2021년 2월
박사학위 논문

Design Methodology Validation for Structural Design of Highly Damped Deployable Solar Panel Module Under Launch Vibration and Thermal Environment

조선대학교 대학원

항공우주공학과

바타라이 샹카

Design Methodology Validation for Structural Design of
Highly Damped Deployable Solar Panel Module Under
Launch Vibration and Thermal Environment

발사 진동 및 열 환경에서 고댐핑

전개형 태양 전지판 모듈의

구조설계를 위한 설계 방법론 검증

2021년 2월 25일

조선대학교 대학원

항공우주공학과

바타라이 샹카

Design Methodology Validation for Structural Design of Highly Damped Deployable Solar Panel Module Under Launch Vibration and Thermal Environment

지도교수 오 현 웅

이 논문을 공학 박사학위 신청 논문으로 제출함.

2020 년 10 월

조선대학교 대학원

항공우주공학과

바타라이 샹카

바타라이 샹카의 박사학위논문을

인준함

위원장 조선대학교　　　겸임교수　　유 영 준 (인)

위　원 조선대학교　　　교수　　　　오 현 웅 (인)

위　원 조선대학교　　　교수　　　　안 규 백 (인)

위　원 전북대학교　　　교수　　　　임 재 혁 (인)

위　원 ㈜솔탑　　　　　책임연구원　김 홍 래 (인)

2020 년 12 월

조선대학교 대학원

Contents

LIST OF FIGURES

LIST OF TABLES

NOMENCLATURE

ADCS	Attitude Determination and Control System
APSD	Acceleration Power Spectral Density
AU	Astronomical Unit
BBIRC	Board Band Infra-Red Camera
BCR	Battery Charge Regulator
C & DH	Communication and Data Handling
CFRP	Carbon Fiber Reinforced Plastic
Co.	Company
COTS	Commercial-Off-The-Shelf
CS	Communication System
CubeSat	Cube Satellite
CW	Continuous Wave
DAQ	Data Acquisition
DOD	Depth of Discharge
DVBS	Digital Video Broadcast Satellite
EBA	Energy Balance Analysis
ECSS	European Cooperation for Space Standardization
EM	Exploration Mission
EO	Electro Optical
EOC	Electro Optical Camera
EOL	End of Life
EPS	Electrical Power System
ESA	European Space Agency
FR4	Fiberglass Reinforced

GaAs	Gallium Arsenide
GASPAC	Get Away Special Passive Attitude Control Satellite
GEVS	General Environmental Verification Standard
GMSK	Gaussian Minimum Shift Keying
GPS	Global Positioning System
GSD	Ground Sampling Distance
HiREV	High-Resolution Image and Video
HRM	Holding and Release Mechanism
IFB	Interface Board
IR	Infra Red
ISISpace	Innovative Solutions in Space
ISSL	Intelligent Space Systems Laboratory
JAXA	Japan Aerospace Exploration Agency
JPL	Jet Propulsion Laboratory
KARI	Korea Aerospace Research Institute
LEO	Low Earth Orbit
LLSS	Low Level Sine Sweep
Ltd.	Limited
LTDN	Local Time Descending Node
LV	Lunch Vehicle
LWIRC	Longwave Infrared Camera
MarCO	Mars Cube One
MCU	Microcontroller Unit
MicroMAS	Micro-sized Microwave Atmospheric Satellite
MIT	Massachusetts Institute of Technology
MOM	Multiple Orbit Mission
MPC	Multi Point Constraint
MSIT	Ministry of Science and ICT

NASA	National Aeronautics and Space Administration
NRL	Naval Research Laboratory
OBC	On-board Computer
OMOTENASHI	Outstanding Moon Exploration Technologies Demonstrated by Nano Semi-Hard Impactor
PCB	Printed Circuit Board
PCDU	Power Control Distribution Unit
PDHS	Payload Data Handling System
PDTS	Payload Data Transmission System
P-HRM	Pogo Pin based Holding and Release Mechanism
P-POD	Poly Picosatellite Orbital Deployer
PSD	Power Spectral Density
RAAN	Right Ascension of the Ascending Node
RBE2	Rigid Body Element, Type 2
RBE3	Rigid Body Element, Type 3
RMS	Root Mean Square
SADA	Solar Array Drive Assembly
SDOF	Single Degree of Freedom
SINDA/FLUIENT	Systems Improved Numerical Differencing Analyzer and Fluid Integrator
SLS	Space Launch System
SMA	Shape Memory Alloys
SOH	State of Health
STEP Cube Lab-II	Cube Laboratory for Space Technology Experimental Project-II
STSL	Space Technology Synthesis Laboratory
TJ	Triple Junction
TMM	Thermal Mathematical Mode

TRP	Temperature Reference Point
TV	Thermal Vacuum
U.S.	United States
UHF	Ultra High Frequency
VMLSA	Viscoelastic Multi-layered Stiffener based Solar Array
XI-IV	Sai Four

초   록

발사 진동 및 열 환경에서 고댐핑 전개형 태양 전지판 모듈의 구조설계를 위한 설계 방법론 검증

바타라이 샹카

지도교수 : 오 현 웅

항공우주공학과

조선대학교 대학원

지난 10년 동안 큐브위성의 연구 개발에 상당한 진전이 이뤄짐에 따라 큐브위성의 제한적인 표면적으로 인해 궤도상 전력생성량 확보에 한계가 있어 더 도전적이고 고난도의 임무를 수행함에 있어서 한계점이 있음이 지속적으로 제기되어 왔다. 이에 따라 태양전지셀 장착을 위한 표면적을 확장하기 위해 일반적으로 전개형 태양전지판이 적용되어 왔으나, 이는 발사 진동환경에서 패널의 과도한 동적변위가 발생할 경우 패널에 장착된 태양전지셀에 가해지는 하중에 의한 균열 및 파손을 유발할 수 있다. 극심한 발사환경 하에서 전개형 태양전지판의 구조건전성을 보장하는 것은 성공적인 큐브위성의 임무를 위한 중요한 요소 중 하나이다.

큐브위성용 태양전지판의 동적변위를 최소화하기 위한 기존 설계는 대부분 PCB 소재의 태양전지판에 알루미늄 등 PCB 대비 고강성 구현이 가능한 소재로 제작된 보강재를 추가로 적용하거나, 또는 CFRP 패널이나 하니컴 패널을 사용하는 등 주로 패널의 강성을 높여 동적변위를 줄이는 데 초점을 맞췄다. 그러나 이러한 설계방식은 보강된 태양전지판의 중량

증가로 인해 구속분리장치에 가해지는 하중 부담이 불가피하게 증가할 수 있는 문제를 수반한다. CFRP 및 벌집형 패널은 상대적으로 패널 구조의 강성 대비 경량화를 달성할 수 있어 항공우주 분야 전반에서 일반적으로 폭넓게 사용되고 있다. 큐브위성의 경우 태양전지판을 수납하여 POD로 불리는 전용 발사관에 수납하여 발사가 이뤄지는 구조이며, POD 내부 공간적 제약 상 태양전지판의 수납 시 장착면으로부터의 높이가 증가할수록 수납성이 저하되기에 가급적 Low Profile로 수납이 이뤄질 수 있도록 설계되는 것이 중요하다. 그러나 앞서 말한 하니컴 패널의 경우 기본적인 두께 상 큐브위성용 태양전지판에 적용 시 수납 효율성이 비교적 낮을 수 밖에 없다. 가급적 저가에 개발되는 큐브위성 특성상 CFRP 소재의 경우 개발비용 증가가 예상되어 적합하지 않을 수 있다. 태양전지판 보강구조를 최소화하고 다수의 분리장치를 여러 구속지점에 적용하는 방법도 있으나, 시스템 복잡화가 예상되며, 궤도상에서 하나의 분리장치라도 전개되지 않을 경우 임무실패로 이어질 수 있는 신뢰도 측면의 위험성이 증가한다는 단점이 있다.

본 논문에서는 STEP Cube Lab-II 6U 큐브위성 적용을 위해 포고핀 기반 Burn Wire Triggering 방식 구속분리장치과 결합된 고댐핑 전개형 태양전지판 모듈에 관해 연구하였으며, 이에 대한 설계 유효성을 검토하였다. 제안된 태양전지판은 점탄성 테이프를 이용해 다층으로 적층된 PCB 구속층을 태양전지판 배면부에 적용함으로서 기존 소재로는 구현 불가능한 수준의 우수한 댐핑 특성을 구현 가능하여 발사 진동환경 하 태양전지판의 구조건전성을 보장하는 데 효과적이다. 또한 태양전지판의 발사구속 및 궤도상에서의 전개 기능은 전술한 포고핀 기반 분리장치를 통해 이뤄지며, 나일론 와이어를 이용해 태양전지판을

구속하고 저항소자의 발열로 구속을 해제하는 방식으로 작동된다. 이 분리장치의 특징은 포고핀만으로 전개를 위한 저항소자로의 전력공급 인터페이스, 구속해제 시 포고핀 스프링 반력에 의한 전개 Initiation 및 구속해제 확인용 스위치로도 활용 가능한 장점을 갖는다. 제안된 태양전지판 모듈의 발사환경 하 구조건전성 검토를 위해 유한요소모델(FEM)을 구축하고 모드해석, 랜덤진동해석을 수행하였다. 또한 준정적해석을 통해 제안 태양전지판과 결합된 구속분리장치의 적용된 나일론 와이어의 안전여유를 분석하였다. 또한 궤도열해석을 수행하여 태양전지판에 적용된 소재의 코팅 유무에 따른 열적 특성을 분석하였다. 설계된 태양전지판 모듈을 제작하고 이에 대한 구조/열적 측면에서의 설계 유효성을 실험적으로 검증하였다. 우선, 댐핑 성능 및 강성 등 태양전지판의 기본 특성을 획득을 위해 자유감쇠시험을 실시했다. 또한 발사환경시험을 통해 태양전지판 모듈의 구조건전성을 입증했다. 제안된 태양전지판의 포고핀 기반 분리장치는 열진공 환경에서의 전개시험을 통해 검증되었다.

키워드: 큐브위성, 전개형 태양전지판, 점탄성 테이프, 구속층, 포고핀, 발사환경, 궤도열환경

ABSTRACT

Design Methodology Validation for Structural Design of Highly Damped Deployable Solar Panel Module Under Launch Vibration and Thermal Environment

by Bhattarai, Shankar

Advisor : Prof. Oh, Hyun-Ung, Ph.D.

Department of Aerospace Engineering

Graduate School of Chosun University

Despite the significant progress made in CubeSat research and development over the last decade, some fundamental questions still habitually arise on its abilities for achieving more challenging and sophisticated missions due to limited in-orbit power generation capability by restraint surface area. The deployable solar panels have commonly been used to expand the surface area for solar cells integration, though, it involves the problem of excessive dynamic displacement of the panel during a launch environment that could cause delamination or stress and crack on solar cells mounted on the panel through the bonded junctions. Ensuring the structural safety of a deployable solar panel under a severe launch vibration environment is one of the important factors for a successful CubeSat mission.

To minimize the dynamic deflection of the panel, most of the previous strategies have focused on increasing the stiffness of the panel by applying additional stiffeners made up of various materials such as aluminium and fiberglass-laminate, or using carbon fiber reinforced plastic (CFRP) panel and honeycomb panel. However, it involves an inevitable increase in mass and

acceleration response of the stiffened panel that could produce an undesirable burden on HRM. The CFRP and honeycomb panels are relatively light in weight and exhibit high stiffness, thus commonly been used in aerospace applications wherever high strength to weight ratio and rigidity are required. However, those structures are expensive and thick in size that has made them less practical for advanced missions of the CubeSat platform due to the internal restraint edge gap on the poly-picosatellite orbital deployer (P-POD) for the solar panel accommodation and development cost limitations. As an alternative solution in regards to the above issues, multiple numbers of HRMs could be applied to provide additional mechanical fixation points on the solar panel, although it could increase system complexity and reduce the available area for solar cell accommodation.

In this present work, a highly damped deployable solar panel module combined with pogo pin-based burn wire triggering release mechanism was developed and investigated for application in the STEP Cube Lab-II 6U CubeSat. The solar panel proposed herein is effective in guaranteeing the structural safety of solar cells under a launch environment owing to the superior damping characteristics achieved using multi-layered stiffeners with viscoelastic acrylic tapes. A holding and release action of the solar panel was achieved by a new version of spring-loaded pogo pin-based burn wire triggering mechanism. The power budget of CubeSat is calculated based on the system requirement according to the mission operations and the energy balance analysis to satisfy the onboard power demand of subsystems and payloads for the mission performance. The solar panel size is determined accordantly. The structural safety of the solar panel module in launch vibration loads is estimated by modal and random vibration analysis of the design through the finite element method (FEM) in MSC Patran/Nastran Softwares for acquiring the mode shape, stiffness, and dynamic responses. In addition, the margin of safety (MoS) of the nylon wire for holding

constraint at the panel is evaluated through the random equivalent static analysis. Furthermore, a thermal mathematical model (TMM) of the solar panel was constructed using a thermal desktop. A thermal design based on thermal coatings or paints on the solar panel surfaces is analyzed by a computer-aided design (CAD) based geometric interface for commercial in-orbit thermal analysis tool of Systems Improved Numerical Differencing Analyzer and Fluid Integrator (SINDA/FLUINT) for minimization of thermal gradient during the in-orbit performance. A qualification model of high-damping solar panel assembly was fabricated and tested to validate the effectiveness of the design. To investigate the basic dynamic characteristics of the solar panel, such as damping performance and stiffness, free-vibration tests were performed. The holding and release mechanism achieved using a pogo pin was functionally tested through solar panel deployment tests under ambient room temperature and a thermal vacuum environment. In addition, the total ionizing dose (TID) and single event effect (SEE) radiation tests of the electrical interface PCB of the mechanism were carried out for radiation hardness assurance. The design effectiveness and structural safety of the solar panel module were validated through qualification-level launch and in-orbit environment tests.

Key Word: CubeSat, Deployable Solar Panel, Multi-layered Stiffener, Viscoelastic Acrylic Tape, Vibration Damping, Launch Vibration, Thermal Vacuum Environment

I. Introduction

A. CubeSat Overview

The Space age is generally considered to have begun with the historic launch of Sputnik 1 in 1957 by the Soviet Union [1]. Subsequently, over the last 63 years, hundreds of satellites were launched for a variety of purposes such as Earth science [2], astronomy and astrophysics [3], and planetary science [4]. Traditionally the space industry produced large and sophisticated spacecraft by large teams of engineers, it takes an average of 5 years to build and required a single rocket for the launch of a satellite. For instance, the famous Hubble Space Telescope is the size of a school bus: 13.2 m long, 4.2 m wide, and 2.4 m diameter aperture [5]. The big satellites are capable of hosting large payloads, sophisticated scientific missions, and tend to have longer lifetime in space, however, the development and launch of such spacecraft require significant resources within the reach of only a few large government-backed space agencies such as the National Aeronautics and Space Administration (NASA) and European Space Agency (ESA) among others. The satellite launch mass gradually increased and reached peak values in the late 1990s and early 2000s. The current tendency in space is to move towards smaller satellites owing to the recent advances in technology miniaturization, which are significantly cheaper than their larger companions and can be designed and built in a much shorter time span with readily available, low cost, low power, and compact commercial-off-the-shelf (COTS) components.

In 1999, Jordi Puig-Suari of California Polytechnic State University and Bob Twiggs of Stanford University proposed a CubeSat as a form factor for nanosatellites for realizing the significances of the standardized platform [6]. A CubeSat is a cube-shaped nano-class miniaturized satellite having a volume of 1000 cm^3 with a maximum mass of 1.33 kilograms (kg) per a standard size of one unit (1U) [7], although larger configurations are also permissible such as 2U, 3U, 6U, 12U, and largest 27U by stacking the units. Figure 1 shows the general configurations of CubeSats size according

to their units. The CubeSats were primarily envisioned for low-cost educational [8] and scientific [9] missions in universities and research institutions. Although, satellites utilizing this form factor has been received considerable attention in the area of space science [10], technology verification [11], meteorology [12], and earth observation [13] owing to the miniaturization of electronics and sensors, low-cost and short period for construction and launch or else availability to launch as a secondary payload. In recent, this trend has been rapidly facilitated by the use of COTS components for electronic and structure to achieve a wide range of operational missions based on CubeSat constellations [14-16] with potential high value in terms of science return and commercial revenue. CubeSats have evolved to become an important platform for space-based research.

| (a) | (b) | (c) |
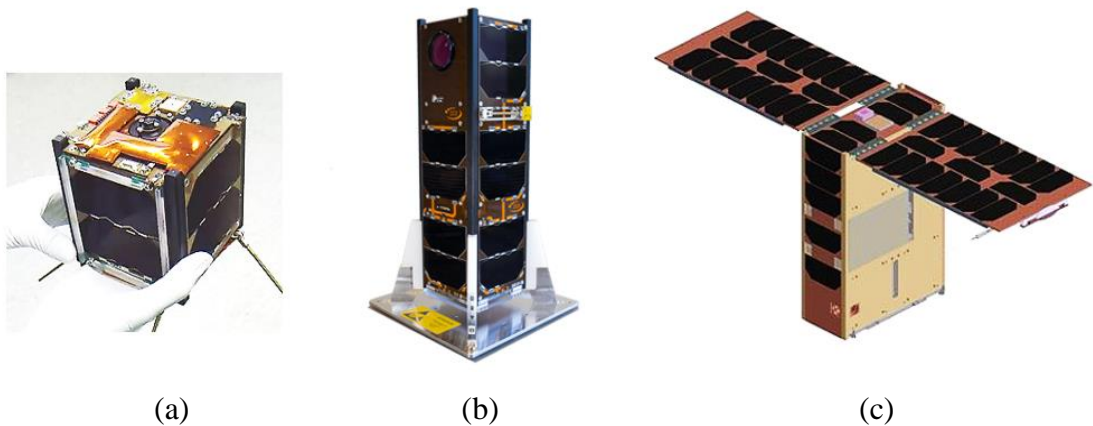
Fig. 1 Configuration of CubeSats Size According to Unit: (a) 1U, (b) 3U and (c) 6U.

The space activities have become more accessible by CubeSats as they are launched as a secondary payload by a stable and efficient canisterized deployer, poly picosatellite orbital deployer (P-POD) using leftover mass that is not used by more expensive primary spacecraft. CubeSats could democratize to access space for small countries, educational institutions, commercial organizations, and even individuals around the world by allowing them to develop and launch their own satellite with a relatively modest budgets of a few hundred thousand dollars. The cost and complexity of CubeSat development

and launch is drastically reduced compared to traditional large satellites, which is demonstrated by the noted dramatic rise in the number of CubeSat launches over the past decade shown in Fig. 2 [17]. The number of nanosats launched was 1417 until the beginning of October 2020, of which 1302 were CubeSats. Among these, the 3U and 6U configurations were the most commonly used CubeSat types.
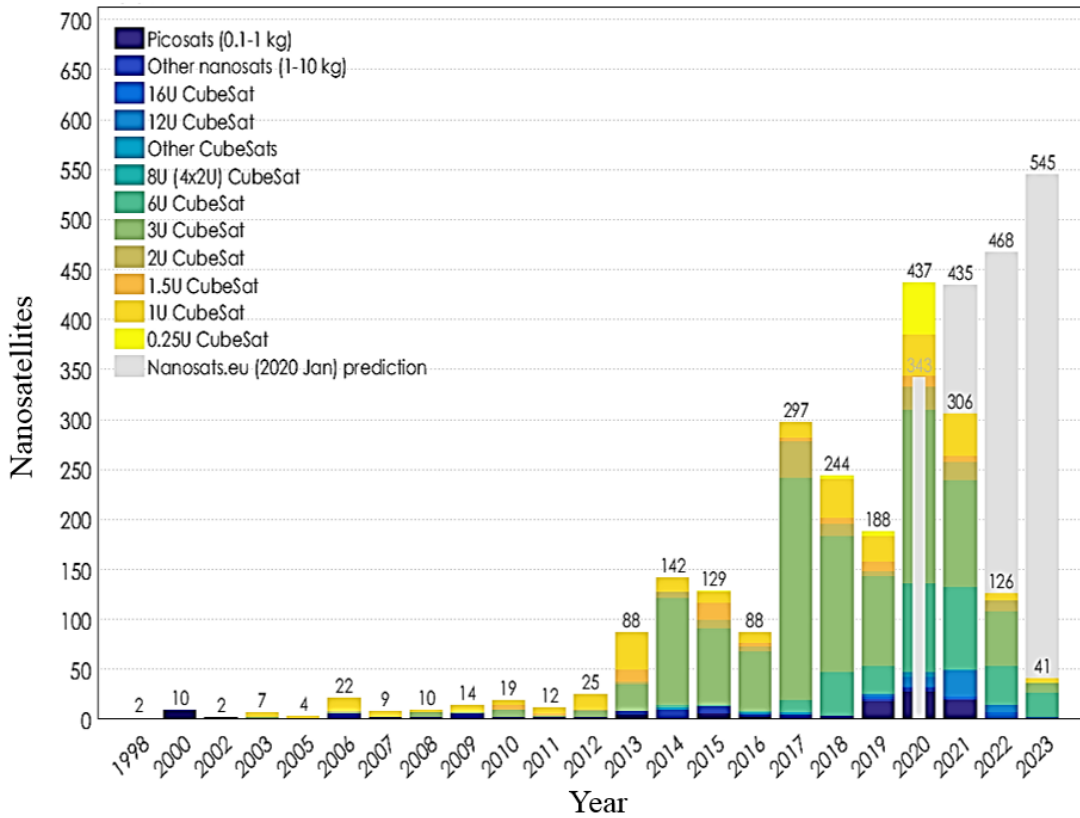
Fig. 2 Number of Nanosatellites Launched and Forecasts [17].

Figure 3 shows an example of a CubeSat development tendency and mission objectives. The first CubeSat in orbit is sai-four (XI-IV), developed by the intelligent space systems laboratory (ISSL) of the University of Tokyo, which was launch on June 30, 2003 from Plesetsk, Russia, with Eurockot Launch Services' Multiple Orbit Mission (MOM) [18]. The main mission objective of 1U sized XI-IV CubeSat was a technology demonstration of basic bus systems for nanosatellites with verification of commercial-

off-the-shelf camera. The XI-IV is still alive and working its operation for more than sixteen years as of 2020 blowing away anybody's expectation, satellites launched with a similar mission and capabilities failed early on. The image sensor of XI-IV has been sent lots of Earth images to the ground station from orbit [19]. In recently, a more advanced CubeSat has also been developed and proposed to reduce the risk of future larger and sophisticated satellite missions by testing new technologies, increasing the Technology Readiness Level (TRL) of satellite components, and demonstrating the science missions at a fraction of the cost of traditional larger satellites. In other words, CubeSat could also be used in high-risk high-value missions. For instance, Mars Cube One (MarCO) 6U CubeSat, developed by the NASA Jet Propulsion Laboratory (JPL) is the first nanosatellite built on the CubeSat form factor to operate beyond the Earth orbit for the demonstration of deep space communication and navigation [20]. The Japan Aerospace Exploration Agency (JAXA) is currently developing an Outstanding Moon Exploration Technologies Demonstrated by Nano Semi-Hard Impactor (OMOTENASHI) 6U CubeSat, one of thirteen CubeSats to be carried with the Orion Exploration Mission-1 (EM-1) into a heliocentric orbit in cislunar space on the maiden flight of the NASA space launch system (SLS), scheduled to launch in 2021. The purpose of the mission is to measure the radiation environment near the Moon as well as on the lunar surface and to demonstrate low-cost technology for a semi-hard landing on the Moon's surface after being deployed into a lunar fly-by orbit by the SLS/EM-1 spacecraft [21]. In addition, inexpensive COTS components that are readily available also allow larger CubeSat constellations with the potential to achieve comparable or even greater performance compared to conventional spacecraft, as well as to create a novel class of mission concepts.

XI-IV (Japan)	GOMX-1 (Denmark)	CNUSail 1 (South Korea)	MarCO (USA)
•Size: 1U (100 mm × 100 mm × 100 mm) •Organization: University of Tokyo •Mission: Demonstrate CubeSat Platform Technologies and COTS Camera •Power Generation: 1.1 W •Launch: June 30, 2003	•Size: 2U (100 mm × 100 mm × 200 mm) •Organization: GOMSpace •Mission: Demonstration of Potential on Aircraft Tracking from Space •Power Generation: 7 W •Launch: November 21, 2013	•Size: 3U (100 mm × 100 mm × 300 mm) •Organization: Chungnam National University •Mission: Deploy Solar Sail and Perform on Orbit Maneuver •Power Generation: 11 W •Launch: January 12, 2018	•Size: 6U (118 mm × 243 mm × 366 mm) •Organization: Jet Propulsion Laboratory •Mission: Deep Space Communication and Navigation •Power Generation: 35 W •Launch: May 5, 2018

Fig. 3 CubeSat Development Trend and Mission Objectives.

B. Power Demand

In recent years, CubeSat on-board power demand has steadily increased as the capability of the platform for advanced missions have significantly improved owing to the recent advances in technology miniaturization. The microprocessors, sensors, and computing technology continue to shrink in size to fit in the constraint volume and mass of the CubeSat platform, although the component power requirements remain nearly steady. Moreover, payloads and data transmission capabilities are also limited if the power generation is insufficient. An increase in the power generation of a CubeSat can increase its potential because data collection, data transmission, and data processing are dependent on the power capacity. The 3U and 6U CubeSat platforms with the dimension of three- and six-unit of 1U have become increasingly popular [22] in research laboratories and small companies aimed to conduct more advanced scientific missions in a short development timeline. However, one of the main limitations of the CubeSat bus is the availability of in-orbit power generation capability owing to the restrained surface area for solar cell installation that has become a concern for implementing advanced payloads. Average power obtained on a 3U CubeSat by using body-mounted high-efficiency triple-junction solar cells is typically less than 10 W [23]. No matter the size of the CubeSat, or the configuration, power is always precious for the success of a

CubeSat mission, the power usage must be moderated and managed according to the payloads and bus system's power consumption. Consequently, the in-orbit power generation capacity of a CubeSat is as important as ever for a given CubeSat for the success of advanced missions.

C. Statement of the Problem

Despite the considerable progress made in CubeSat research and development over the last decade, due to the restrained on-board power generation capability, some fundamental questions still habitually arise about its capabilities, limitations, and ultimately about their scientific and commercial value [24, 25]. Several studies have been carried out to maximize power generation and different solutions have been investigated to optimize the solar panel configuration, including the possibility of deploying solar arrays from the surface of the CubeSat [26, 27]. One technical solution to satisfy increasing onboard power demand is the adoption of a deployable solar panel that encompasses expand surface areas for solar cell installation as well as optimizing the orientation or the articulation of panels by the use of a solar array drive assembly (SADA) in the Sun direction. When the sun is orthogonal to the solar panels, the power generation performance would increase by 160% to 400% relative to the body-mounted solar panels [28]. CubeSats do not normally have solar panels that actively track the Sun because of the additional complexity required for hinges, motors, sensors, and attitude stabilization. The MarCO CubeSat is powered by two deployable solar arrays, these arrays fold to a single 3U panel and stowed on the CubeSat structure during the launch, but extend out to reveal 42 solar cells, able to provide approximately 35 W of average power capability as at 1 astronomical unit (AU) distance from the Earth surface [29].

In recent, the deployable solar panels based on the printed circuit board (PCB) substrate have been excessively produced owing to the advantages of rapid fabrication and provides ease of electrical interconnection between the solar cells. For stowing and releasing those deployable panels, hold and release mechanisms (HRMs) based on a burn wire triggering method are widely utilized owing to their simplicity, low cost, and

ease of mechanism reset. These mechanisms usually provide a mechanical constraint on the solar panel during launch by tightening the nylon wire, which is then cut by heating the nichrome wire or burn resistor to release the panel in orbit. However, the deployable solar panel mounted on the CubeSat is subjected to severe launch vibration environments [30]. The excessive dynamic deflection of a solar panel under a vibration environment causes stress at the solar cells mounted on the panel by the bonded junction, which could ultimately lead to a crack or fracture in those cells. In general, solar cells in a panel are wired in series connection to achieve higher voltage if one of the cells fails to generate power, which causes loss of electrical energy from a solar panel. This problem becomes more severe when the solar panel size is larger. Thus, the minimization of solar panel dynamic deflection and stress during a severe launch environment for ensuring the structural safety of solar cells mounted by bonded junctions is one of the important factors for mission success.

D. Literature Review

In order to overcome the aforementioned issues, several mechanical design strategies such as increasing eigenfrequency of the solar panel by implementing stiffeners made up of aluminum or fiberglass-laminate, using carbon fiber reinforced plastic (CFRP) and honeycomb panels, or else employing multiple holding and release mechanism (HRMs) to provide additional mechanical fixation points have been practiced by considering the design specification and mission requirements [31-33]. For example, innovative solutions in space (ISISpace) [31] developed deployable solar panels as shown in Fig. 4, where the thin FR4 printed circuit board (PCB) solar panel with a thickness of 0.18 mm is stiffened by an aluminium panel. Park et al. [32] developed a PCB-based 6U CubeSat's deployable solar panel stiffened by high-pressure fiberglass-laminated G10 material. Besides, Lim et al. [33] developed a 6U sized deployable solar panel based on an aluminium honeycomb panel instead of the PCB to ensure a stiffness requirement specified by the launch provider. In the case of stiffener strategy rigidity of stiffener is the key point for increasing the eigenfrequency of the

panel. However, the implementation of the additional stiffener approach involves a trade-off between the panel's stiffness and weight that might be a disadvantage for the CubeSat having a restraint mass budget. Additionally, the inevitable increase in mass raises the acceleration response of stiffened panels that could produce an undesirable burden on HRM, especially the ones based on the nylon wire cutting mechanism generally used in CubeSat applications.
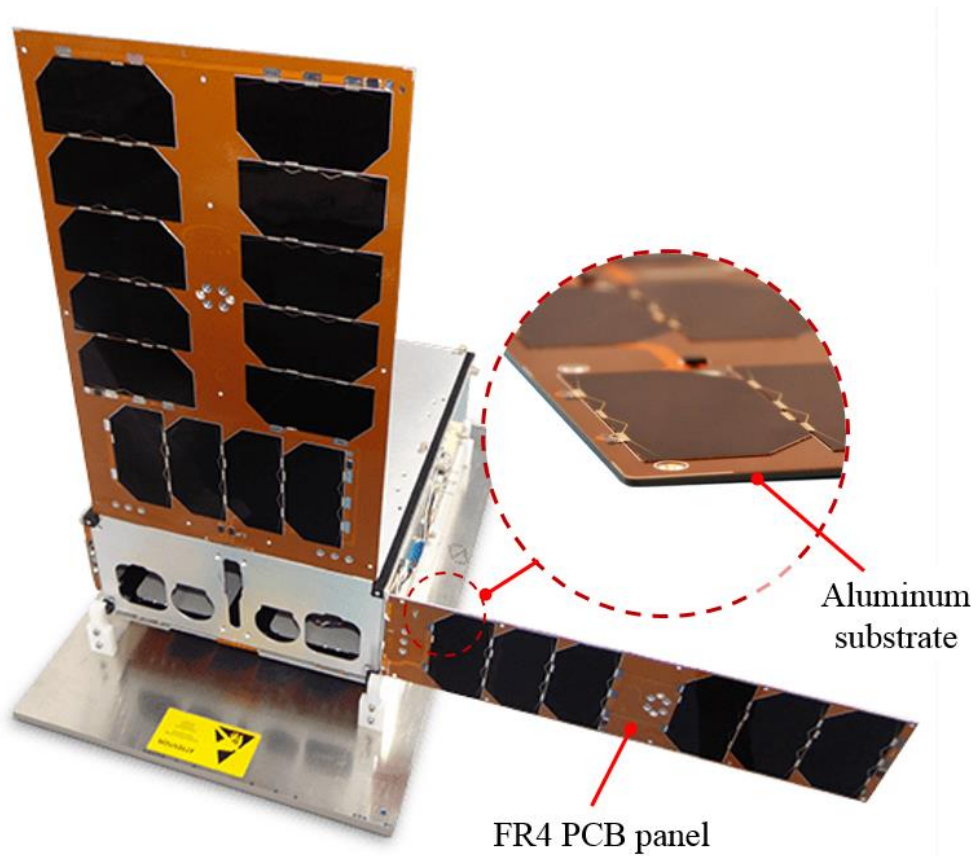
Fig. 4 ISISpace's Deployable Solar Panel for CubeSat Applications [31].

The CFRP and honeycomb panels are relatively light in weight and exhibit high stiffness, thus commonly been used in aerospace applications wherever high strength to weight ratio and rigidity are required. However, those structures are expensive, thick in size that have made them less practical for advanced missions of the CubeSat platform

due to the internal restraint edge gap on the poly-picosatellite orbital deployer (P-POD), 7 mm [34] for the solar panel accommodation and development cost limitations. Figure 5 shows the deployed configuration of VELOX-II CubeSat's Al-honeycomb-based solar panel.
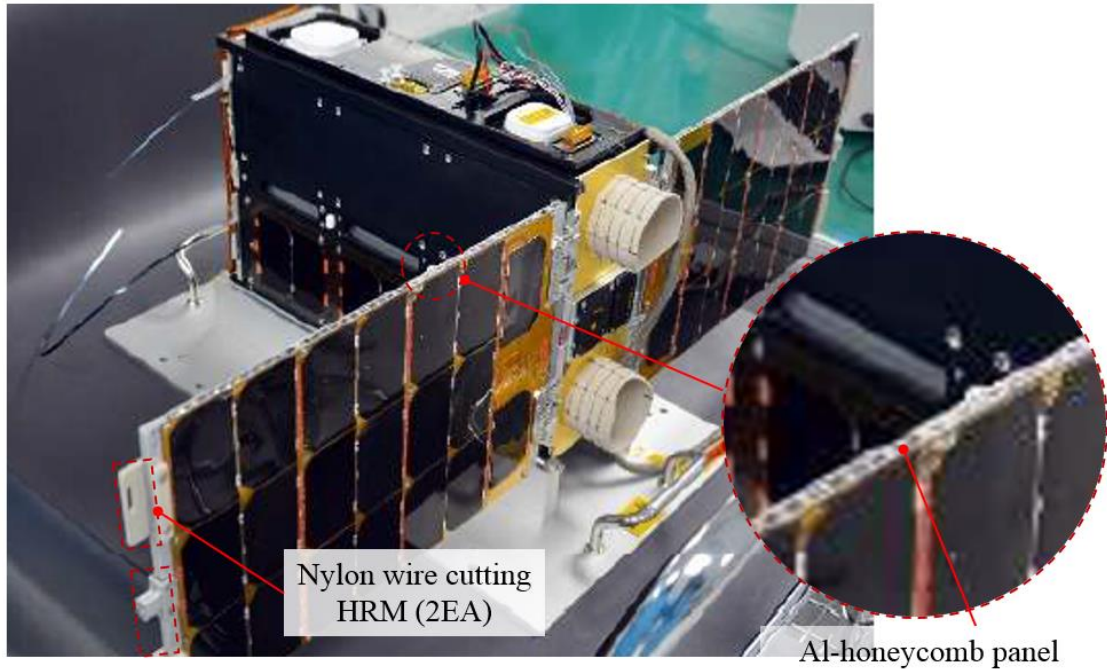
Fig. 5 Deployed Configuration of VELOX-II CubeSat's Solar Panel [33].

In recent, as an alternative solution in regards to the above issues, multiple numbers of HRMs have been applied to provide additional mechanical fixation points on a 6U or larger sized solar panels aiming for minimizing dynamic deflection. For instance, GomSpace developed a nano power deployable solar panel for the application of 3U and 6U CubeSats, where two sleds with spring-based burn wire cutting HRMs were used to reduce the dynamic response of the panel under launch environments [35]. However, this could increase system complexity, development cost, and reduce the available area for solar cells accommodation. Figure 6 shows the GomSpace nano power deployable solar panel module.
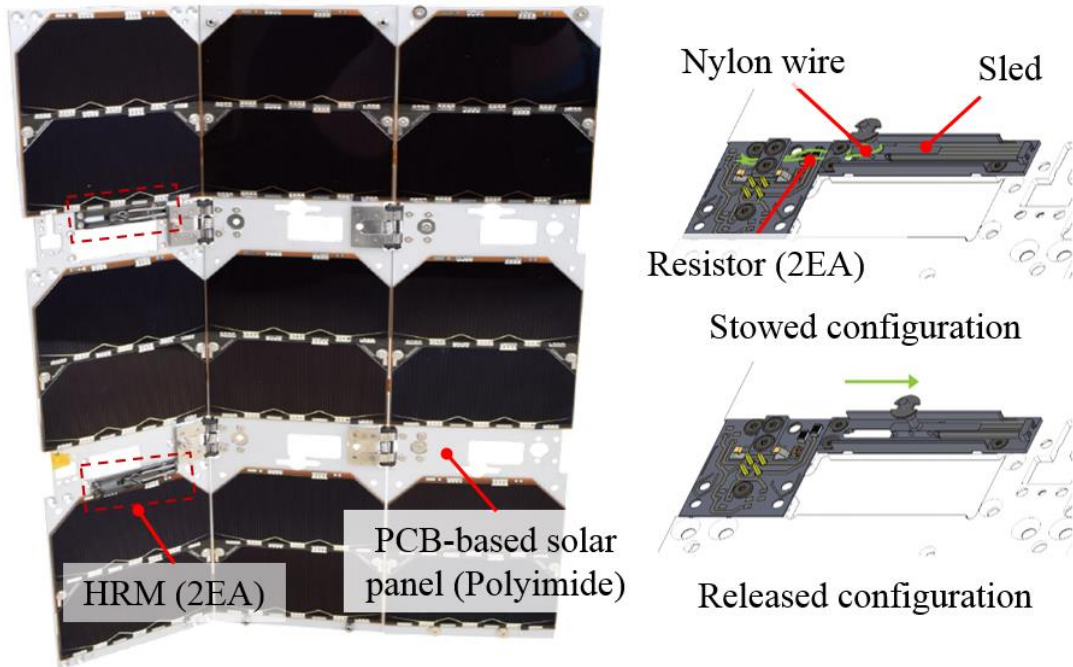
Fig. 6 Configuration of GomSpace Nano Power Deployable Solar Panel Module [35].

Furthermore, the MMA design LCC [36] has recently proposed various configurations of mass-effective multi-array-based deployable solar panels, where an additional launch restraint mechanism is implemented in conjunction with wire cutting release mechanism to reduce panel dynamic deflection and stress on the holding constraint under launch environments. The solar panel architecture provides a building block approach that enables modularity and scalability, although the implementation of an additional launch restraint device creates system complexity.

Another technical issue related to the deployable solar panel is the necessity of reliable HRM to provide adequate strength and stiffness for survival in launch environments and release functions to allow deployment in orbit. Several types of mechanisms such as pyrotechnic device [37], shape memory alloys (SMA) actuator [38], mechanical motor [39], explosive bolt [40], and burn wire cutting [41] have been practiced in CubeSat applications by considering the design specification and mission

requirements. The pyrotechnic devices often induce a high-level dynamic resonance due to the sudden transient release of the restraining energy, that high-frequency pyroshock will lead to electrical malfunctions or critical damage on the satellite [42]. The non-explosive SMA separation devices have relatively low shock, high loading capability, and reputability functions [43]. Though SMA materials are costly, high weight and dimension limitations make these HRM less applicable for CubeSat deployable applications. Another technique, the mechanical motors would be beyond the CubeSat budget and required significant volume capability. Moreover, explosive bolts for holding and releasing the mechanical strength of the deployable structures in CubeSat are prohibited by NASA CubeSat guidelines [44]. Among them, a burn wire triggering release method has commonly been used in CubeSat's deployable appendages owing to its simplicity and low-cost. In 2014, Thurn et al. [45] developed a burn wire release mechanism to deploy a stacer and tether deployment system at the United States (U.S.) Naval Research Laboratory (NRL). The mechanism utilizes a nichrome burn wire when power activated heats up and cuts through a Vectran tie-down cable allowing the deployment of the appendages. This novel research reveals the application of wire cutting release mechanism for the CubeSat's deployable structures. Gardiner, J. [46] proposed a nickel-chromium wire cutter based HRM for the restraining and releasing the deployable AeroBoom of Get Away Special Passive Attitude Control Satellite (GASPACS) mission. The nickel chromium-filament is used as a heating element, upon activation of the mechanism dyneema wire restraining the AeroBoom thermally cut, consequently released the holding constraint. Bharadwaj and Gupta [47] developed an antenna deployment mechanism for CubeSat application by considering the protrusion and space constraints [48] inside the poly pico-satellite orbital deployer (P-POD). The antennas are stowed on the sub-frame of CubeSat using dyneema wire, and the antenna's release action is triggered by a through-hole resistor that is heated with a current limiting integrated circuit. The Micro-sized Microwave Atmospheric Satellite (MicroMAS) [49] is a 3U CubeSat developed by the Massachusetts Institute of Technology (MIT) space laboratory that is powered by body-mounted as well as four 2U sized deployable solar

panels. The deployable panels were stowed on the CubeSat structure through the holding constraint of nylon wire tightened over the holes interface of the panel and zenith facing plane of the satellite body. The activation of the mechanism releases the holding constraint of the panel by melting the nylon wire. Furthermore, the deployable solar panels of high-resolution image and video (HiREV) CubeSat [13] were tied up by nylon wire to stow during launch, activation of the nichrome wire released the panel's holding restraint by melting the nylon wire. Figure 7 shows an example of a conventional burn wire cutting type of HRM. However, as the size of CubeSat's solar panel getting larger for advanced missions, these mechanisms should be improved because of their limited loading capability, lack of mechanical constraint along with in-plane directions of a solar panel, unable for synchronous release of panels, and difficulty for wire knotting on the flat surface.
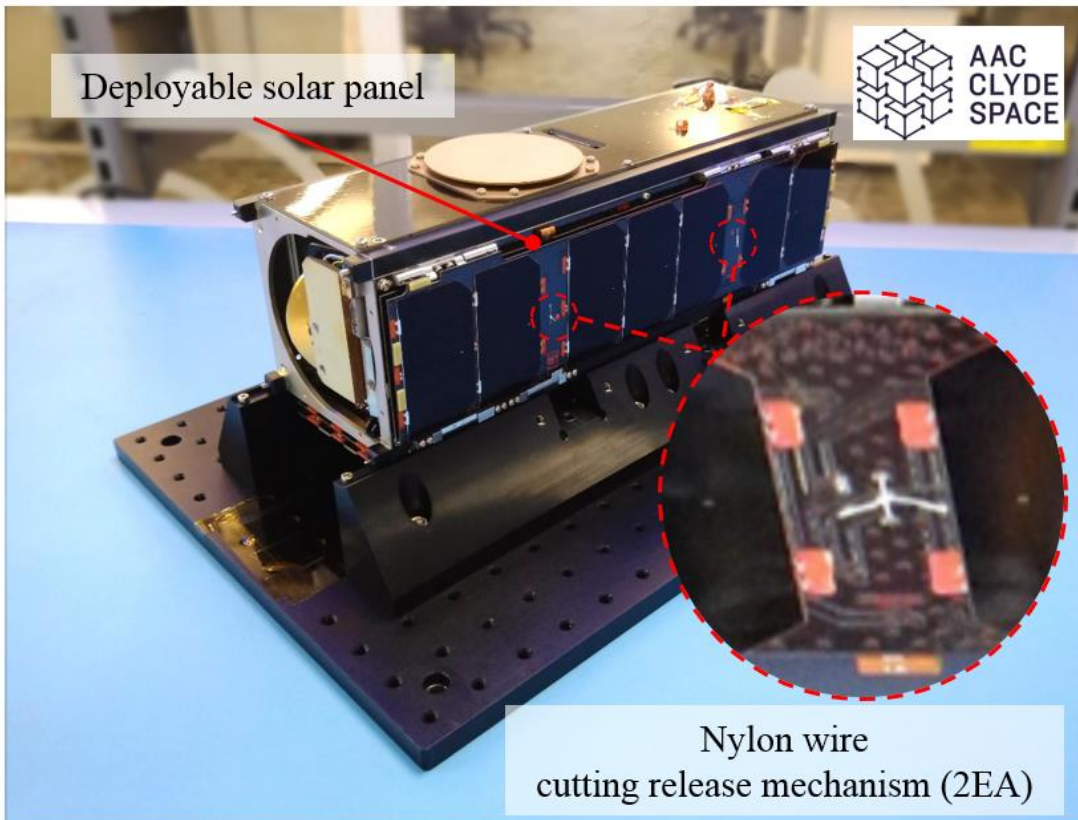
Fig. 7 Example of Conventional Burn Wire Cutting Type of HRM [50].

Furthermore, another potential technical problem related to the deployable solar panel is an oscillation of the deployed panel induced by satellite attitude maneuvering because it causes a rigid body motion of the satellite, which might degrade its pointing stability in-orbit. In recent years, the complexity of CubeSat missions has been increasing steadily as the platform capability has drastically improved. Missions involving high-accuracy fine-pointing stability for Earth observation and interplanetary explorations are no longer out of the reach of CubeSats. The in-orbit low and medium frequency vibration can also be critical for some on-board equipment and sensors, the microvibrations may degrade the image balance of an observation satellites. During the in-orbit operation, where rapid slew maneuvers are required for the acquisition of a target point, the interaction of deployable solar panels with the attitude control system could generate a rigid body motion owing to the low flexible mode of panels that can significantly degrade performance in terms of pointing accuracy and acquisition time. This oscillation problem might be unavoidable if the panel size becomes larger due to a low flexible mode of the solar panel. Additionally, the conventional technologies for reducing panel oscillation that has been widely applied for large-class satellites, such as rotary damper or deployable truss link, are extremely difficult to apply them for CubeSats due to the spatial limitations allowed for the deployable appendages. Considering the current trend in CubeSat design of the growing size of deployable solar panels and the stringent criteria for attitude control accuracy, conventional solar panel designs may not be adequate to meet the performance requirements of future advanced missions. These facts indicate that an alternative way for reducing on-orbit panel oscillation might be necessary for advanced CubeSat missions.

E. Motivation and Objective

Taking into account the trend of CubeSat solar panels becoming larger for advanced missions, the aforementioned technical problems related to solar panel vibrations in launch and in-orbit environments and the reliability issue of the HRM should be solved. This is the motivation of this dissertation. In this study, we focus on multi-layered PCB

stiffeners with viscoelastic acrylic tapes for attenuation of the launch and in-orbit vibrations in a passive way to ensure the structural safety of solar cells, which is far different than the current state-of-the-art solar panel design strategy for minimizing the dynamic deflection. Viscoelastic materials possess both elastic and viscous properties, which provide damping by converting the excessive mechanical vibrational energy into heat [51]. Many polymeric materials exhibit internal damping due to the rearrangement of long-chain molecules when the material undergoes deformation. The term damping refers to the loss of energy from a system during each cycle. When a viscoelastic material is deformed, the long-chain molecules are stretched and then retract back, when stress is removed, to their original position slowly as compared to pure elastic materials. This slow response opposes the next cycle of vibration [52]. In the category of energy-absorbing materials as a means of passive damping, viscoelastic materials have shown significant efficiency for vibration mitigation and the application of these materials does not alter the mode shapes although increase the natural frequencies of the structure. Thus, the applications of viscoelastic materials for vibration attenuation have been widely studied in space engineering fields owing to the simplicity and cost-effectiveness. For example, Minesugi et al. [53] investigated the damping mechanism of a polyimide tape with viscous lamina for space applications. Torisaka et al. [54] proposed a passive vibration damping approach for the solar panel of the small satellite by considering viscoelastic materials and lightweight aluminium stiffeners. Kwon et al. [55] developed a multi-layered blade-type passive vibration isolator with double-sided viscoelastic adhesive tapes to attenuate the launch and in-orbit vibrations for a spaceborne cryogenic cooler. Furthermore, Steinberg [56] reported that constrained layers of viscoelastic material could be effective for reducing dynamic displacements and stresses in vibrating beam and plate structures.

In this study, a novel highly damped deployable solar panel module combined with pogo pin-based burn wire cutting HRM is proposed for the application in Cube Laboratory for Space Technology Experimental Project-II (STEP Cube Lab-II) 6U CubeSat. An important advantage of the proposed solar panel is that dynamic deflection

and stresses in the panel under launch vibration loads can be effectively minimized owing to the superior damping characteristic achieved by multi-layered stiffener with viscoelastic acrylic tapes. This superior damping characteristic of the solar panel is effective to guarantee the structural safety of solar cells by minimizing the panel dynamic deflection. In addition, this damping characteristic may also be advantageous to rapidly attenuate the oscillation of the deployed solar panel during an in-orbit operation. The CubeSat's power budget and Energy balance analysis (EBA) is performed by power simulation in commercial FreeFlyer software to check whether the generated power from the proposed composition of the solar cells in the CubeSat is balanced with the power consumption for mission scenarios, power storage for the system operation in eclipse, and battery health over the mission life. The solar panel size is determined accordantly. The solar panel's holding and releasing action is achieved by a new version of the spring-loaded pogo pin mechanism that can overcome the aforementioned limitations of conventional burn wire triggering release mechanisms such as increased loading capability, multiplane constraints, and reliable release. The feasibility and effectiveness of three pogo pins in HRM were investigated by Park et al. [57] and Bhattarai et al. [58], although the proposed mechanism has many advantages, including improved holding constraint, simpler electrical circuit, and handling simplicity during the wire knotting process. The structural safety under launch vibration environment and thermal design for the reduction of heat gradient under in-orbit performance is simulated. Furthermore, a demonstration model of a 6U sized solar panel was fabricated and tested to validate the effectiveness of the proposed design. The natural frequency and damping ratio of the solar panel were investigated by conducting free-vibration tests in an ambient room temperature at stowed and deployed configurations. The holding and release mechanism using the pogo pin was functionally tested by solar panel deployment tests under ambient room temperature and thermal vacuum environment. In addition, the total ionizing dose (TID) test of the electrical components used in the mechanism was performed. To validate the effectiveness of design aiming for ensuring a structural safety of solar cells under launch vibration

environment, sine and random vibration tests were performed at a qualification level. A thermal vacuum (TV) test was also conducted to validate the structural safety of solar panel and the functionality of the pogo pin-based mechanism under space simulated thermal vacuum environment. These test results demonstrated that the deployable solar panel module proposed in this study is effective for ensuring a structural safety of solar cells under the launch environment and stable release action in-orbit TV environment.

F. Organization of the Dissertation

Starting with a general introduction of the CubeSat, the content of this dissertation systematically deals with a description of the design methodology validation for structural design of solar panel under launch vibration and thermal environments. To satisfy the objectives of the dissertation presented in the above section, the following are the study design. Chapter II presents an overview of the STEP Cube Lab-II CubeSat mission objective including the operation concept and scenario, power consumption by the payloads and sub-systems, orbit information, power simulation results, and energy balance analysis. We have performed the power simulation by using FreeFlyer commercial software then carry out the energy balance analysis based on power consumption by the components on a mission scenario and the in-orbit generated power. For the optimization of the in-orbit power generation capability of the CubeSat, the various power analysis was performed by changing the orientation of the solar panel towards the Sun direction by satellite roll maneuver according to the mission operation and idle mode of concepts. The battery depth of discharge (DOD) and battery lifecycle is determined based on the energy balance analysis.

In Chapter III, a detailed mechanical design description of a highly damped deployable solar panel module combined with a pogo pin-based burn wire cutting HRM proposed for application in the STEP Cube Lab-II is presented. The electrical system of the pogo pin based HRM and wire tightening process for the holding constraint on the panel are briefly discussed. Furthermore, the torque budget for the panel deployment

and mechanical tolerance gap between the hinge brackets and shaft were estimated based on the ECSS rule.

The structural safety of the proposed solar panel module in the launch vibration environment and thermal design evaluation during in-orbit TV environments are discussed in Chapter IV. The structural safety of the solar panel module in launch vibration loads is estimated by modal and random vibration analysis of the design through the FM modeling. Finite element analysis of the solar panel is carried out using MSC Patran/Nastran Softwares for acquiring the mode shape, stiffness, and dynamic responses under the launch vibration environments. In addition, the MoS of the nylon wire for holding constraints at the panel is evaluated through the random equivalent static analysis. Furthermore, a TMM of the solar panel was constructed using a thermal desktop. A thermal design based on thermal coatings or paints on the solar panel surfaces is analyzed by a CAD-based geometric interface for commercial in-orbit thermal analysis tool of SINDA/FLUINT for minimization of thermal gradient during the in-orbit performance.

In Chapter V, a PCB-based deployable solar panel employing multi-layered stiffeners interlaminated with viscoelastic acrylic tapes was fabricated and experimentally tested to validate the effectiveness of the design for the application in STEP Cube Lab-II. To demonstrate the effectiveness of stiffeners with viscoelastic acrylic tapes for launch load attenuation of the solar panel, a 3U sized solar panel without using HRM was fabricated and tested according to the number of stiffener attachment conditions through free-vibrations and launch vibration tests. The main objective of the tests was to investigate the panel's dynamic behavior and structural safety with the attached stiffeners. Moreover, the characteristics of the panel in the deployed configuration were investigated under various temperatures to predict its design effectiveness under in-orbit operation. Based on these results, a demonstration model of a highly damped 6U sized solar panel module combined with pogo pin based HRM was fabricated and tested. The holding and release mechanism achieved using a three pogo pin was functionally tested through solar panel deployment tests under ambient room

temperature and a thermal vacuum environment. In addition, the TID and SEE radiation tests of the electrical interface PCB was carried out for radiation hardness assurance of the P-HRM. The design effectiveness and structural safety of the solar panel module were validated through qualification-level launch and in-orbit environment tests.

Finally, Chapter VI presents the conclusions drawn from the analysis conducted in Chapters IV and V. Additionally, a list of future works based on the analysis performed in this dissertation is briefly discussed.

II. STEP Cube Lab-II CubeSat's Power System

A. Overview of STEP Cube Lab-II

The STEP Cube Lab [59] was the first 1U CubeSat developed at the Space Technology Synthesis Laboratory (STSL) of Chosun University in South Korea. The main mission objective was to exploit core space technologies researched in domestic universities and verify these technologies through in-orbit operation of the CubeSat. After the successful operation of the STEP Cube Lab for technology demonstration missions in 2017, the STSL of Department of Aerospace Engineering of Chosun University is developing multispectral earth observation 6U CubeSat "STEP Cube Lab-II" as part of the 2019 cube satellite contest hosted by the Ministry of Science and ICT (MSIT) and organized by the Korea Aerospace Research Institute (KARI). Figure 8 shows the system architecture of the STEP Cube Lab-II mission. The STEP Cube Lab-II has been developed within a collaborative framework of the university and start-up aerospace companies for pursuing educational and technology verification purposes. The STSL of Chosun University and a consortium team of eight domestic organizations, including SOLETOP Co., Ltd., Hanwha Systems Co., Ltd., Viewworks Co., Ltd., Edel Tech Co., Camtic Advanced Institute of Technology, ELM Co., Ltd., MIDI Co., and Sejong University were involved in this project to verify in-country-developed space technologies and demonstrate the unique night time video mode remote sensing capability through CubeSat.

The CubeSat is equipped with three commercial-off-the-shelf (COTS) remote sensing instruments onboard as the primary payload for earth remote sensing, such as an electro-optical camera (EOC), a broad band infrared camera (BBIRC), and a long-wave infrared camera (LWIRC). The CubeSat's primary objective is to carry out the nation's first multi-band earth observation mission on various targets on the Korean peninsula, including Mt. Paektu, which has recently shown signs of a volcanic eruption, observation of areas affected by forest fires and the route of spread in areas where forest

fires have occurred, analysis of thermal island phenomenon in urban areas of metropolitan cities, observation of ship activities, observation of seawater coolant discharge at nuclear power plant operation, by utilization of CubeSat's electro-optical (EO) and infra-red (IR) images and videos. Furthermore, the space technologies to be verified in this mission are an optimized method for data compression in the payload data handling system (PDHS) and payloads data transmission system (PDTS) for video data processing/transmission to the ground station. Moreover, the verification of a VMLSA for ensuring the structural safety of solar cells under launch environments by attenuating the launch loads, a P-HRM for high holding constraint on the solar panels during launch and reliable release action in space, and a SADA for the acquisition of power maximization were secondary mission objectives. This study is mainly focused on the on-ground experimental validation of design effectiveness and structural safety of VMLSA and P-HRM.
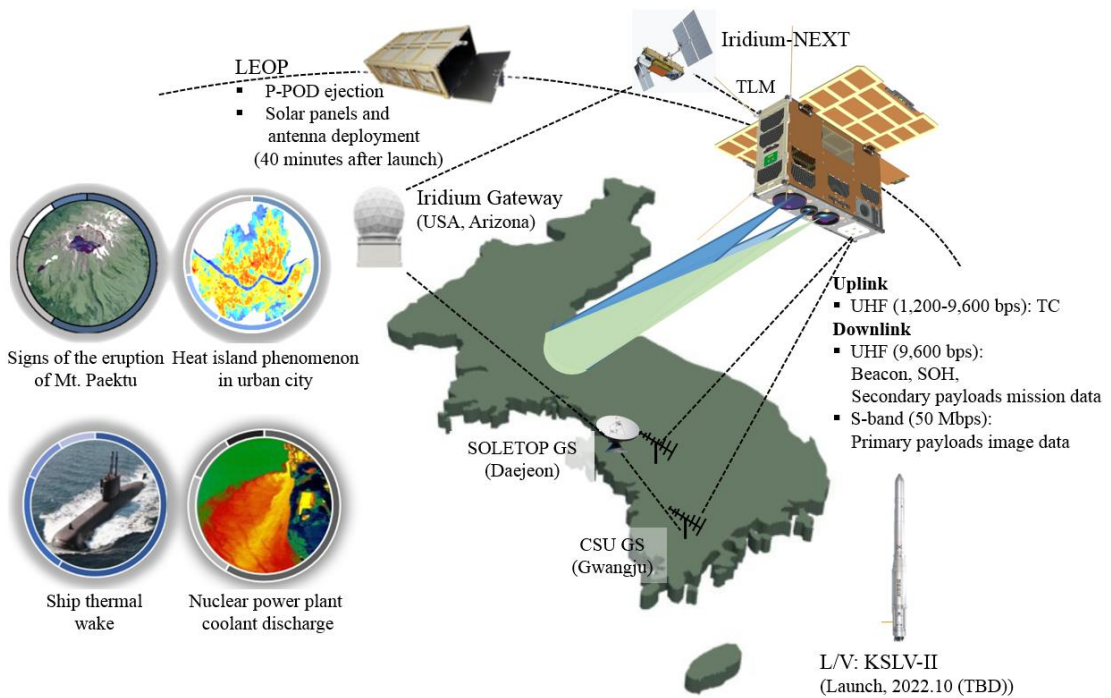
Fig. 8 System Architecture of the STEP Cube Lab-II Mission.

Table 1 presents the system specifications of the STEP Cube Lab-II. For mission operation, the satellite orbit is selected as a sun-synchronous orbit of 700 km altitude and an inclination angle of 97.13° with a local time of descending node (LTDN) of 16:00. The ground station contact time of the satellite calculated from the orbital analysis is approximately 7.5 minutes and access to the ground station occur 6 times a day. The CubeSat is scheduled to be launched in the first quarter of 2022 and mission operation life is set as 1 year.

Table 1 System Specifications of STEP Cube Lab-II.

Items		Specifications		
Satellite Name		STEP Cube Lab-II		
Dimensions (mm)		366 (X) $\times$ 113.7 (Y) $\times$ 240.5 (Z)		
Weight (kg)		7.49		
Orbital Parameter		Orbit: Sun-synchronous Orbit Altitude: 700 km Orbital Inclination Angle: 97.13 deg. LTDN (hr.): 16.00		
Mission Payload		Primary Payloads: EOC BBIRC LWIRC		
		Secondary Payloads: PDHS & PDTS VMLSA P-HRM SADA		
Camera Performance	Camera	EOC	BBIRC	LWIRC
	GSD (m)	10	350	350
	Observation Width (km)	40	220 $\times$ 160	220 $\times$ 160
	Wave Length Range (μm)	0.38-0.94	3-14	9-12
Observation Mission Time		Multi-band Still Imaging Mode: 5.85 sec BBIRC & LWIRC Video Mode: 10 sec		
Ground Station Contact		7.5 Minutes (Average)		
Communication System	Uplink	UHF band 1,200 (GMSK)		
	Downlink	UHF band: 9,600 bps (GMSK)		S-band: > 8 Mbps (16-APSK)
Attitude Control System		3-axis Attitude Control Method		
Mission Life		1 Year		

Figures 9 (a) and (b) show the mechanical configurations of STEP Cube Lab-II in solar panel stowed and deployed state, respectively. The CubeSat's mechanical dimensions and total weight were 366 mm (X-axis) × 113.7 mm (Y-axis) × 240.5 mm (Z-axis) and 7.49 kg, respectively, which is within the 6U standard. The CubeSat mainly consists of COTS components enclosed in an in-country-developed structure, while a few interface boards and mechanical subsystems were designed and assembled by the team.

(a)   (b)
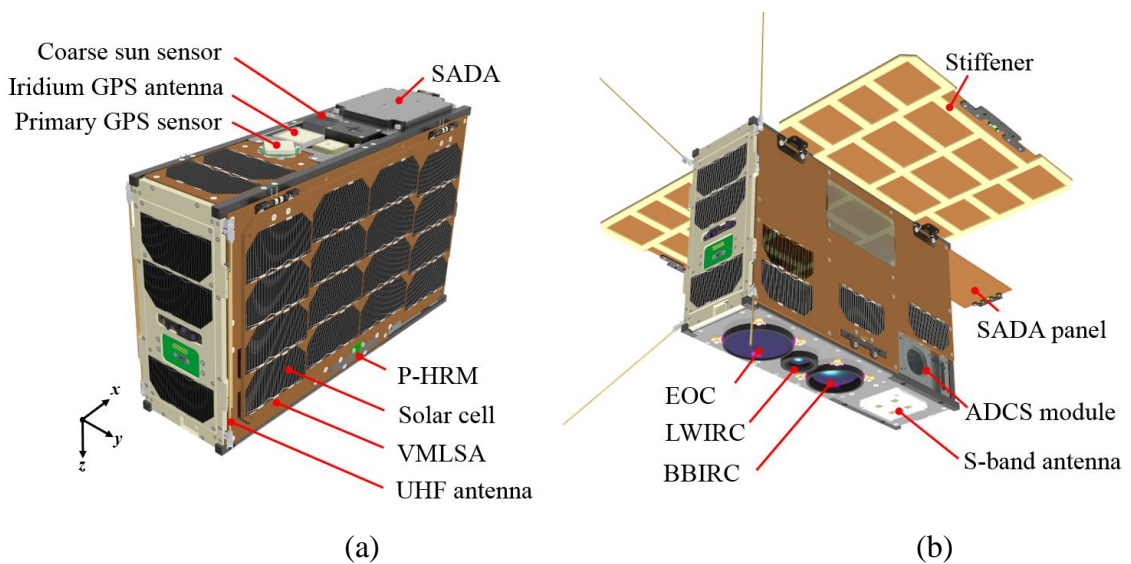
Fig. 9 Mechanical Configuration of STEP Cube Lab-II: (a) Solar Panel Stowed and (b) Solar Panel Deployed.

Figure 10 shows the detailed mechanical configuration of payloads and bus systems. The primary payload consists of three optic and sensor pairs: EOC, BBIRC, and LWIRC, which are designed to operate in staring mode, capable of capturing images and videos nearly simultaneously from the three cameras. The performance specification of EOC is 10 m ground sampling distance (GSD) with a swath width of 40 km, which has a spectral of 0.38-0.94 μm wavelength. The GSD and swath width of the BBIRC and LWIRC are 350 and 220 × 160 in the wavelength range of 3-14 μm and 9-12 μm, respectively. The maximum estimated observation time of EOC still imaging mode and dual-IR video

mode on the Korean peninsula during one orbit period is 5.85 sec and 10 sec, respectively. All commands uplink, as well as downlinks of images and telemetry will be performed by using the ultra-high frequency (UHF) amateur band at a frequency of 1,200-9,600 bps. Additionally, the communications between the CubeSat and the ground station for the data transmission are accomplished by an S-band antenna of greater than 8 Mbps capacity. Furthermore, the attitude control of the satellite is achieved by the 3-axis attitude control method by the application of the XACT-15 attitude determination and control system (ADCS) [60]. To optimize the in-orbit power generation capability from the fixed-type deployable solar panels, the attitude of the CubeSat was set in such a way that the deployable solar panels always point towards the Sun direction by 90-degree roll maneuver of the CubeSat from the nadir pointing attitude, except for the periods of mission operation and ground contact.
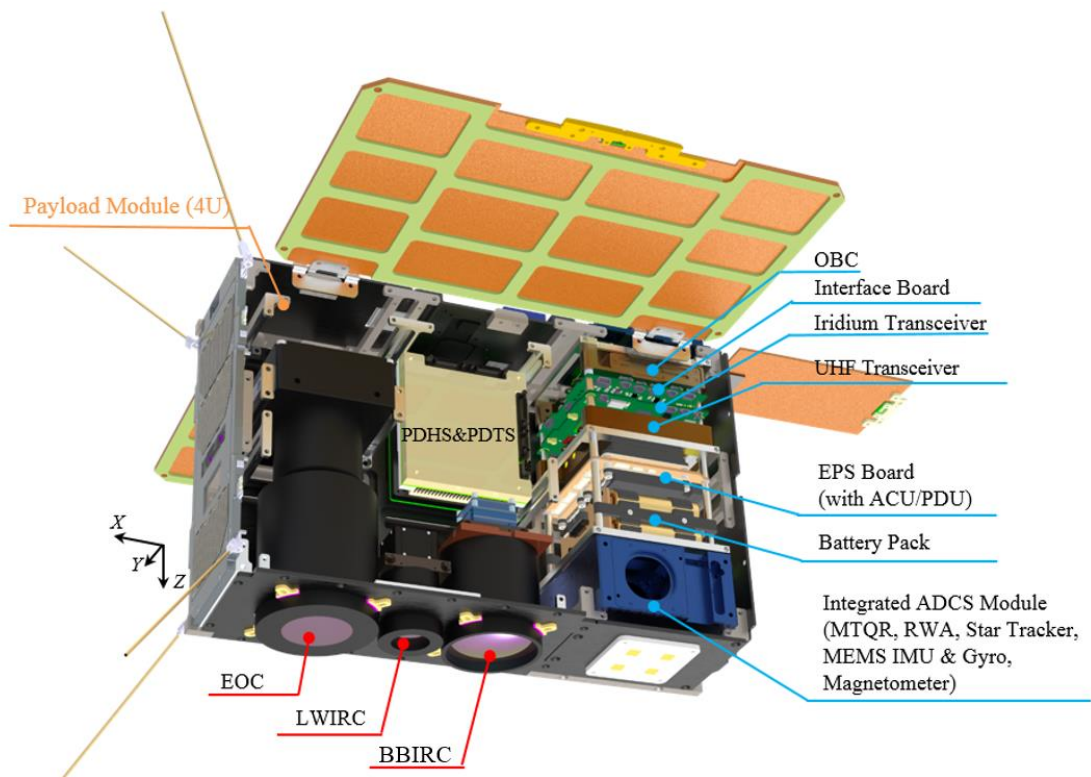
Fig. 10 Detailed Mechanical Configuration of STEP Cube Lab-II's Payloads and Bus Systems.

B. Operation Concetps and Scenarios

A satellite is characterized by a well-defined set of operational modes, beginning from the process of launch to its disposal and at each stage of the mission, the concept and operational consequences are relevant steps in the design and manufacture of any space mission. This is essentially a discipline of system engineering and has to take into account the complete life-cycle of a satellite, in particular its operational constraints and requirements. Figure 11 shows the conceptual architecture to support the operation modes and scenarios of the STEP Cube Lab-II for the acquisition of mission success. To support the primary and secondary mission objectives, STEP Cube Lab-II has mainly three-phase of operation: safe-hold phase, mission operation phase, and ground contact phase. The satellite operation is defined at the most basic level by the mode; a general functionality tree that defines which tasks can be performed at a given point to satisfy logic and command defined goals. An example of such a mode would be the earth observation modes, in which the satellite seeks to image and videos of a specific target. For mode transition, we have two cases, either the ground operations drive the complete satellite mode transition down to each reconfigurable hardware and software unit by executing a step-by-step procedure and uploading the related telecommands, or the ground operator sends telecommands to trigger a mode transition with the satellite converting it into a series of on-board operations for the subsystem reconfiguration. A limited level of onboard autonomy can be sufficient for the mode transitions because the low earth orbit (LEO) satellites can be operated in a quasi-real-time fashion. A mode is comprised of many sub-modes; a unique set of tasks that further define each individual goal within a mode. The sub-modes is executed autonomously, and sequentially.
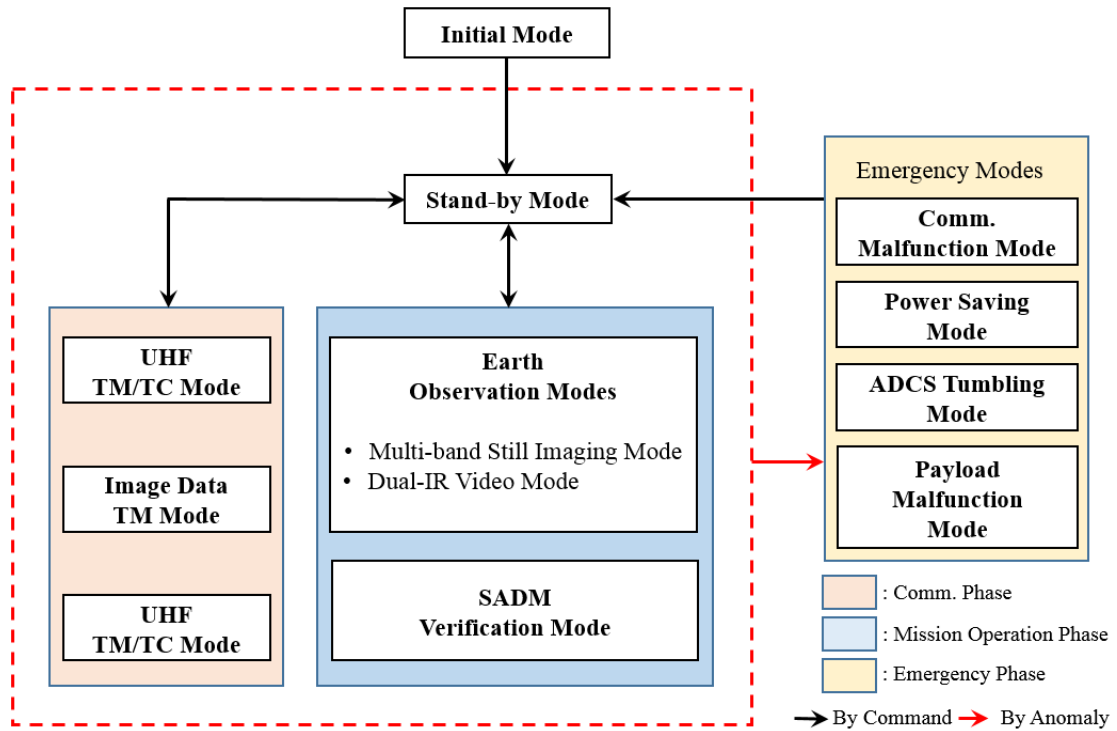
Fig. 11 Conceptual Architecture to Support Operation Modes and Scenarios.

1. Initial Mode

The initial mode is the satellite's initial operation mode in which the Kill switch operates immediately after the satellite is ejected from the P-POD. During the initial mode, the satellite batteries are powered, the communication band receivers and transmitters were on, and the satellite communication buses are initialized. After having enabled all the analog and digital acquisition/commanding lines, the on-board computer (OBC) automatically starts the separation sequence and executes the solar panels and antennas deployment at 40 minutes. Furthermore, the attitude of the satellite is stabilized by obtaining the solar vector with the ADCS and Sun sensor.

2. Stand-by Mode

The standby operation mode initiates before switching to mission mode, communication mode, and emergency mode. The satellite acts as an in-orbit spare not used for any operational service but able to become operational within a short time frame.

The satellite is three-axis stabilized ensuring the required high pointing accuracy of +Z face towards the Earth in order to provide mission product data and services, once configured for the mission operation otherwise the attitude of the satellite is maintained in such a way that solar panels pointing towards the Sun direction by roll maneuvering, in an autonomous way. During this period, the continuous wave (CW) beacon cross transmits the real-time state of the health (SOH) of the satellite via UHF amateur frequencies. This provides enough information to allow operators to make appropriate decisions and immediately identify potential issues. Full health and safety activities are maintained, including continuous real-time monitoring.

3. Communication Phase Mode

The communication phase mode includes communication to the ground station via the UHF, mission data transmission mode via S-band antenna and communication with iridium. The satellite communicates with the ground-station upon receipt of a ground station command then sends stored SOH data from the satellite to the ground station through the UHF band. Moreover, the onboard iridium transceiver communicates with the ground station through the iridium satellite network and receives beacon signals and real-time SOH.

4. Mission Operation Mode

The STEP Cube Lab-II mission operation mode mainly encompasses earth observation mode and SADA verification mode. The earth observation mode is divided into three parts including still image mode, BBIR movie mode, and LWIR movie mode. The image still mode; acquiring image still data from EOC, BBIRC, and LWIRC. Similarly, the satellite's LWIR and BBIRC movie mode obtains video data generated by LWIRC and BBIRC, respectively. All photos and video data obtained were stored in PDTS memory, and the satellite switched to standby mode. In addition, after receiving the commands from the ground station the SADA verification mode initiates, then store

the acquired SADM deployment status signal data in the system, and switch to standby mode.

5. Emergency Mode

The satellite enters the emergency mode under critical on-board anomaly detection, which cannot be autonomously recovered or which, though recovered, could present a risk later on its normal operations are continued. The emergency mode is divided into four categories according to the types of events and faults, such as communication failure mode, power-saving mode, ADCS tumbling mode, and payload failure mode. No communication is made with the ground station in the communication malfunction mode for up to 7 days, the system checks communications system malfunction and sends the telecommunications information to the ground station. The ground station will receive a beacon every minute until the communication of the satellite with the ground station is made again. Then switch to standby mode when communication with the ground station is made. Furthermore, the satellite system enters the power-saving mode, if the low-power battery mode is (DOD 80%) then minimizing the operation of all components of the system except essential H/W's functions when the battery DOD is less than 20%, the system switch to standby mode. Furthermore, the ADCS tumbling mode states that if the angular velocity of the satellite's *x, y*, and *z*-axis position is greater than 3 deg./s, it is considered to be a satellite tumbling state and switched to the control mode out of position. Using ADCS, posture control is performed until the angular deviation is lowered to less than 0.3 deg./s then switches to standby operation mode after finishing the attitude stabilization. The payload malfunction mode states when the system detected malfunctioning on the payloads functions. The onboard system will verify the malfunctioning factor and it has been removed from the SOH data after off/on malfunction mode. Return to normal operations if the malfunction and anomalies were completely carried out under ground control.

C. Power Status of the Hardware's in Mission Operation Mode

The electrical power system (EPS) provides, stores, distributes, and controls satellite electrical power. The most important sizing requirements are the demands for average and peak electrical power with the orbital profile. The power budget is associated with power generation and consumption of the satellite power system, it can estimate the net power balance of the system while in different operation modes. The power consumption can vary according to modes of operation due to the power on/off status of the hardware. Table 2 shows the power on/off status of the hardware according to the operation mode in each task. This power status information is used to calculate the power consumption by the payloads and sub-systems in each operation phase of the satellite. According to the power status listed in the table, the highest power-consuming phase is the mission operation period because the maximum member of hardware was consuming power as compared to the other operation modes. Thus, the total power consumption by the components in the mission operation phase is used as a worst-case scenario for energy balance analysis.

Table 2 Power On/Off Status of the Hardware's in various Operation Mode of the Satellite.

H/W		Initial Op.	Normal Op.	Comm.			Mission Op.				Emergency			
							Earth Observation Mode			SADM Ver.	Power Saving	ADCS Tum.	Comm. Mal.	Payload Mal.
		Initial	Stand-by	(UHF)	(S-band)	Iridium	Still Image	BBIRC movie	LWIRC Movie					
EOC		Off	Off	Off	Off	Off	On	Off	Off	Off	Off	Off	Off	Off
BBIRC		Off	Off	Off	Off	Off	On	On	Off	Off	Off	Off	Off	Off
LWIRC		Off	Off	Off	Off	Off	On	Off	On	Off	Off	Off	Off	Off
SADM		Off	Off	Off	Off	Off	Off	Off	Off	On	Off	Off	Off	Off
PDHS Module		Off	Off	Off	Off	Off	On	On	On	Off	Off	Off	Off	Off
PDTS Module		Off	Off	Off	On	Off	On	On	On	Off	Off	Off	Off	Off
OBC Board		On	On	On	On	On	On	On	On	On	On	On	On	On
EPS Board		On	On	On	On	On	On	On	On	On	On	On	On	On
ADCS Module		On	On	On	On	On	On	On	On	On	On	On	On	On
Sun Sensor	Coarse	On	On	On	On	On	On	On	On	On	On	On	On	On
	Fine	On	On	On	On	On	On	On	On	On	On	On	On	On
GPS Receiver Module		Off	On	On	On	On	On	On	On	On	Off	Off	Off	Off
Comm. Board	Rx	On	On	On	On	On	On	On	On	On	On	On	On	On
	Beacon Tx	On	On	On	On	On	On	On	On	On	On	On	On	On
	FM Tx	Off	Off	On	Off	Off	Off	Off	Off	Off	Off	Off	Off	Off
Iridium Transceiver Module		Off	Off	Off	Off	On	Off	Off	Off	Off	Off	Off	Off	Off
Solar Panel HRM		On	N/A	N/A	N/A	N/A	N/A	N/A	N/A	N/A	N/A	N/A	N/A	N/A
UHF Antenna HRM		On	N/A	N/A	N/A	N/A	N/A	N/A	N/A	N/A	N/A	N/A	N/A	N/A

D. Power Consumption

Table 3 summarizes the estimation of power consumption by the payloads and sub-systems in the LWIR video mode of the earth observation phase. The LWIR video mode of the earth observation phase is the most power-consuming phase as compared to the other operation modes. The required power was calculated using the operating voltage and currents provided by each component's datasheet. The power usage of subsystems is weighted using their duty-cycles to get the orbit average consumption of the system. The power consumption by the communication system is based on the ground contact

and data transmission period per orbit of the satellite. The total power consumption of the CubeSat in LWIR video mode with a 10% contingency margin is 15.13 W.

Table 3 Power Consumption in LWIR Video Mode of Earth Observation Period.

Item			Nominal Power (W)	Peak Power (W)	Duty (%)	Consumption Power (W)
Payload	Cameras	EOC	0.00	6.00	0.00	0
		BBIRC	0.00	1.20	0.00	0
		LWIRC	0.00	1.50	5.00	0.0075
	PDHS Module		0.00	15.00	5.00	0.075
	PDTS Transmitter (X-band)		0.40	12.00	5.00	0.4362
	SADA		0.80	2.30	0.00	0.8
C&DH	OBC		1.30	2.00	50.00	1.65
	IFB		0.60	3.00	50.00	1.8
EPS	PCDM		0.26	1.00	50.00	0.63
	Battery		0.00	0.06	100.00	0.064
ADCS	ADCS Module		2.25	17.50	20.00	5.3
	Coarse Sun Sensor		0.00	0.12	5.00	0.006
	Fine Sun Sensor		0.00	0.20	5.00	0.01
	GPS Receiver		0.72	1.60	20.00	0.896
CS	UHF Comm. Board		0.80	2.50	6.00	0.902
	UHF Comm. Antenna		0.00	0.17	100.00	0.165
	Iridium Transceiver		0.67	12.00	3.00	1.01184
Contingency Margin (10%)						1.38
Total Power Consumption (W)						15.13

E. Power Source

The STEP Cube Lab-II will be equipped with two deployable solar panels, and a 2U sized SADA panel for the optimal orientation of the solar cells in the Sun direction to satisfy the onboard power requirements of operating modes. Figure 12 shows the configuration of solar panel cell strings. The Azure space 30% efficiency triple-junction GaAs solar cell (3G30C) [61] of dimensions $80 \times 40 \times 0.15$ mm were considered for the analysis. The composition of the solar cells in the CubeSat was as follows: 16 cells were mounted in each deployable solar panels, 3 solar cells in the CubeSat structure's $+X$ and $-X$ axis, 4 solar cells in $+Y$ and $-Y$, 2 solar cells in $-Z$ axis surface and 3 solar cells were mounted in the SADA panel. The color distinct of the solar cells represents the parallel strings of series cells that were determined based on the voltage and current requirement by the system. The attitude of the CubeSat was set in such a way that the deployable solar panels always point towards the Sun direction by 90-degree roll maneuver from the nadir pointing attitude, except for the period of mission operation and ground contact.
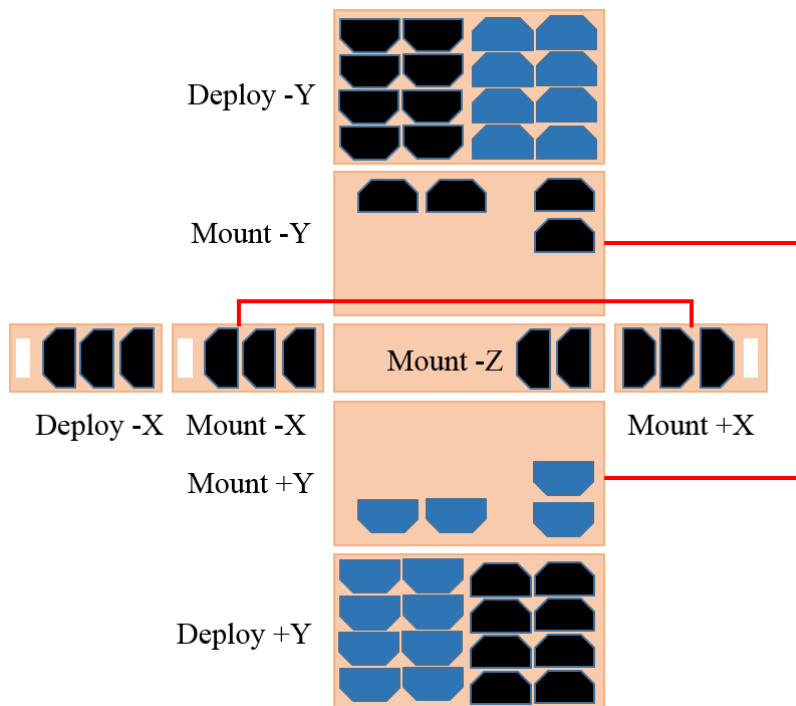
Fig. 12 Composition of Solar Cells in the CubeSat.

Table 4 shows the mechanical and electrical specifications of the triple junction (TJ) solar cell 3G30C. The 3G30C solar cells offers best end of life (EOL) performance values and should be combined with an external bypass diode protection. The average power generates in an orbit of the STEP Cube Lab-II should be greater than 15.13 W. Thus, a comprehensive power balance analysis is performed in order to ensure the sufficient power margin to the payloads and bus-system for the acquisition of successful missions [62] throughout the mission lifetime of the CubeSat.

Table 4 Specifications of Azur Space's TJ Solar Cell 3G30C [61].

Item	Details
Base Material	GaInP/GaAs/Ge on Ge Substrate
AR-coating	$TiOx/Al2O^3$
Dimensions (mm)	$40 \times 80 \pm 0.1$
Cell Area (cm^2)	30.18
Average Weight (mm/cm^2)	≤ 86
Thickness Without Contacts (µm)	150 ± 20
Contact Metallization Thickness Ag/Au (µm)	4-10
Average Open Circuit Voc (mV)	2700
Average Short Circuit Isc (mA)	520.2
Voltage at Max. Power Vmp (mV)	2411
Current at Max. Power Imp (mA)	504.4
Average Efficiency at 1367 W/m^2 (%)	29.5

F. Power Generation

The calculation of the power generation capabilities of a satellite's solar array is complex, requiring consideration of the satellite's orbit, attitude, panel layout, the sun position, and eclipse the satellite experiences [63]. The FreeFlyer program was used in a simulation to calculate the power generation and battery power estimation and its performance was analyzed with satellite operational modes. The FreeFlyer is a COTS software application for space mission design, analysis, and operations which has been independently verified and validated for flight-tested, proven accuracy, and is used for spacecraft analysis and operations by NASA, and commercial satellite manufacturers companies. This power simulation tool could be used not only to calculate the suitable power budget when developing the power system but also to analyze the remaining energy balance in the satellite. The power generated by the solar panels must be greater than the power consumption by the satellite subsystems. If the in-orbit generated power is lower than the consumed power, the satellite may stop operating or the life of the satellite may be reduced. The energy balance analysis of the satellite in low earth orbit was performed to verify the efficiency of mission and energy balance by predicting DOD, bus voltage, and charge/discharge currents. The power estimation is helpful either for the sizing of the power sources and energy storage or for defining the operation modes of the CubeSat with the energy available.

1. Orbital Parameter

In CubeSats, the calculation of the incident solar energy according to the orbital parameters and satellite attitude is important for the design process of the electrical power system because of the restraint surface area for solar cell attachment [64]. The basic orbital parameters of the STEP Cube Lab-II are listed in Table 5. The Sun-synchronous orbit of altitude 700 km from the Earth's surface of LEO is selected based on the mission operation parameters. The orbital inclination and period of the satellite according to the LTDN of 16:00 hour will be 98.13 degrees and 98.76 minutes, respectively. The power simulation analysis is performed with the assumption of the

LTDN information provided by the launch provider. The satellite is scheduled to be launched in the first quarter of 2022.

Table 5 Orbital Parameters of the STEP Cube Lab-II CubeSat.

Parameter	Specification
Orbit	Sun-synchronous Orbit
Altitude (km)	700
Orbital Inclination (deg.)	98.13
Orbital Period (s)	5,926
LTDN (hr)	16:00
Mission Lifetime (yr)	1
Launch Date (YY/MM)	2022/10

Figure 13 shows the orientations of the CubeSat during the orbit according to the mission and idle mode phases. The attitude control of CubeSat is set in such a way that during the idle mode in orbit, CubeSat rolls in the direction of the Sun for the solar panel pointing to the Sun, and the satellite rolls back to the nadir pointing attitude in the mission performance period. Thus, deployable solar panels orientate always in the Sun pointing by satellite attitude maneuver except for the imaging and ground contact periods that could enhance the power generation capability of the CubeSat even with the application of fix type deployable solar panel. Sanjuan et al. [65] compare the incident solar energy and battery storage in a 3U CubeSat satellite in different orientation scenarios such as nadir-pointing, Sun-pointing, and free-orientation. According to the results, more solar energy can be harvested by the solar cells in the sun-point and free-orientation scenarios; however, the free-orientation is effective specially for the body-

mounted solar cells and it depends on the initial torque. Oh and Park [11] investigated feasibility of concentrating photovoltaic power systems for CubeSat applications in various rotation angles of irradiation source and the angle between the irradiation source and solar panel through ground-based experiment. Etchells and Berthoud [66] developed a MATLAB based power modelling tool for analyzing CubeSat solar power generation. The power model is designed to allow satellite orbit customization, along with a range of attitudes and solar panel configurations, including deployable panels.
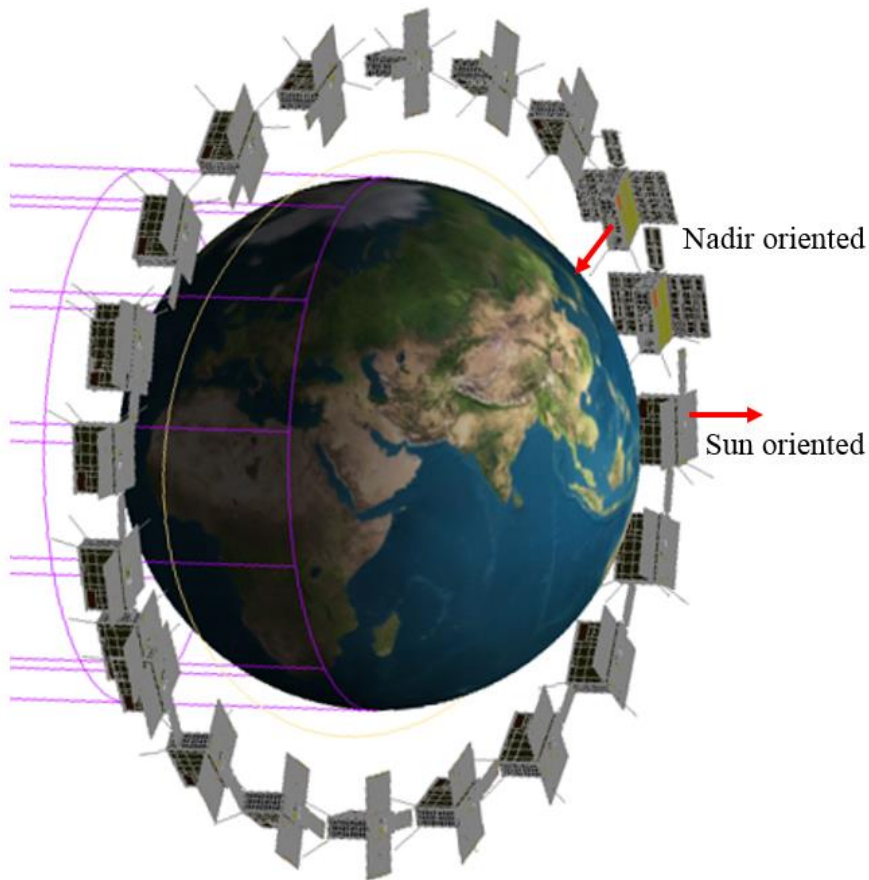
Fig. 13 Orientations of the CubeSat During an Orbit According to the Earth-imaging and Idle Modes.

2. Power Simulation Result

The CubeSat's power analysis is performed by FreeFlyer software in accordance with the orbital information mentioned in Table 1. Figures 14, 15, and 16 show the power simulation results of the STEP Cube Lab-II according to the roll maneuvering angle towards the Sun direction from the nadir pointing attitude.
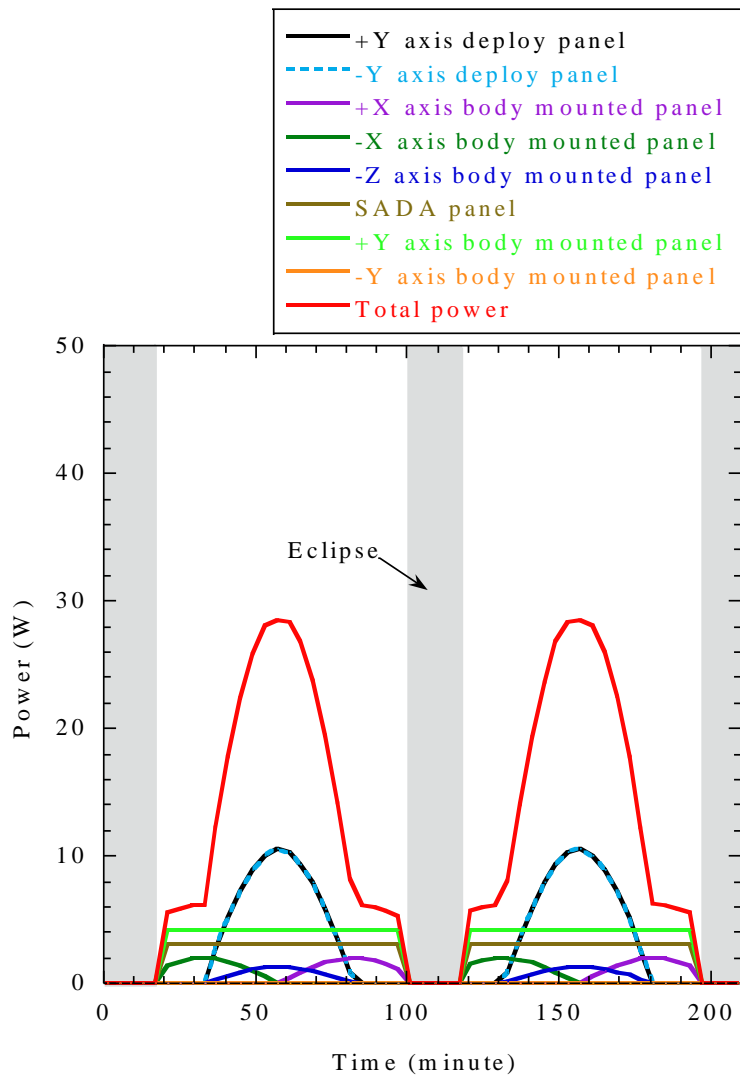
Fig. 14 Power Analysis Result of the CubeSat without Roll Maneuvering (Nadir Point Attitude).
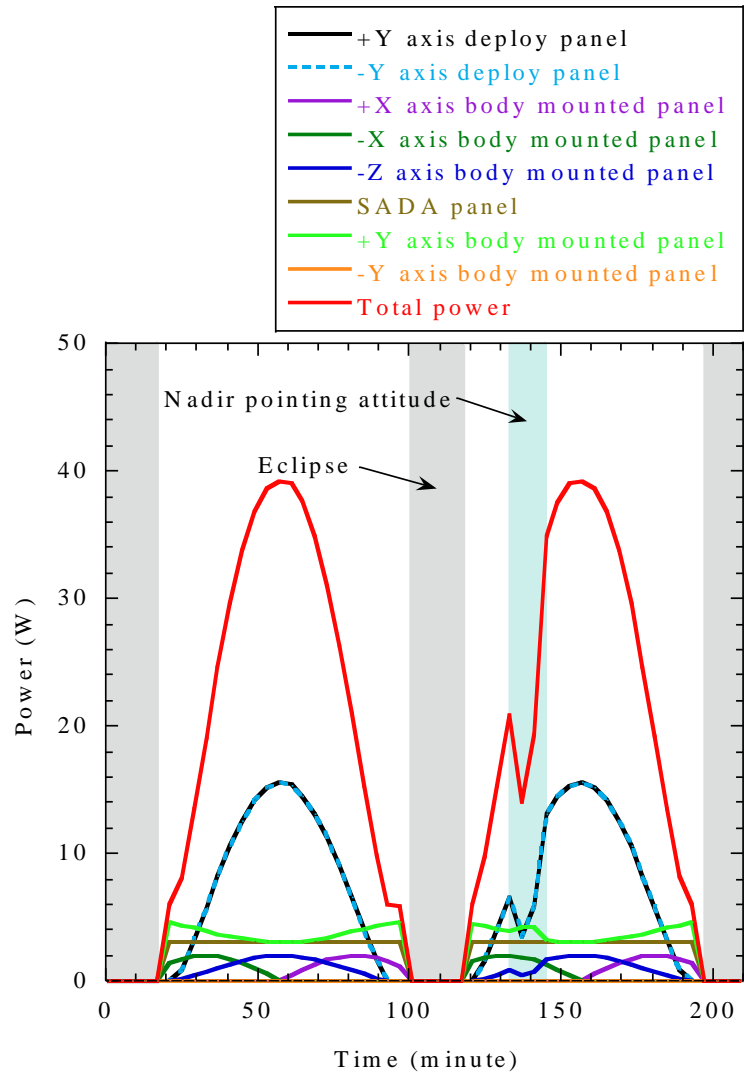
Fig. 15 Power Analysis Result of the CubeSat at 20 deg. Roll Angle Maneuver.
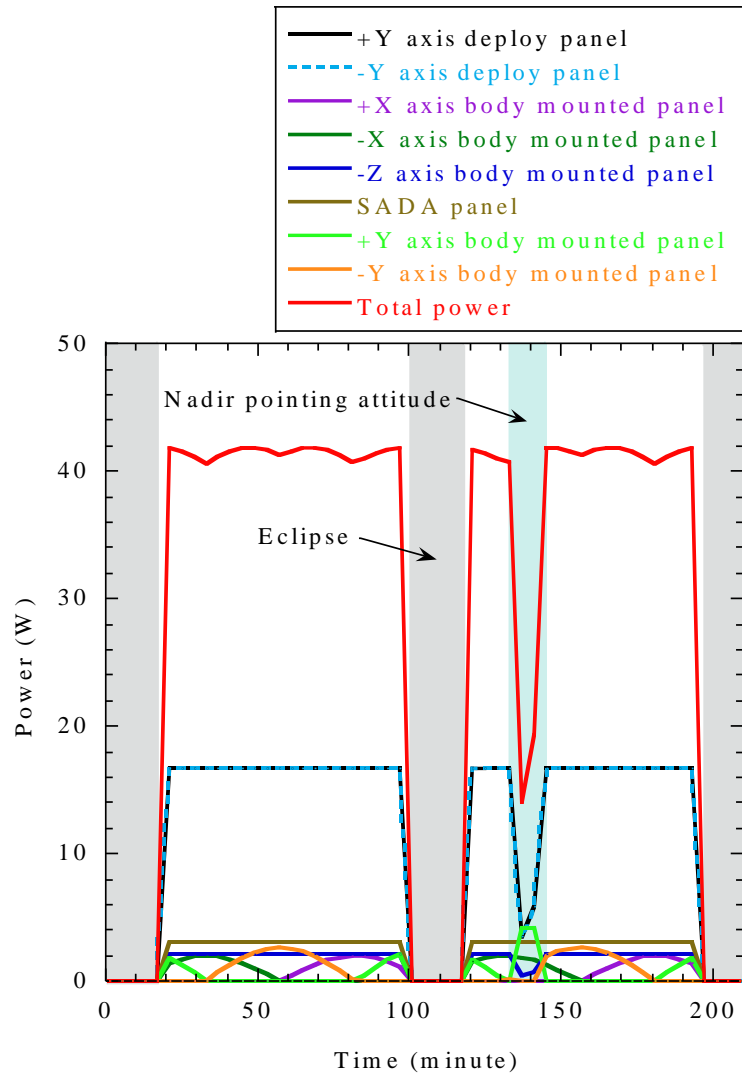
Fig. 16 Power Analysis Result of the CubeSat at 90 deg. Roll Angle Maneuver.

Table 6 lists the peak and average power generation of the CubeSat according to the roll maneuvering angle towards the Sun direction. The maximum peak power and average power generation at 90 deg. roll angle maneuver were 41.84 W and 41.46 W, respectively. The average power generation at 90 deg. maneuver is higher by a factor of 2.74 than that of the CubeSat with nadir pointing attitude in orbit. The results indicate that the in-orbit power generation capability of the CubeSat can be substantially increased with the roll maneuver of the CubeSat for pointing the solar panel toward the

Sun direction this is owing to the solar intensity variation on the solar cells with Sun angle.

Table 6 Power Generation Capability of the CubeSat According to Roll Maneuver Angle.

Roll Maneuver Angle (deg.)	Peak Power (W)	Average Power (W)
0	28.55	15.11
20	39.12	23.79
90	41.84	41.46

G. Energy Balance Analysis

Energy balance analysis (EBA) is carried out to check whether the generated power of the satellite is balanced with the power consumption and the stored power. The magnitude of each power generation from the deployable solar panel and body mounted solar cells are approximated during the orbit of CubeSat. The power status of the CubeSat in orbit is predicted according to power consumption at mission modes so that the power produced from the solar panel during daylight, the power consumed in each subsystem, and the power stored in the battery maintain the optimal condition. The satellite power estimation is also helpful to predict the state of charge of the battery in standby mode, allowing for the determination of battery health and life cycle in orbit.

Table 7 shows the energy balance analysis of the STEP Cube Lab-II in worst case power consumption scenario, the LWIR video mode of Earth observation. The average power generation of the CubeSat is considered from the power simulation result at 90 deg. roll angle. The total power consumption by the satellite system during the LWIR video mode of Earth observation phase is 15.13 W. The residual energy after for eclipse after the 0.9 percent deduction for battery charge regulator (BCR) is 30.80 Wh. The

result shows that the power margin of the satellite in an orbit is 26.87 Wh after subtracting the worst case power consumption in eclipse period, which is 49.86 % of the generated power during daylight period. The energy balance analysis results shows the CubeSat have sufficient power margin while the satellite is 90 degree roll maneuvering towards the Sun direction. The power budget percentage will be negative while satellite is nadir pointing because the average power generation in an orbit is only 10 W that is less than power consumption by the payloads and sub-systems in standby mode.

Table 7 Energy Balance Analysis in Worst Case Power Consumption Scenario.

Time (min)		Parameter	Power (W)	Energy (Wh)	Remarks
Daylight	78	Generation	41.46	53.89	-
		Consumption	-15.13	-19.66	-
Residual Energy (for eclipse)				34.23	-
				30.80	BCR Eff.=0.9
Eclipse	19	Consumption	-12.43	-3.93	-
Power Margin (Wh)				26.87	-
Power Budget (Margin/Generation,%)				49.86	Req. : > 0 %
Battery DOD (%)				5.89	Req. : < 20 %

Figure 17 shows the energy balance analysis of the CubeSat in attitude of 90 deg. roll from the nadir pointing to the Sun pointing direction. The results shows that battery is fully charged during each daylight period of the orbit. The DOD percentage of the battery is determined through the following equation:

$$DOD\ (\%) = \frac{Power\ Consumption\ (W) \times Eclipse\ Period\ (h)}{Battery\ Capacity\ (Wh)} \times 100\% \quad (2.1)$$

The battery DOD in an orbit can be easily estimated if we know the total electrical power used by the sub-system and payloads during an eclipse period, the time taken by the satellite during the eclipse in hour and the overall battery pack capacity. The satellite's power consumption during the eclipse period where the satellite is in standby mode is 12.43 W, determined from the hardware's power on/off status. The calculated max. DOD based on the energy balance analysis of the STEP Cube Lab-II with the maximum battery pack capacity of 77 Wh is 5.11 %, which is within the system requirement of maximum 20 % DOD. The result shows that battery is able to fully charge during the daylight period of each orbit.
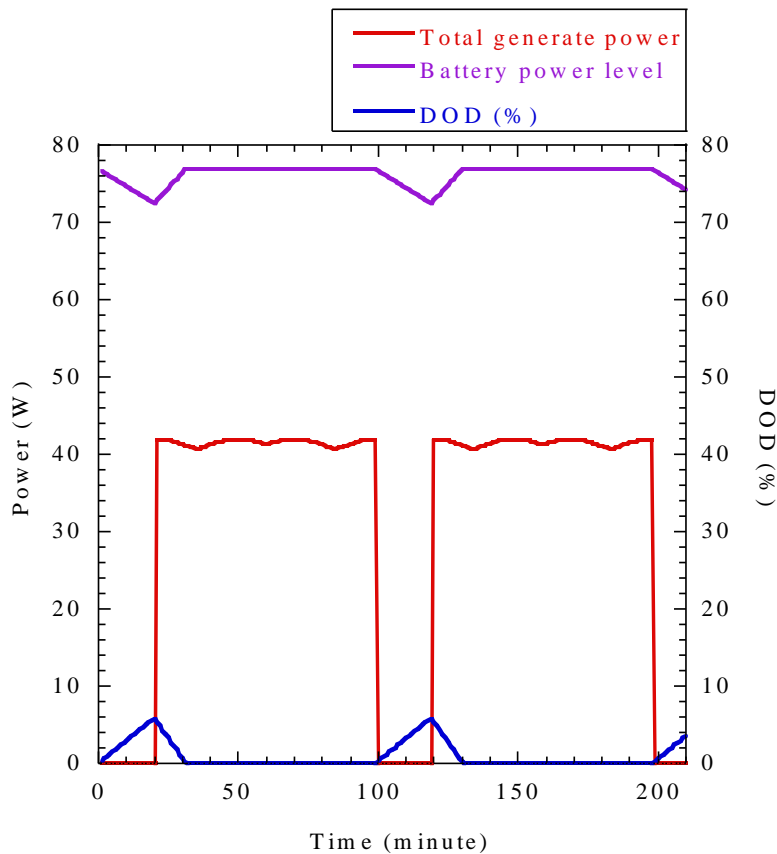
Fig. 17 Energy Balance Analysis of the CubeSat at 90 deg. Roll Maneuver.

H. Battery Life Cycle

To assure the battery charge-discharge capacity until the end of the mission life, the maximum discharge depth should be less than 20 percent of the actual capacity, which is the system requirement that defines the battery pack capacity to be used in the EPS based on the EBA result. The required battery capacity can be determined by the above DOD equation (2.1). The power consumption in an eclipse is approximately 12.43 W, thus the total power drawn from the battery during 19 minutes of the eclipse is 3.94 Wh. To fulfill the least DOD requirement of 20 %, the battery capacity shall be at least 19.7 Wh. Thus, the NanoPower BPX of 77 Wh capacity [67], lithium-ion battery pack manufactured by GomSpace is proposed for the STEP Cube Lab-II based on the energy balance analysis that has temperature sensor and heater for better battery performance. The NanoPower BPX is comprised of eight 18650 lithium-ion cells of capacity 2600 mAh, which can be configured for nominal voltages ranging up to 29.6 V. This battery provides a variety of option for customization such as two cells in series with four parallel, four cells in series two parallel, and all eight cells in series by realizing that the different applications have different requirements to a power system. When choosing batteries for a satellite mission it is important to make sure that they can withstand the hostile environment encountered in space. The GomSpace batteries provide flight heritage and extensive testing and are chosen specifically for their suitability in satellite missions [68].

Table 8 shows battery life cycle approximation for the 1-year orbital cycle of the CubeSat. The maximum number of dawn-dusk cycles that the CubeSat will complete in an orbital period of one year is approximately 5475 by taking 15 cycles a day. The NanoPower BPX consists of eight lithium-ion batteries, the cumulative charge and discharge cycle is 5000 while connecting them in series. If we make the battery composition of four cells out of eight in series and link them in parallel, the 10,000 charges and discharge period can be achieved. The results show that the composition of the battery should be 4 cells in series and 2 parallel connections out of 8 cells that ensure

45.25 percent charge and discharge cycle margin relative to the satellite's total orbital dawn-dusk cycles of 1 year.

Table 8 Battery Life Cycle Estimation for the 1 Year Orbital Cycle.

Battery	Li-ion Cell	DOD (%)	Battery Composition	Charge & Discharge Cycle	1 Year Orbit Cycle	Margin	Percentage Margin (%)
NanoPower BPX	8	15	4 Cells Series x 2 Parallel Connection	10000	5475	4525	45.25
			8 Cells Series Connection	5000		-475	-9.5

III. A Highly Damped Deployable Solar Panel Module

A. Design Description

Figures 18 (a) and (b) show the stowed and deployed configuration of highly damped deployable solar panel module proposed in this dissertation for the application of STEP Cube Lab-II, respectively. The solar panel module is mainly composed of a viscoelastic multi-layered stiffener-based solar panel, a pogo pin-based HRM and torsional hinges. Table 9 lists the basic specifications of the STEP Cube Lab-II solar panel module. The solar panel is comprised of a PCB panel, thin PCB stiffeners, and viscoelastic acrylic tapes. The PCB panel is made out of FR4 material with dimensions 325.4 mm × 193 mm × 1.6 mm that provides a mechanical interface for the integration of stiffeners and solar cells. The five layers of thin PCB stiffeners as shown in Fig. 18 made of FR4 material of thickness 0.5 mm were attached on the rear surface of the PCB panel by double-sided 3M^{TM} 966 acrylic tape [69].

(a)   (b)
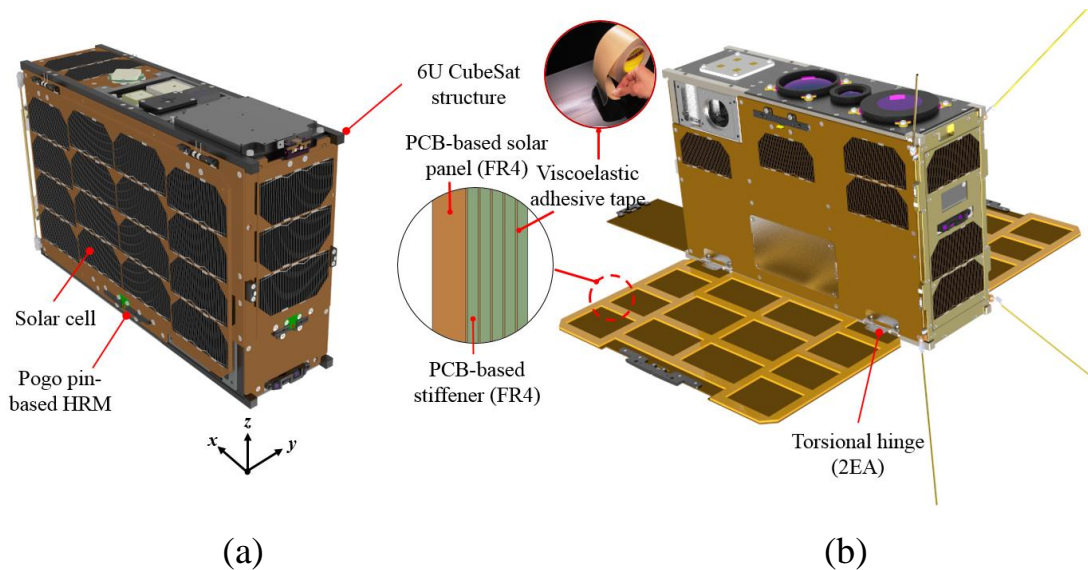
Fig. 18 Mechanical Configuration of STEP Cube Lab-II: (a) Solar Panel Stowed and (b) Solar Panel Deployed.

Table 9 Specifications of the STEP Cube Lab-II Solar Panel Module.

Items		Details
Viscoelastic Multi-Layered Solar Array (VMLSA)	Dimension (mm)	325.4 (L) × 193 (W) × 3.7 (H)
	Total Mass (g)	306.5
	Damping Ratio	0.141
	1st Eigenfrequency (Hz) (Launch Stowed Configuration)	75.0
	Material	FR4 (PCB Panel & Stiffener), Acrylic Adhesive Kapton Tape (Stiffener Attachment)
Pogo Pin-based Holding and Release Mechanism (P-HRM)	Separation Method	Burn Wire Release Mechanism
	Key Features	High Holding Constraint, Separation Spring, Deployment Status Switch
	Max. Repetitive Release	> 10 times
	Allowable Temperature Range (℃)	-15 ~ 60
	Material	Aluminium (I/F Bracket) FR4 (PCBs)
Torsion Hinge	Deployment Method	Torsional Spring-based Hinge
	Solar Panel Latching Method	Passive Latch by Residual Torque of Spring
	Materials	Aluminum (Hinge), SUS304 (Shaft), Delrin (Bushing)

The 3M^{TM} 966 acrylic tape manufactured by the 3M company is a high-temperature acrylic adhesive with low outgassing properties that meet the National Aeronautics & Space Administration (NASA) low volatility specification criteria of ASTM E596. Thus,

it has been used in aerospace applications for bonding purposes. The constrained layer damping with the viscoelastic adhesive material (3M ISD142R) from the same 3M Company has been used for vibration attenuation in the Hubble Space Telescope deployable solar panels damper [70]. The detailed specifications of the materials used in the solar panel are presented in Table 10. The basic principle for attenuating the launch load on the panel is based on the resistive deformation characteristics of laminated adhesive tapes subjected to shear deformation such that the constrained viscoelastic layer dissipates maximum vibration energy.

The manufacturing process of PCB stiffener is simple, the rectangular blocks, as well as a hinge and the HRM portion of the PCB, were intentionally cut out for mass optimization that also allows access to the rear side of the solar panel. Furthermore, the longitudinal and the transverse structural shape of the stiffeners effectively mitigate longitudinal and torsional oscillation of the panel with the combination of viscoelastic acrylic tape. The stiffener attachment process is considerably simple, although intensive care should be given to control the uniform bonding strength distribution in workmanship. The unsymmetrical attachments of acrylic tape would increase pre-stress and delamination in the multi-layered stiffener. Therefore, four guide holes were considered on the four edge corners of the stiffeners and the PCB panel for effortless integration of stiffeners on the panel. The total thickness of the solar panel after integration of the five layers of stiffener on the PCB panel is 3.7 mm that allows an additional margin of 3.3 mm lateral edge gap on P-POD for a dynamic clearance [30]. This constraint layer damping with viscoelastic acrylic tapes strategy could be useful for structural protection of solar cells in a light-weight and compact volume without reducing solar cells accommodation area because fastener interfaces are not required to attach stiffeners on the panel.

Table 10 Specification of Materials used in the Solar Panel.

Item	Details	Value
3M™ 966 Adhesive Transfer Tape [69]	Manufacturer	3M Company
	Adhesive Material	Acrylic
	Color	Transparent
	Thickness (mm)	0.06
	Thermal Conductivity (at 41℃) (W/m/K)	0.178
	Coefficient of Thermal Expansion (ppm/℃)	1.99
	Allowable Temperature (℃)	-40 ~ 232
	Adhesive Strength (to steel) (N/100 mm)	159
	Outgassing (%, TML/CVCM)	0.93 / 0.01
FR4	Elastic Modulus (Pa)	18.73×10^9
	Poisson's Ratio	0.136
	Density (kg/m^3)	1850
	Thermal Conductivity (W/m/K)	0.29

B. Holding and Release Mechanism Using Spring-Loaded Pogo Pins

Park et al. [57] experimentally investigated the feasibility of using spring-loaded pogo pin in wire cutting release mechanism for CubeSat's deployable solar panel. Figure 19 shows the examples of pogo pin. The pogo pin connector comprises a cylindrical barrel, spring, and pin, have advantages such as space-saving connecting, no sliding friction like other spring pins, decrease contact area, friction damage tolerance capability.

Pogo pins are extensively used in automatic test equipment in the form of a bed of nails wherein they facilitate a rapid and reliable connection of the tested devices. The main intention of using pogo pins hardware in the mechanism was as an electro-mechanical connector for the power connecting between the edge of the CubeSat plane and burn resistor PCB integrated in the solar panel, separation spring to initiates the panel deployment, and a status switch to determine the panel deployment status. A demonstration model of the mechanism was fabricated on the 2U sized dummy solar panel and feasibility of the mechanism was evaluated by functional tests under various test conditions such as different input voltages, different numbers of tightened nylon wires, and different temperatures ranges from -40 ºC to 70 ºC. However, in order to employ a pogo pin-based HRM in a real-time CubeSat mission, the mechanism should be qualified under severe launch and in-orbit TV environments, which was investigated later by Bhattarai et al. [58]. The electrical interface of a pogo pin-based HRM was redesigned and it was manufactured as a qualification model. The design feasibility, structural safety, and reliability of the mechanism were verified through functionality tests and launched and in-orbit environment tests.

Fig. 19 Examples of Spring-loaded Pogo pin [57].

In this dissertation, as an extension of the previous research [57] and [58], a new version of two pogo pin based burn wire triggering HRM has been proposed by enhancing the nylon wire tightening interfaces with bracket application rather than using pins and electrical interface modifications for the application in 2U and 3U sized deployable solar panels of CubeSat. Figures 20 (a) and (b) show the close-up view of the newly proposed two pogo pin-based HRM with a fully and partially stowed deployable solar panel, respectively. The mechanical constraint along the out-of-plane direction of the solar panel is achieved by tightening the nylon wire on the guide rail interface of the CubeSat structure side bracket and solar panel side bracket. To release the holding mechanical constraint of the solar panel, a surface-mounted burn resistor is used as an actuator that releases the solar panel by cutting the nylon wire tightened along the guide rail interface of brackets once the mechanism is triggered via the power supply in the circuit.

(a)   (b)
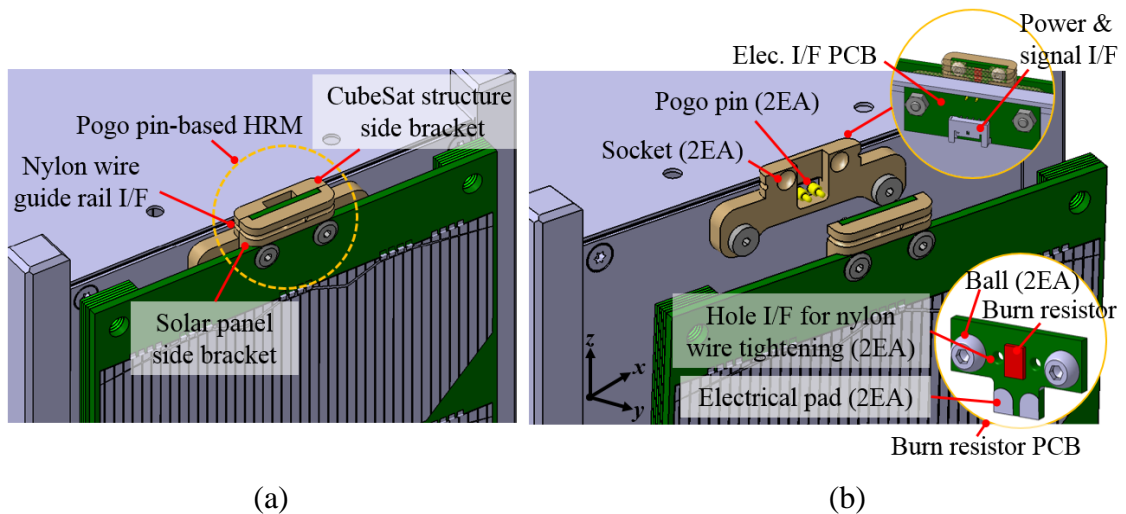
Fig. 20 Close-up Views of Two Pogo Pin-based Mechanism: (a) Fully Stowed and (b) Partially Stowed.

Figure 21 shows the electrical system schematic block diagram of the pogo pin-based Mechanism, which is mainly comprised of a power IC, a NAND gate, an optocoupler, and a PNP transistor for providing power to the burn resistor, and two

buffer ICs with an XOR gate to determine the solar panel deployment signal. In the aforementioned previous studies, a microcontroller unit (MCU) is used to determine the solar panel deployment status. However, in this study, an XOR gate (SN74LVC1G86DBVR) [71] was used in the circuit to utilize the function of pogo pins as a deployment status switch that provides a telemetry of "1" or "0" according to current flow status through a burn resistor, where "1" represents the fraction of input voltage after voltage resistor divider. The functionality of the mechanism is tested by release function tests of the solar panel by implementing in the 3U sized dummy panel, discussed in more detail in the experimental validation section.
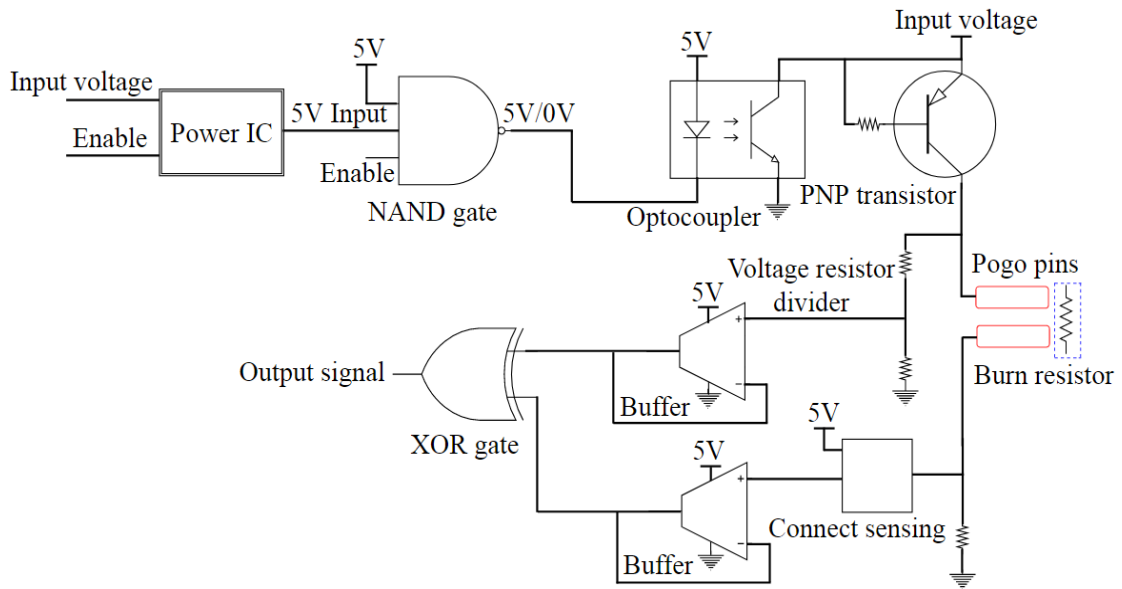
Fig. 21 Electrical System Schematic Block Diagram of Two Pogo Pin-based Mechanism.

1. Three Pogo pin-based HRM

For the application in STEP Cube Lab-II's 6U sized solar panel, we have proposed three pogo pin-based burn wire triggering HRM. The main purpose of using three pogo pins in the mechanism is to simplify the electrical circuit by reducing the electrical components as much as possible for reducing the product's cost and increase its

reliability. Figures 22 (a) and (b) show the close-up view of the proposed three pogo pin-based HRM with a fully and partially stowed solar panel, respectively. The mechanism is mainly composed of pogo pins, electrical interface PCB, burn resistor, burn resistor PCB, brackets, and nylon wire. The key design driver for using pogo pins (MP210-2160-B02 100A, CFE Corporation Co.) [72] in the mechanism was to make a secure electro-mechanical contact between the electrical interface PCB and burn resistor PCB implemented at CubeSat edge and solar panel, respectively, with the intention of providing electrical power to burn resistor during mechanism activation.

(b)   (b)
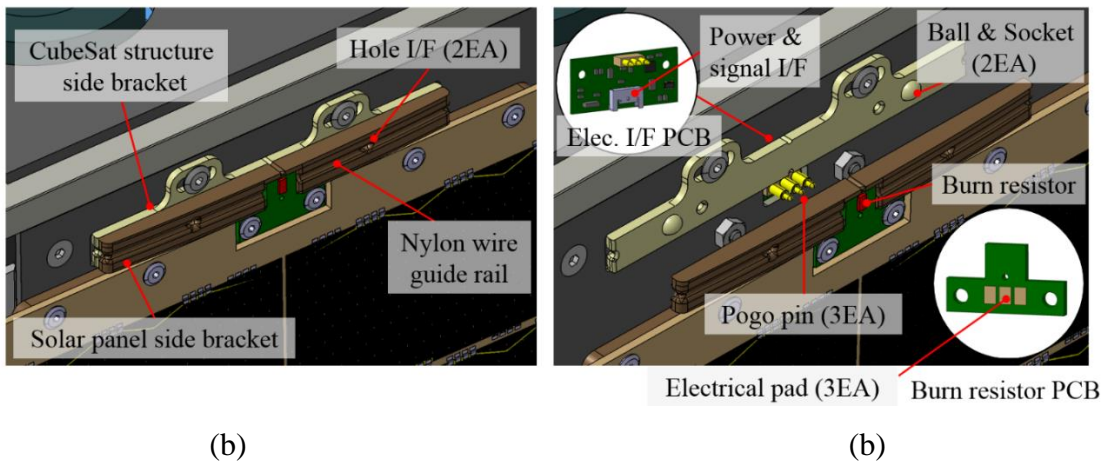
Fig. 22 Close-up Views of the Three Pogo Pin-based Mechanism: (a) Fully Stowed and (b) Partially Stowed.

The mechanical constraint along the out-of-plane direction of the solar panel is achieved by tightening nylon wire on the guide rail interface of the CubeSat structure side bracket and solar panel side bracket. These brackets also allow a mechanical interface to the burn resistor PCB and ball and socket. The CubeSat structure side bracket has a ball-shaped tip on the out of plane lateral surface that acts as a ball and rounding notching on the CubeSat solar panel side bracket is made for the socket. The in-plane direction constraint at the panel is achieved by a combination of ball and socket joints where the socket restricts the movement of ball in a certain nominal gap that

prevents unintentional burden at the tightened nylon wire during launch vibration environment. In addition, this also acts as a mechanical limiter to avoid the undesirable panel strike on pogo pins beyond the range of 1mm working stroke of spring-loaded pin.

For releasing holding mechanical constraint of solar panel, a surface mounted burn resistor (3216 SMD type, Walsin Technology Co.) [73] integrated on the burn resistor PCB is used as an actuator that releases the solar panel by cutting the nylon wire tightened along the guide rail interface of brackets once the mechanism is triggered via power supply in the circuit. The compression force of the spring-loaded pogo pin, 0.78 N ± 0.16 N initiates the panel deployment instantly after the burn resistor thermally cuts the nylon wire that could also quickly or easily interrupt a circuit path to the burn resistor. Then, the passive torsional force of the torsional hinge deploys the solar panel at its intended position. Table 11 lists the basic specifications of the hardwares used in the mechanism.

Table 11 Basic Specifications of the Hardwares used in the Mechanism.

Items	Details	Value
Pogo Pin	Manufacture	CFE Corporation Co.
	Maximum Allowable Voltage and Current (V, A)	12, 3
	Contact Resistance (mΩ)	Max. 50
	Maximum Number of Loadings (Cycle)	50,000
	Qualification Temperature (℃)	-40 ~ 85
	Operation Power of Spring-loaded Pin (N)	0.78 ± 0.16
	Full Stroke (mm)	1.4
	Working Stroke (mm)	1.0
Nylon Wire	Manufacture	YGK
	Material	Fluorocarbon
	Diameter (mm)	0.205
	Max. Allowable Force (N)	88.2
Burn Resistor	Manufacture	Walsin Technology Co.
	Package	SMD Type
	Package Size Code	3216
	Electrical Resistance (ohm)	4.7
	Resistance Tolerance (%)	± 1
	Max. Power Dissipation (W)	0.25

2. Electrical System

Figures 23 (a) and (b) show the electrical interface PCB and the schematic electrical block diagram of the three pogo pin-based HRM electrical system, respectively, which are mainly composed of a power IC, a NAND gate, an optocoupler, and PNP transistor for providing power to the burn resistor, and a buffer IC as an outlet for determination of the solar panel deployment signal. The input voltage to the burn resistor for mechanism activation is set to 8 V, while 3.3 V is supplied to the electrical components, which can be adequately provided by the CubeSat power system using commercial Li-ion batteries in the initial orbital ejection phase. An optocoupler (PC817) [74] was used to prevent electrical malfunction in the circuits at a high voltage. In the optocoupler, electrical signals between two isolated circuits are transferred through light. The input voltage to the burn resistor is set as 8V to reduce the solar panel release time that is accomplish by applying input voltage through the emitter of the PNP transistor. When the PNP transistor is turned on, then the current starts flowing from the emitter towards the base region and finally to the collector that is connected to the burn resistor as a load through pogo pins. The power cutoff function after panel deployment is accomplished through the electrical circuit shown in the block diagram; it did not require a microcontroller unit (MCU), thereby reducing the mechanism's cost.

(a)

(b)
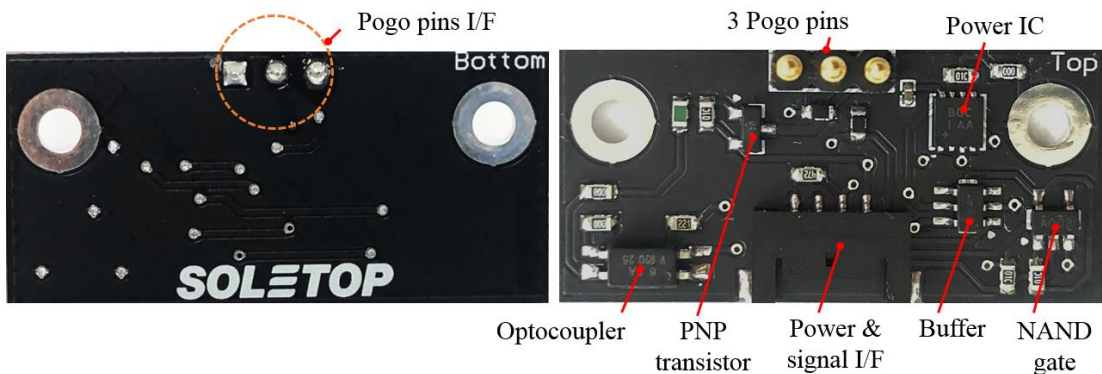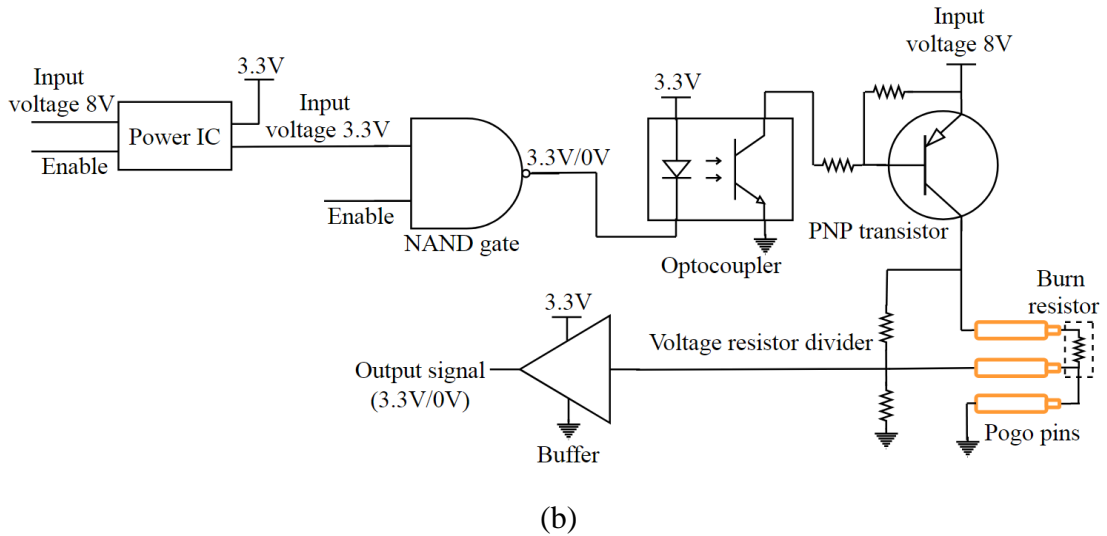
Fig. 23 Electrical System of Three Pogo Pin-based Mechanism: (a) Electrical Interface PCB's Front and Rear View and (b) Schematic Block Diagram.

Figures 24 (a) and (b) show the mechanical configuration of the burn resistor PCB front and rear view, respectively. The burn resistor as an actuator for panel release is soldered on the front side of the PCB, which is facing outward direction while integrating with the solar panel. To interconnect the electrical power coming from the pogo pins to the burn resistor, three surface-mounted electrodes were attached on the rear surface of the burn resistor PCB, which is mechanically connected to the burn resistor internally. The two via hole interfaces were made near the electrodes that are connected to the electrodes physically. In general, the use of thermal via is well known as a method that uses the PCB circuit board to improve the heat dissipation of surface-mounted components. However, the application of via holes here in the burn resistor PCB is to make a more secure attachment of the electrodes on the PCB surface in order to avoid the risk of detachment of electrodes pads due to stress caused by the sharp-edge tip of the pogo pins under launch vibration loads. Bhattarai et al. [58] performed scanning electron microscope (SEM) inspection on the electrode pads after completing all the vibrations tests for the evaluation of the friction and damage caused by the pogo pin tip even though the spring-loaded pin has low friction impact in vibration loads. The

thickness of the electrical contact part, curvature tip on the electrodes was 23.88% reduced value as compared with the initial thickness of 60.37 μm. The impact is minimal, the secure electrical contact could be assured after being exposed to the severe launch vibration loads because of the 1.7 mm full stroke of the spring-loaded pin of pogo pins.

| (a) | (b) |
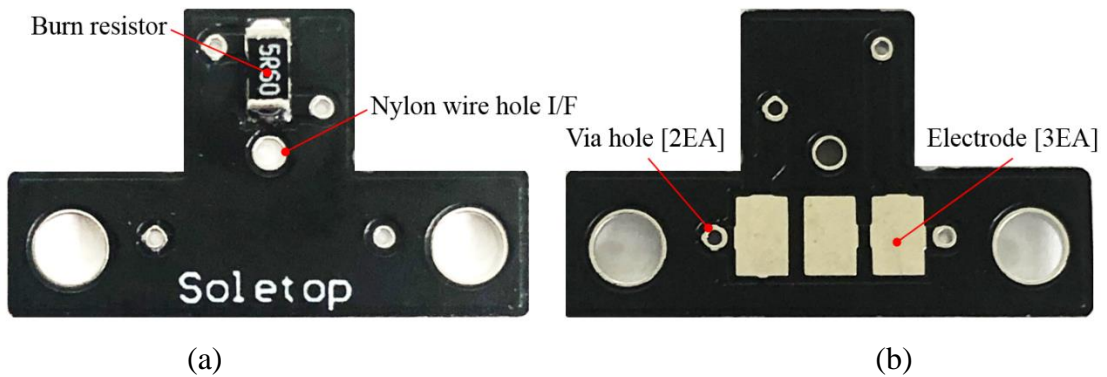
Fig. 24 Mechanical Configuration of Burn Resistor PCB: (a) Front View and (b) Rear View.

In this study, three pogo pins with the combination of voltage resistor divider are used to utilize the function of pogo pins as a deployment status switch that provides telemetry of "1" or "0" through buffer IC according to current flow status on the burn resistor, where "1" represents the output voltage at voltage resistor divider. Table 12 shows the truth table of the circuit to determine the deployment status of the solar panel. When the mechanism is triggered by the power supply in the circuit, the current flow through the burn resistor and voltage resistor divider, the resistance value of the resistors were selected in such a way that the output voltage at the voltage divider becomes approximately 0 V until the panel is deployed (the resistance value of the resistors used in the voltage divider is excessively higher than the burn resistor). The resistance of the resistors of the voltage divider and burn resistor was 10 kΩ and 4.7 Ω, respectively. Once the solar panel is deployed the circuit through the burn resistor becomes open thus output signal turns high (same as the output voltage at voltage resistor divider) that helps to determine the solar panel deployment status. The electrical interface PCB was

compact; it measured 34 mm × 16 mm and was integrated on the CubeSat structure, back of the CubeSat structure side bracket through bolt fastening. This makes it possible to implement the function of power, switch, and mechanical interface for pogo pins integration into the mechanism. Furthermore, the pogo pins and electrical components were mounted on the top side of the PCB, the same side that reduced the space needed to incorporate PCBs into the lateral edge of CubeSat structure compared to while integrating them in an alternative direction. The electrical components are also reduced such as XOR gate and one buffer IC compared to the electrical system proposed in two pogo pin based mechanism that minimizes the components radiation test efforts and cost of the HRM. Hence, the three pogo pin-based mechanism proposed in this study is simple, inexpensive, and compatible with the P-POD rail that does not interfere with the *z*-axis space of the CubeSat structure.

Table 12 Circuit Truth Table for Deployment Status of Solar Panel.

Input		Solar Panel Deployment Status			
		Undeployed		Deployed	
V_{in}	Enable	Pogo Pin Voltage	Output Voltage	Pogo pin Voltage	Output Voltage
1	1	1	0	1	1
1	0	0	0	0	0

3. Nylon Wire Tightening

Figure 25 demonstrates a nylon wire tightening process along the guide rail interface of brackets for mechanical constraints at the panel's out-of-plane direction. In order to avoid the interface with the P-POD, the bracket configuration and wire tightening method are proposed by the space-saving way on the lateral side of the CubeSat structure. The nylon wire (YGK Nylon) [75] made of fluorocarbon material of dimension 0.205

mm is winded around the guide rail interface of brackets that has a maximum allowable strength of 88.2 N. Thus, the nylon wire has an adequate strength to stow panel during the launch environment and also has space heritage [58]. The loading capability can be increased by increasing the number of wire windings. The surgeon's knot is carried out for the final knotting of wire at the bracket corner, which helps to create steady tight tension on the knot of tightened wire. The surgeon's knot is a surgical knot and is a simple modification to the reef knot. It adds an extra twist when tying the first throw, forming a double overhand knot. The additional turn provides more friction and can reduce loosening while the second half of the knot is tied. For the reliable release of the panel, the physical contact of the wire to the burn resistor is mandatory. Thus, the nylon wire guide rail interface notching on the brackets prevents wire misalignment from the burn resistors during the launch vibration period. Moreover, the edge fillet on the four corners of the brackets distributes the corner stress of the tightened wire, which is one of the important mechanical instigations for the structural safety of the tightened nylon wire. The effectiveness of the wire tightening method was validated through solar panel release function tests, addressed in more detail in the experimental validation chapter.
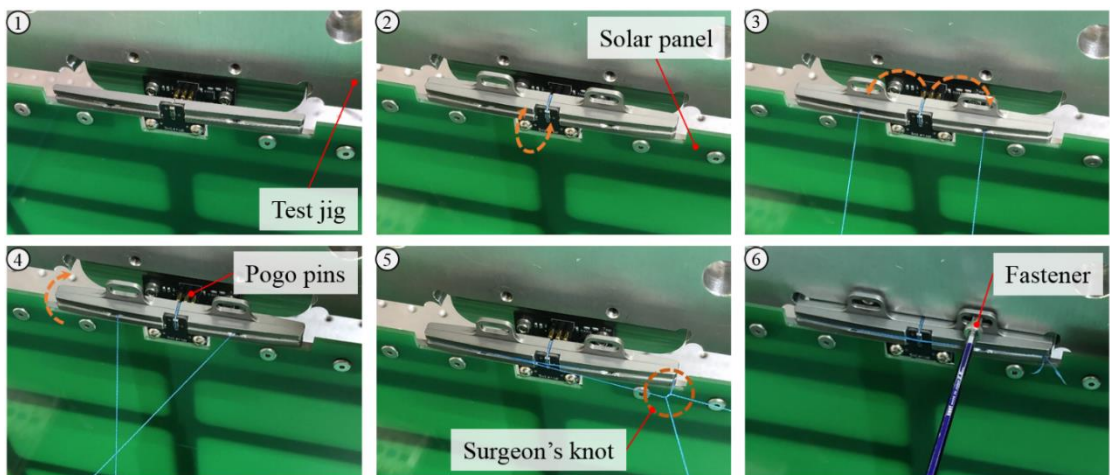
Fig. 25 Nylon Wire Tightening Process for Holding Constraint at the Panel.

Furthermore, Park et al. [57] investigated the normalized natural frequency of the solar panel module as a function of qualification temperature ranges -40 ℃ to 60 ℃. The solar panel was stowed with nylon wire tightening by performing a surgeon's knot. The results indicated that the frequency of the mechanism with respect to the temperature variation was negligibly low under the temperature ranges from -40 ℃ to 60 ℃. In addition, the test report [58] of the nylon wire stated that the elongation at the break of the wire only decreases to 67.9% of the original value when it is exposed to the ultraviolet (UV) radiation expected in the space environment for 200 hrs. This indicates that the nylon wire has sufficient endurance against the UV environment taking into account that the deployment of the solar panel is typically initiated after several minutes to hours after the orbital injection of the CubeSat.

The wire tightening method provides increased tension on the holding constraint as the nylon wire is tightened around the rectangular brackets with fillet edges as well as reliable cutting of the nylon wire upon activation of the mechanism. Additionally, the combination of vertical and horizontal cross-pattern winding of the wire with two additional hole interfaces in the brackets makes the secure holding constraints on the panel. Thus, the handling of the nylon wire during the wire tightening process becomes considerably simpler and reliable compared to the conventional mechanisms in which the nylon wire is tightened on the flat surface of the solar panel.

C. Deployment Mechanism

The passive and active deployment mechanisms have been used to deploy the deployable appendages of the satellite [76]. The active mechanism such as electrical motors and deployable booms requires power sources to turn on mechanical elements generate the deployment motions and it is very difficult to implement active mechanisms in the CubeSat due to the restraint space available in the edge of the P-POD. Thus the passive techniques, mechanical springs such as coil spring, torsional spring, tape spring have been commonly used in the CubeSat owing to simplicity and no electrical power requirement for deployment [77]. The CubeSat standard imposes strict restrictions on

satellite development, particularly of weight, size, and cost, which ought to be necessarily taken into account when designing solar panels and HRM. Additionally, despite the CubeSat standard, there are several norms and procedures that should satisfy the methodology as well as other restrictions when characterizing and designing the Solar panel module. For instance, NASA proposes a methodology of three phases to design a mechanism for satellites, which tends to obtain functional and low-cost designs, satisfying the most restrictive standards. According to NASA, successful deployment mechanisms of the deployable solar panel ought to have four states initial blocking, motion release, deployment guide, and final latching. Furthermore, the reduction of friction between the hinge shaft and the brackets is also an important factor to ensure the reliable deployment action on the panel. Additionally, the excessive mechanical backlash on the hinge shaft may generate excessive oscillations in the panel that could create unintentional stresses and fatigue on the solar panel and HRM under launch environments.

The deployment mechanism in CubeSat, similar to the holding mechanism, has many issues with the system which provides the anchor position for deployable solar panels [78]. The main issues of deployment mechanisms for solar panels in CubeSats are the inaccurate torque estimation, friction on the hinge shaft and brackets, lack of a position system to block the back-driving of the solar panel when it reaches the final phase of the deployment. Furthermore, the most typical approach to mitigate in-orbit rigid body motion disturbance on the deployed solar panel induced by attitude slewing maneuver is to increase the solar panel stiffness in deployment state by increasing the residual rotational stiffness of torsional hinges. The passive latching mechanism locks the panel at the final deployment position such that oscillation could be reduced to some extent [79]. However, the latch shock force induced by the solar panel's deployment speed could be excessively increased owing to the increased hinge's initial torque. That could lead to a large transient impulsive force and momentum exerting on the satellite system, thus, threaten the structural safety on the bus system due to the transient shock, and may also affect the flight trajectory or attitude of the satellite at an initial orbital

ejection period [80-82]. Additionally, the conventional technologies for reducing back driving and panel oscillation that has been widely applied for large-class satellites, such as rotary damper or deployable truss link, are extremely difficult to apply them for CubeSats due to the spatial limitations allowed for the deployable appendages. These facts indicate that accurate estimation of the torque budget of the torsional hinge might be necessary for the reliable release action and latch the panel in an intended position.

1. Torque Budget

The torque budget and mechanical tolerance gap between the hinge brackets and shaft were estimated based on the ECSS standard. The torque budget of the torsional spring based on the solar panel mass and residual torque after deployment for the passive latching is derived by the ECSS torque budget formula [83].

$$T_R = 2(3T_{friction} + 1.1T_{1g}) \tag{3.1}$$

Where T_R is the minimum required torque to deploy the solar panel. The $T_{friction} = M \times r \times \mu$ and $T_{1g} = M \times r$ are the frictional and 1g torque, respectively. The M, r, and μ are solar panel mass, spring radius (mandrel radius) or shaft radius, and frictional coefficient of aluminum material, respectively. The calculated torque budget of the solar panel is summarized in Table 13. The minimum torque required to deploy the solar panel is 88.81 N-mm.

Table 13 Torque Budget of the Solar Panel Torsional Hinge.

Parameter	Value
Solar Panel Mass (g)	285
Shaft Radius (mm)	1.5
Frictional Coefficient of Aluminum	1.4
$T_{friction}$ (N-mm)	2.74
T_{1g} (N-mm)	1.96
T_R (N-mm)	88.81

2. Torsional Hinge

Figures 26 (a) and (b) show the stowed and deployed configuration of the passive torsional spring-based deployment mechanism, respectively. The passive torsional springs of the hinges produce torque to deploy the solar panel in the final intended position of 90 degrees relative to the initially stowed configuration. The hinge is mainly composed of brackets, torsional spring, hinge shaft, C-clamp, and delrin bushing. The CubeSat side hinge bracket mounted on the structure has extended space on the lateral side for the end stop of the solar panel. The passive latching of the panel is achieved by the combination of residual force of the torsional spring and the end stop at the deployment position of the solar panel. Delrin bushings are used to minimize the mechanical friction between fixed and moving brackets that could help to ensure reliable deployment after being exposed in the launch environments. In order to lock the hinge shaft, the C-clamp is proposed because of its lightweight, compact volume and frictionless locking in the arterial side of the shaft. The hinge brackets, shafts, and torsional hinge are made up of Aluminium 6061 that have commonly preferred for the mechanical parts of the CubeSat. The 90-degree actuation of the solar panel in a

deployed configuration is determined by the power balance orbital analysis of the CubeSat based on the optimal orientation of the deployable solar panels towards the Sun direction during its orbital periods. Furthermore, in order to reduce unusual backlash on the hinge shaft in the radial direction of the hinge rotational axis, the mechanical tolerance gap between the hinge brackets and shaft, delrin washers were made 0.05 mm.
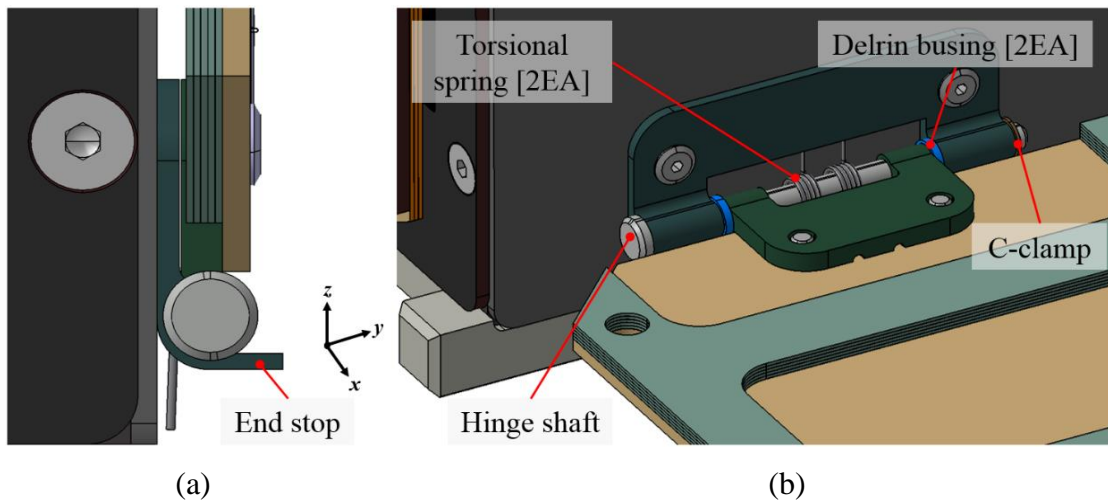
Fig. 26 Conceptual Mechanical Design of Torsional Hinge: (a) Stowed and (b) Deployed.

Based on this torque budget calculation result, a 180-degree arm angle torsional spring of spring constant 0.1533 N-mm/deg. is selected that could produce a torque of 27.6 N-mm at panel stowed position. The specifications for the selected torsional spring are specified in Table 14. In the stowed configuration of the panel, the four torsional springs of two hinges will induce 110.37 N-mm that satisfies the necessary torque of 88.81 N-mm for panel deployment with the margin of 21.56 N-mm. Furthermore, the torques induced by the springs are compatible and far less than the holding restraint imposed by the wire winding around the HRM brackets, which ensures that the hinges do not result in excessive preload on the nylon wire knot. The torsional spring chosen in the design has an arm angle of 180 degree, thus at the 90 degree deployment from the

initial stowed position of the panel, the torque spring could ensure half of the initial torque as a residual torque that latches the panel in the deployed state. The deployment action of the mechanism was evaluated by repetitive deployment tests of the solar panel in ambient room temperature of 20 ºC, the detailed description of the functional test results is presented in the experimental validation section of this dissertation.

Table 14 Specifications of Selected Torsional Spring [84].

Spring Diameter (mm)	Number of Winding	Wire Diameter (mm)	Arm Length L/R (mm)	Arm Angle (deg.)	Spring Constant (N-mm/deg.)	Max. Torque (N-mm)
3	5	0.2	20	180	0.1533	27.6

IV. Structural Safety Analysis and Thermal Design Evaluation

A. Launch Vehicle Environment

Before a CubeSat can become operational it must first make the journey to its mission orbit through the launch vehicle. The launch loads environments are made up of a combination of steady-state, low-frequency transient, higher-frequency vibroacoustic, and very high-frequency shock loads. Such excitations may be of aerodynamic origin (e.g. wind, gusts, or buffeting at transonic velocity) or due to the propulsions systems (e.g. longitudinal acceleration, thrust buildup, or tail-off transients, or structure-propulsion coupling, etc.) [85]. Surviving the launch without any damage to payloads or bus systems is essential for mission success. Table 15 demonstrations the sources of launch vehicle environments. Acoustic loads also know sound pressure is as a result of exhaust noises and turbulent flows along with the launch. However, vibration and shock are the primary forces that satellite encounters during launch. The particular events like ignition, engine shut-off, and separation of the payload, shock occurs they are major thrills that happen in a short span of time and die off quickly. For extended periods, vibrational forces are predominant during launch and have greater overall excitation energy than shock forces. These vibration loads will be described in detail in subsequent sections.

Table 15 Sources of Launch Vehicle Environments [85].

Stages	Acoustics	Random Vibration	Sine Vibration	Shock
Lift-off	✓	✓		
Aerodynamics/Buffet	✓	✓		
Separation (Stage, Fairing, Spacecraft)				✓
Motor Burn/Combustion/ POGO		✓	✓	

Every launch vehicle exhibits its own unique loading and vibrations during launch. As a result, each launch provider has its own specific requirements that a spacecraft must meet. In the ride-share environment, knowing the exact launch vehicle loads during development is not always guaranteed. Fortunately, NASA established the General Environmental Verification Standard (GEVS) providing general requirements encompassing the worst case load conditions of common launch vehicles [86]. Figure 27 shows an example of the GEVS launch loads for the worst-case scenario. The acceleration magnitude at the corresponding frequency is plotted for each launch vehicle (LV). The vibration profile dictated by GEVS exceeds the profile of the other four launch vehicles shown, providing a conservative estimation of vibrational loads that must be accounted for the satellite. Designing to GEVS will ensure that a spacecraft will meet the specific requirements of a variety of launch vehicles. This design strategy is essential for spacecraft utilizing ride-shares; increasing the probability the spacecraft can launch on the first available platform. The GEVS encompasses a range of environmental requirements a spacecraft must meet, including structural and mechanical verification.
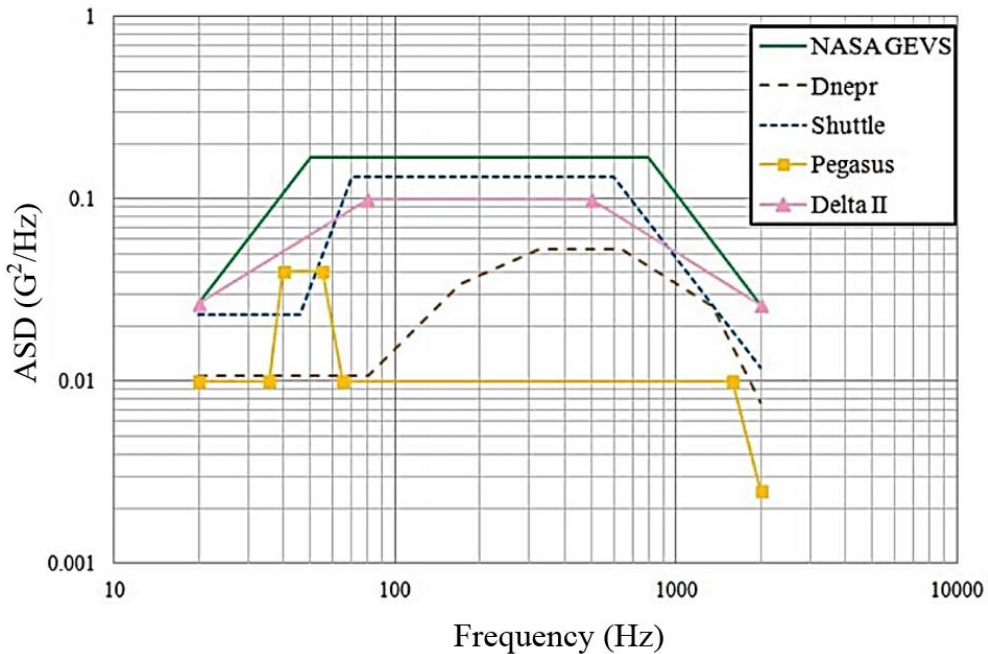
Fig. 27 NASA GEVS Vibration Profile with the other Launch System [86].

Despite the fact that currently available launch vehicles have provided a relatively high success rate, there is no guarantee that failure will not occur. To reduce the risk of failure, stringent qualification testing of the secondary payloads are requested by launch providers to minimize the risk of failure and to ensure the added payload will not adversely impact the launch. Additionally, it is equally important for ensuring the structural safety of mechanical sub-systems and payloads.

B. Launch Vibration Load

1. Low Frequency Sinusoidal Vibration

The low-frequency sinusoidal vibrations occur as a result of the interaction between launch vehicle mode forms and loads occurring during lift-off, combustion of the engines, and POGO phenomenon at engines burn up of a stage. The POGO is a self-excited longitudinal vibration that is generated through the closed-loop interaction of the launch vehicle structure and propulsion system with combustion chamber pressure and thrust fluctuations [87]. Table 16 shows the qualification-level sinusoidal vibration test profile of the QB 50 system requirements and recommendations for the small satellites. Often referred to as the sinusoidal vibration, this load is typically expressed in terms of acceleration amplitude in *g* over the frequency range of interest, which is usually under 100 Hz.

Table 16 Qualification-level Sinusoidal Launch Vibration Test Specifications [88].

Level	Frequency (Hz)	Amplitude (g)	Sweep Rate (oct/min)
0 dB (Full Level)	5	1.3	2
	8	2.5	
	100	2.5	

2. Random Vibration

Random vibration in the launch environment is primarily induced through the structural transmission of acoustic pressures impinging on the surfaces of the vehicle. Other less significant sources include structure-borne vibration transmitted directly from rockets motors and other equipment. Random vibration is no-deterministic, meaning its instantaneous magnitude is predictable only on a probability basis [89]. Such vibration may be considered as being composed of a continuous spectrum of frequencies whose individual amplitudes are varying in a random manner. The random vibration is usually quantified in terms of Power Spectral Density (PSD) in g^2/Hz. The mechanical dynamic loads during random vibration are in a frequency range of 20-2000 Hz. The amplitude is described statistically by determining the percentage of time the vibration is within certain limits. The root mean square (RMS) acceleration (G_{rms}) value is typically used to express the overall energy of a particular random vibration event and its statistical value is used for structural design and analysis purposes. The GEVS qualification level random vibration test specification for a satellite less than 22.7 kg is presented in Table 17.

Table 17 Qualification-level Random Vibration Test Specifications [86].

Level	Frequency (Hz)	Amplitude (g^2/Hz)	Test Duration (s)	RMS Acceleration (G_{rms})
0 dB (Full Level)	20	0.026	120	14.10
	50	0.16		
	800	0.16		
	2000	0.026		

C. Structural Analysis

The structural analysis of the solar panel module proposed in this study is performed by the Patron and Nastran commercial software through finite element analysis (FEA). To predict the 1st eigenfrequency and mode shapes of the solar panel modal analysis are performed. The static and dynamic response of the solar panel under the launch vibration loads was investigated by random and random equivalent static analysis. The GEVS qualification-level test loads are applied for the random vibration analysis of the solar panel. Then, the margin of safety on the holding constraint of the panel is estimated using a random equivalent static analysis result.

In general, it is essential to design the satellite payloads with a first fundamental frequency greater than 35 Hz, but, GEVS exceeds this value, recommending coupled loads analyses between satellite and booster for modes below 70 Hz [90]. According to the specifications of Ariane-5, the structure of the satellite is requested to have a minimum of 50 Hz fundamental lateral frequency and a minimum of 100 Hz basic longitudinal frequency [91]. In this study, the more conservative value of 60 Hz will be the assumed threshold for the first fundamental frequency of the solar panel, the same as the typical requirement for secondary payloads.

1. Finite Element Modelling

The FEA is the simulation of a physical phenomenon using a numerical mathematic technique referred to as the finite element method (FEM). This process is at the core of mechanical engineering, as well as a variety of other disciplines. Barsoum et al. [92] investigated the static and dynamic performance of the CubeSat primary structure using finite element software. Moreira et al. [93] studied finite element modeling and computational method of damping structures. Abdoun et al. [94] examined the responses of multilayer constrained damping structures through FEM. Yang et al. [95] considered strain energy and damping characteristics of the five-layer structure by finite element modelling while Li et al. [96] conducted experimentations on its damping property for comparison of results. It is difficult to estimate an accurate numerical modeling

representation for the mechanical performance of viscoelastic damping materials because the complication of the physical structure leads to the non-linear material's characteristics. Not only the system with viscoelastic material most of the structural systems show a certain extent of nonlinearity associated with different sources [97,98]. However, neglecting the nonlinearity is acceptable in many cases for the sake of simplification of analysis [99,100]. In other cases, nonlinear behavior plays a dominant role. Nonlinearity abandoning should be prevented in such cases, as it may lead to erroneous predictions of system behaviors [101]. Though, the vibration attenuation of constrained layer damping with viscoelastic materials is highly dependent on geometric parameters of viscoelastic and constraining layers. Thus, we have considered simpler FEM modeling by varying the material properties as the thickness of the viscoelastic adhesive layer is only 0.06 mm. Predominantly, the simulation dynamic analysis results are related to the damping value of the system. Therefore, the modal damping value obtained from experimental free-vibration test performed prior to simulation analysis is used for more accuracy of the results. Torisaka and Yamakawa [102] applied structural damping value of the solar panel employing constraint viscoelastic material obtained from an experimental characteristics investigation test for numerical analysis. It is simple and more time-effective as its validity and accuracy have been proved through comparison to other methods.

Figure 28 shows the FEM model of the solar panel module. The CHEXA, CTETRA10, RBE2, RBE3, and CBAR elements were built for the modeling of the solar panel module. The total number of nodes and elements were 180466 and 117806, respectively. The PCB panel stiffeners and tapes were modeled by CHEXA elements, although the hinge and HRM were modeled by making the CTETRA10 element. As the company does not disclose the detailed material properties of the adhesive used in the $3M^{TM}$ transfer tape, the tape is assumed to be 0.06 mm thick polyimide.
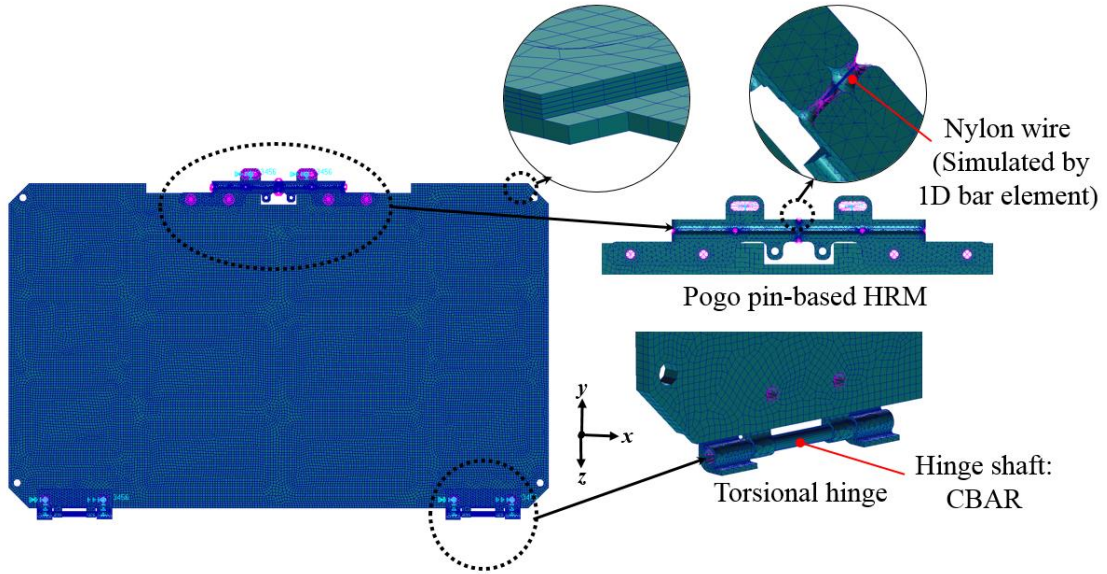
Fig. 28 Finite Element Model of the Solar Panel Module.

The boundary conditions were imposed according to the solar panel mounting on the CubeSat structure in stowed configuration. The nylon wire was executed by making RBE2 and 1D bar element (CBAR) with applying material property of the nylon. At the corners of the brackets, we have made RBE2 multi-point constraints (single node connected to many nodes), where the center single node is independent and the other side nodes are dependent. The degrees of freedom of the single-core node enforces the degrees of freedom of the leg nodes thus it distributes the force and moment equally among all the connected nodes (corners of the HRM brackets) irrespective of the position of force or momentum. The center independent nodes of two opposite RBE2 of the brackets are connected by making a CBAR element, where material properties of the bar element are applied as nylon to simulate wire tightening more accurately. The CBAR element is a kind of simplified CBEAM element that has been used whenever the cross-section of the structure and its properties are constant and symmetrical. Thus, RBE2 and CBAR elements add stiffness between HRM brackets by constraining the system to follow a one-to-one linear displacement and/or rotational relationship between the connected nodes. It enables the solar panel module to conduct torsional as well as

translational dynamic behaviors that perform more precise simulations for wire tightening.

The hinge shaft was modeled by making the RBE3 and CBAR elements. The central dependent node of RBE3 is (Ux=Uy=Uz=Ry=Rz=0) degrees of freedom that allows the rotational motion only in the x-axis and the independents nodes are in (Ux=Uy=Uz=0) degree of freedom. The motion at the dependent node of RBE3 is a weighted average of the motion at the independent nodes and it does not add artificial stiffness to the structure. All the bolding interfaces for the HRM brackets and hinges were constrained by the RBE2 with the 6-degree of freedom constraint. Table 18 summarizes the information of the solar panel finite element model. Table 19 presents the material properties of the solar panel module applied for the structural analysis.

Table 18 Information of Solar Panel Finite Element Model.

Item			Number of Node or Element
Node			180466
Element	Solid	CHEXA	65946
		CTETRA10	51824
	Shell	RBE2	22
		RBE3	8
		CBAR	6

Table 19 Material Properties of the Solar Panel used for Structural Analysis.

Item	Material	Young's Modulus (GPa)	Poisson's Ratio	Density (kg/m^3)
Solar Panel and Stiffener	FR4	18.73	0.136	1850
HRM and Hinge	Al6061-T651	69	0.33	2700
Adhesive Tape	Polyimide	2.5	0.34	1430
Nylon Wire	Nylon	2.7	0.38	1130

2. Modal Analysis

The first step during a dynamic analysis is the determination of natural frequencies (eigenfrequencies) and mode shapes of the solar panel. The results of this analysis characterize the dynamic behavior of the structure and can show how the structure will respond under dynamic loads [103]. The most important modal characteristic of a structure is the natural frequency threshold, the first natural frequency must be above a specific value, which is usually determined by the launch vehicle. The general system requirement of the deployable solar panel of 6U CubeSat is the eigenfrequency of the panel must meet at least 60-90 Hz. To predict the 1st eigenfrequency and mode shapes of the solar panel proposed in this study modal analysis are performed by making the finite element as shown in Fig. 28. In order to compare the effectiveness of the proposed solar panel, the modal analysis of typical solar panels without using an additional stiffener is also carried out. The FEM modelling of the panel is made in the same fashion as the solar panel as described in the finite element modelling section. The total number of nodes and elements of the simulated typical solar panel were 145158 and 79746, respectively.

Figure 29 shows the first four mode shapes of a typical solar panel module of the same PCB size without employing the additional stiffeners. The first four fundamental modes of the solar panel were appeared at 52.69 Hz, 58.98 Hz, 76.92 Hz, and 134.04

Hz, respectively. As expected the first mode of the solar panel appears torsion mode shape because of the application of a single HRM constraint in the center of the edge.

Mode 1 (52.69 Hz)   Mode 2 (58.98 Hz)

Mode 3 (76.92 Hz)   Mode 4 (134.04 Hz)
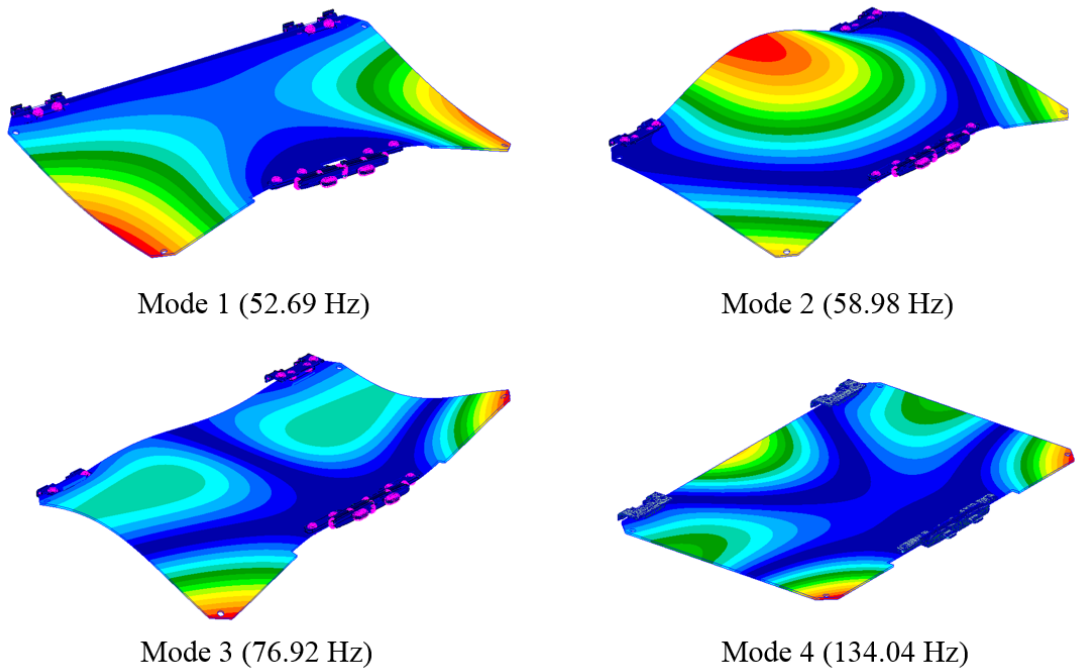
Fig. 29 Mode Shape of the Typical Solar Panel Module without Employing
Additional Stiffeners.

Figure 30 shows the first four mode shapes of the proposed solar panel module. The first four fundamental modes of the solar panel were appeared at 83.83 Hz, 119.28 Hz, 233.82 Hz, and 253.18 Hz, respectively. The result indicates that attachment of thin multi-layered stiffeners on the panel by viscoelastic acrylic tape also increases the stiffness of the solar panel. Moreover, the global bending mode is obvious for the solar panel assembly shown in this study, even if the stiffeners proposed in this study are installed on the solar panel. This is because the stiffness value of the stiffeners themselves is smaller than the panel, such that they do not change the original mode shape at 1st eigenfrequency of the panel although the modes at higher frequency might be changed to some extent. In addition, many of the previous literature [104, 105] also

proven that the global bending mode was observed from the similar configuration of the stiffened panel assemblies. These facts indicate that the fundamental mode shape of the solar panel at 1st eigenfrequency is not changed by the attached stiffener proposed in this study although the dynamic displacement would be reduced owing to the increased stiffness of panel assembly.

Mode 1 (83.83 Hz) Mode 2 (119.28 Hz)

Mode 3 (233.82 Hz) Mode 4 (253.18 Hz)
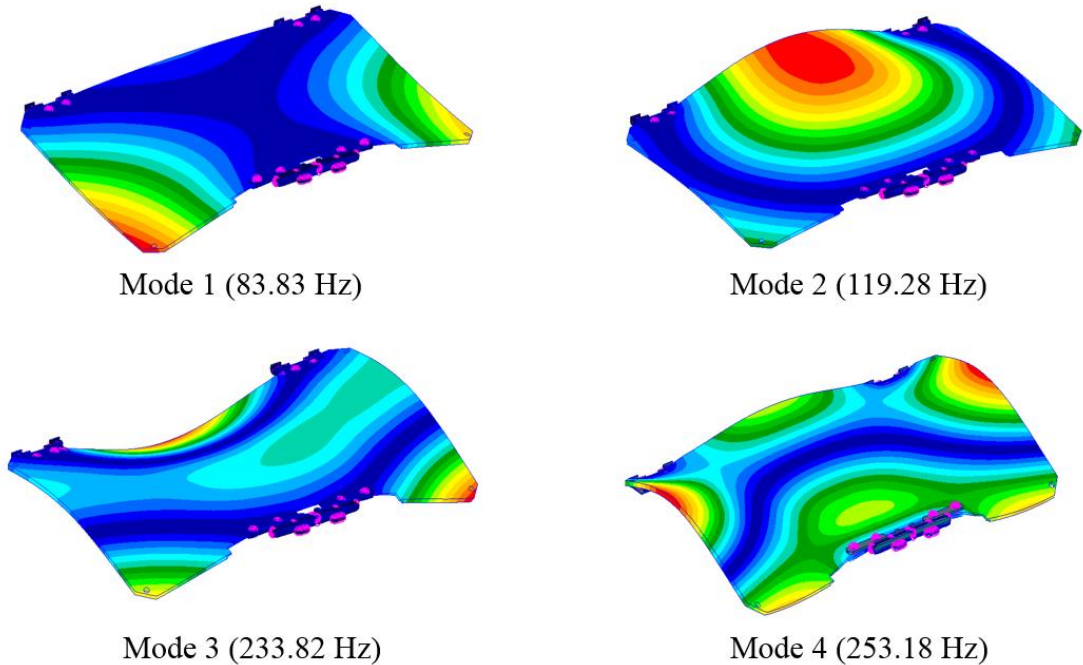
Fig. 30 Mode Shape of the Proposed Solar Panel Module.

Figure 31 demonstrates the VMLSA panel's stiffness according to the stiffeners attachments conditions, which was obtained from the simulation results. This curve line implies that increasing the number of stiffeners raised the panel rigidity to some extent, however, not as a linear function of stiffener numbers. The zone of saturation started from the panel with 5 layers of stiffeners, the same numbers of stiffeners were implemented in the design evaluation of the VMLSA by considering the available solar panel accommodation area in the P-POD.
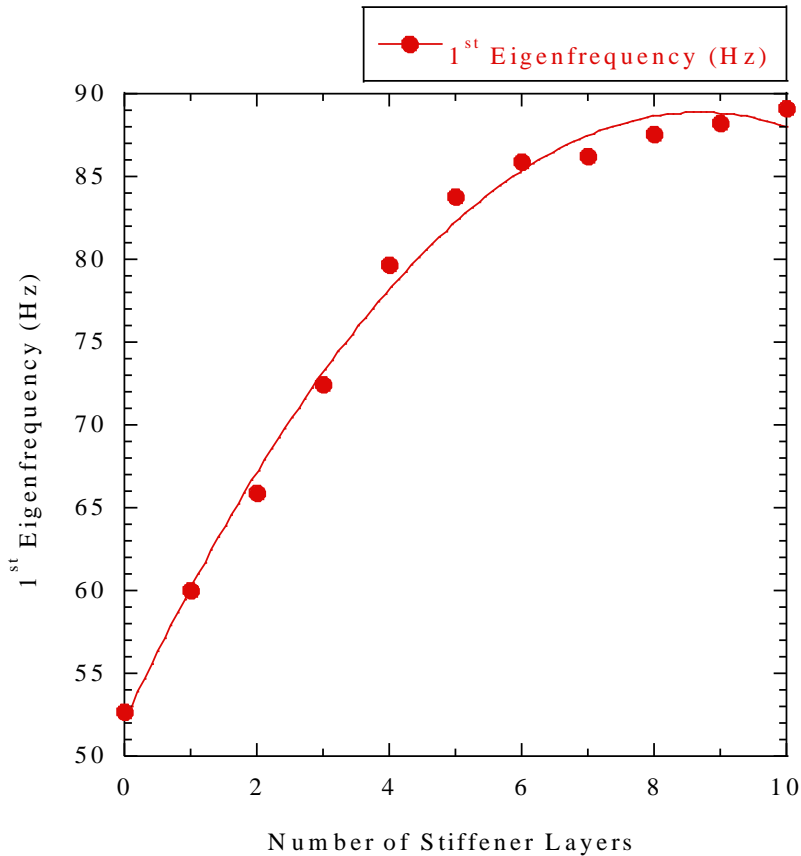
Fig. 31 Relationship of Stiffness of VMLSA According to the Number of Attached
Stiffener Layers.

3. Random Vibration Analysis

To perform the random vibration test, a random test spectrum must be defined. Figure 32 shows simulation analysis result of random vibration power spectral density (PSD) response of the solar panel under the GEVS qualification level random vibration load listed in Table 17. The modal damping values of 0.036 and 0.141 were applied in the analyses of the typical FR4 panel and VMLSA, respectively. These damping values were obtained from the free-vibration test results. Prior to performing the dynamic analysis, we had carried out free-vibration tests at ambient room temperature of 25 ℃. A more detailed explanation was presented in the basic dynamic characteristic section of the experimental results. Generally, the random vibration spectrum profile is

exhibited as a PSD acceleration vs. frequency plot. The PSD plot shows mean square acceleration per unit bandwidth (i.e. acceleration squared per Hz versus frequency) thus the shape of the PSD plot defines the average acceleration of the random signal at any frequency. The G_{rms} value obtained from acceleration power spectral density (APSD) profiles of the proposed solar panel was 12.20. The output response of the solar panel in the z-axis is lower by a factor of 1.15 than that of the input 14.1 G_{rms} level. The mode frequencies for the 1st and 2nd modes are clearly visualized in the power spectral density response graph of the solar panel obtained from random vibration analysis. However, the higher modes such as 3rd and 4th modes are not clearly identified because the graph is drawn on a logarithmic scale and the amplitude on these frequencies might be lower in the excitation axis.
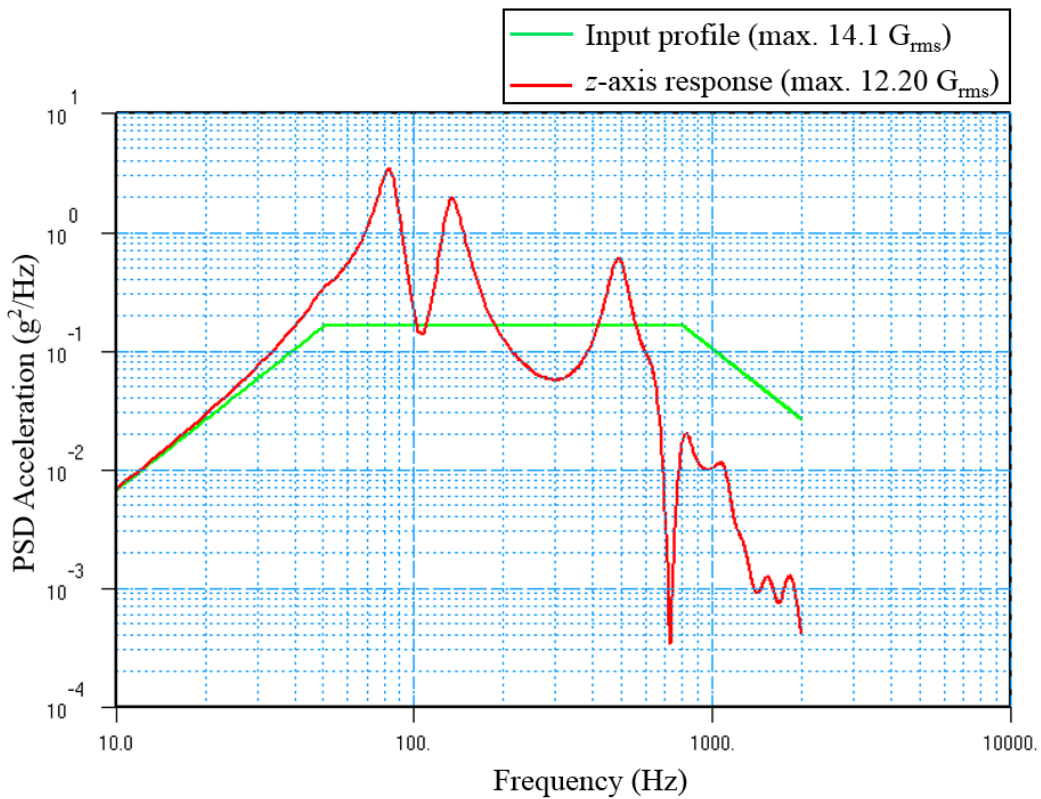
Fig. 32 Power Spectral Density Response of the Solar Panel under Random Vibration Load obtained from Simulation Result.

Figure 33 shows the relative dynamic displacement at the center of the solar panel obtained from random vibration analysis. The maximum dynamic deflection of the vibration shaker table and the solar panel is 0.58 mm and 0.72 mm, respectively. The maximum relative dynamic displacement at the center of the solar panel along the excitation axis (z-axis) estimated from the random vibration simulation analysis is 0.14 mm.
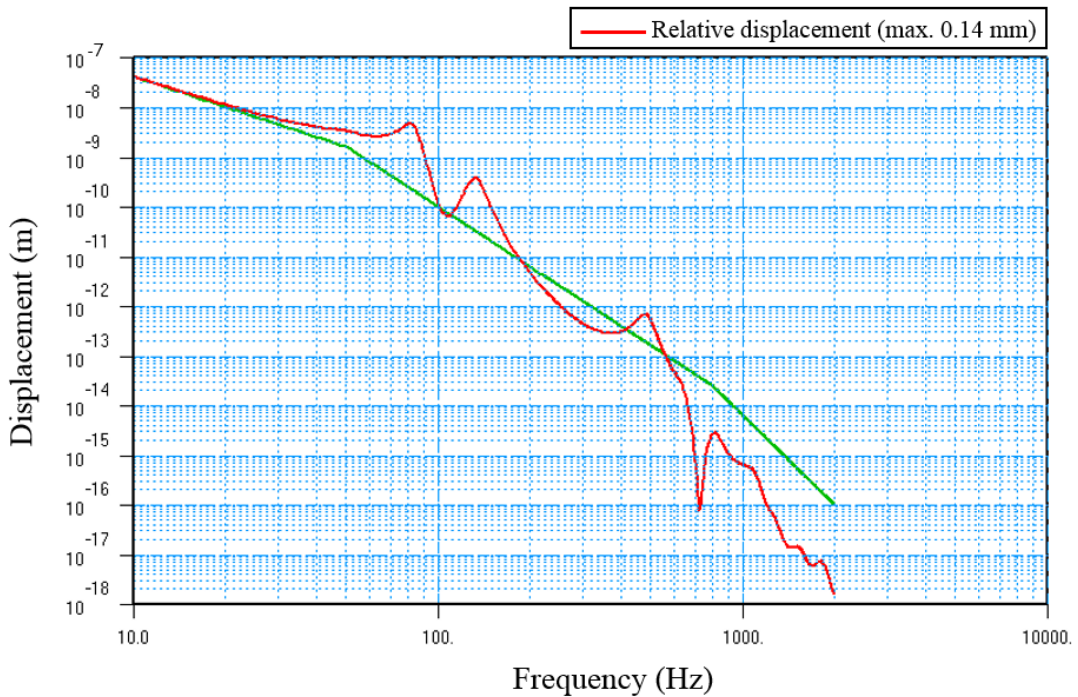
Fig. 33 Relative Dynamic Displacement at the Center of the Solar Panel under Random Vibration Load obtained from Simulation Result.

Table 20 summarizes the dynamic analysis results of the typical solar panel without employing additional stiffeners and proposed solar panels with the application of viscoelastic multi-layer stiffeners. The results show that the 1st eigenfrequency of solar panel module with stiffener is higher by a factor of 1.59 than that obtained in the solar panel without stiffeners although the mass difference between them is minimal. Moreover, the PSD acceleration response of the proposed panel is lower by a factor of

1.96 than that of the typical FR4 solar panel this is because of the higher damping capability achieved by multi-layered stiffeners interlaminated with viscoelastic tapes. Furthermore, the max. relative displacement of the solar panel is also reduced owing to resistive deformation characteristics of the panel. Furthermore, to investigate the influence of the HRM and hinge modeling on the analytical result of the solar panel, additional tests of the solar panel without HRM and hinge was performed with constraining by RBE2 at the HRM and hinge hole interfaces of the panel. The results indicate that the first eigenfrequency of the panel in a rigidly mounted condition is 111.5 Hz, which is 27.67 Hz higher than that of the module level. However, the acceleration PSD is slightly higher than the solar VMLSA in module case. These results indicate that the dynamic response of the panel could be influenced by the hinge and HRM modeling due to the difference in boundary conditions.

Table 20 Summary of Solar Panel Dynamic Analysis Result.

Case	Solar Panel	Eigenfrequency (Hz)		Acceleration Power Spectral Density (G_{rms})	Max. Relative Displacement (mm)
Module Level	Typical FR4 Solar Panel	Mode 1	52.69	23.97	0.78
		Mode 2	58.98		
		Mode 3	76.92		
		Mode 4	134.04		
	VMLSA	Mode 1	83.83	12.20	0.14
		Mode 2	119.28		
		Mode 3	233.82		
		Mode 4	253.18		
Rigidly Mounted	VMLSA (without HRM and Hinge)	Mode 1	111.50	13.90	0.12
		Mode 2	111.78		
		Mode 3	133.62		
		Mode 4	255.01		

4. Random Equivalent Static Analysis

The satellite will be exposed to simultaneous static and dynamic loads during the launch phase due to launch acceleration and aerodynamics. Thus, the solar panel should be designed and tested to withstand all these loads. From design perspective, a common approach is to combine static and dynamic loads into an equivalent static load which is referred to as quasi-static loads [106]. In the solar panel context, the quasi-static loads are random equivalent static loads, typically expresses as equivalent accelerations at the center of gravity. The maximum amplitude of these loads is generally encountered at the end of the first-stage burn of the launch vehicle because of the weaker mass of the launcher (the burned fuel mass being no longer present) for the same amount of thrust [107]. In order to obtain the maximum force and stress distribution on the panel especially in the bolting interfaces and panel holding constraint nodes at the vibration loads, the random equivalent static analysis is performed by applying panel inertial load. The inertial load of the solar panel is calculated from Miles' equation [108].

$$X_{max} = 3\sqrt{\frac{\pi}{2} f_n \sqrt{f_n} \ U_{PSD}(f_n)} \tag{4.1}$$

Where X_{max} is the inertial load, f_n is the natural frequency, and $U_{PSD}(f_n)$ is the input power spectral density at f_n. If the modal analysis has been performed and determined a predominant resonance frequency, the Miles' equation can be used to estimate the inertial loads due to the random vibration as it provides a statistical calculation of the peak load for a single degree of freedom (SDOF) system. The inertial load on the panel during the random vibration is approximately 58.92 g, which is calculated from the Miles' equation. In the analysis, Von Mises stress and multi point constraint (MPC) force on the nylon wire were calculated to identify the force on the nylon wire knot for predicting the structural safety of the wire under launch loads that also helped to determine the number of required wire winding for holding constraint on the panel. The result shows that the maximum force on the nylon wire knot's is 21 N during the *z*-axis

excitation that is the most severe axis for the static loads due to the excessive dynamic deflection as compared to the other axes.

5. Margin of Safety of Nylon Wire

The approximation of margin of safety (MoS) of the nylon wire knot that holds the panel during the launch is one of the important aspects for ensuring the structural safety of the solar panel under launch loads. The MoS at the holding constraint of the panel is calculated through the following equation.

$$MoS = \frac{F_{allowable}}{S.F \times F_{max}} - 1 \geq 0 \qquad (4.2)$$

Where $F_{alllowable}$ and F_{max} are the maximum allowable strength force of the nylon wire and maximum force on the nylon wire knot node obtained from the random equivalent static analysis, respectively. The $S.F$ is a safety factor which is the standard value of 3 for the structural mechanics of the satellite [109]. The MoS of the nylon wire for holding constraint on the panel is estimated according to the number of nylon wire winding on the HRM brackets under the assumption that the allowable force of the wire will be multiple with increasing the number of wire winding. Table 21 presents the estimation of nylon wire margin of safety according to the random equivalent static analysis result. The single winding of the nylon wire can withstand a maximum of 88.2 N of load, however, the calculated result shows the maximum allowable strength of the nylon wire on the HRM bracket should be 176.4 N or greater for a positive margin with the safety factor of 3. The results showed that at least double nylon wire winding is required to hold the panel securely for ensuring the structural safety of the solar panel under launch vibration loads.

Table 21 Estimation of Margin of Safety of the Nylon Wire on VMLSA.

Material	Number of Winding	Wire Diameter (mm)	$F_{allowable}$ Force (N)	Inertial Load (g)	F_{max} (N)	S.F	MoS
Nylon	1	0.2	88.2	58.92	21	3	0.4
	2		176.4				1.8
	3		264.6				3.2

In addition, dynamic response of FR4 panel employing Al-stiffeners of the same stiffness with the VMLSA panel has been investigated through the simulation analysis to compared the effectiveness of constrained layer damping strategies implemented in the VMLSA for reduction of the burden on nylon wire under vibration loads. Table 22 lists the dynamic responses of the VMLSA and FR4 panel employing Al-Stiffener. Even though the stiffness of the panels are the same, the dynamic responses of VMLSA such as G_{rms} value and relative displacement are substantially reduced owing to the damping characteristic achieved between interlaminated viscoelastic layers and stiffeners. The MoS on the nylon wire with the double wire winding at a safety factor of 3 was 0.33 and 1.8 for FR4 panel with Al-stiffener and VMLSA. Additionally, the force on the nylon wire knot and MoS on the nylon wire knot of the typical FR4 panel was 27 N and 1.1, respectively.

Table 22 Comparison of Dynamic Responses of the VMLSA and FR4 Panel using Al-Stiffener of Same Stiffness.

Case	Mass (g)	Simulation Result				
		1st Eigenfreq. (Hz)	G_{rms}	Relative Disp. (mm)	Force on Nylon Wire (N)	Margin of Safety (MoS)
FR4 Panel with Al-Stiffener	324.6	83.88	29.97	0.49	44	0.33
VMLSA	306.5	83.83	12.20	0.14	21	1.8

The comparison of the solar panel's dynamic performance under launch environments is demonstrated in Fig. 34. The typical FR4 panel is also presented in the graphs. The results showed that the FR4 panel with Al-stiffener reduces the dynamic deflection to some extent as compared to the typical FR4 panel owing to the stiffness increased. However, the increased mass of the panel inevitably increases the panel excitation under a launch load owing to the increased acceleration; this may result in an undesirable burden on the HRM. However, the VMLSA panel has shown relatively excellent dynamic performance as compared to the other cases on the view of ensuring the structural safety of the panel under the launch environments owing to the constrained layer damping.

(a)   (b)

(c)   (d)
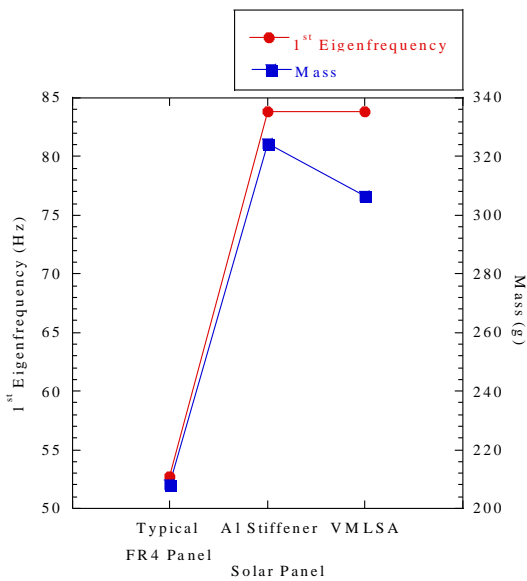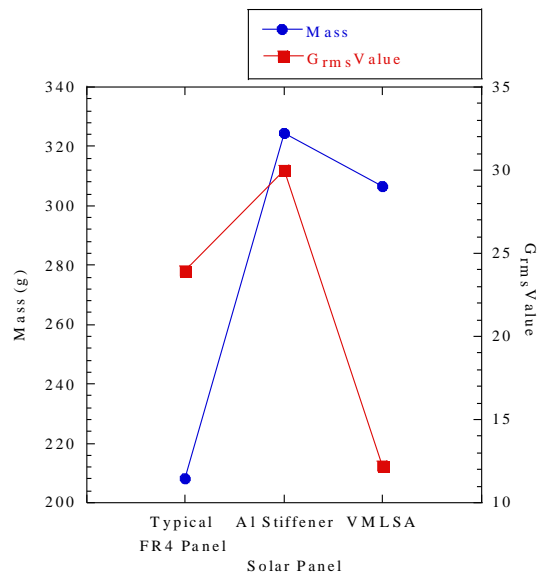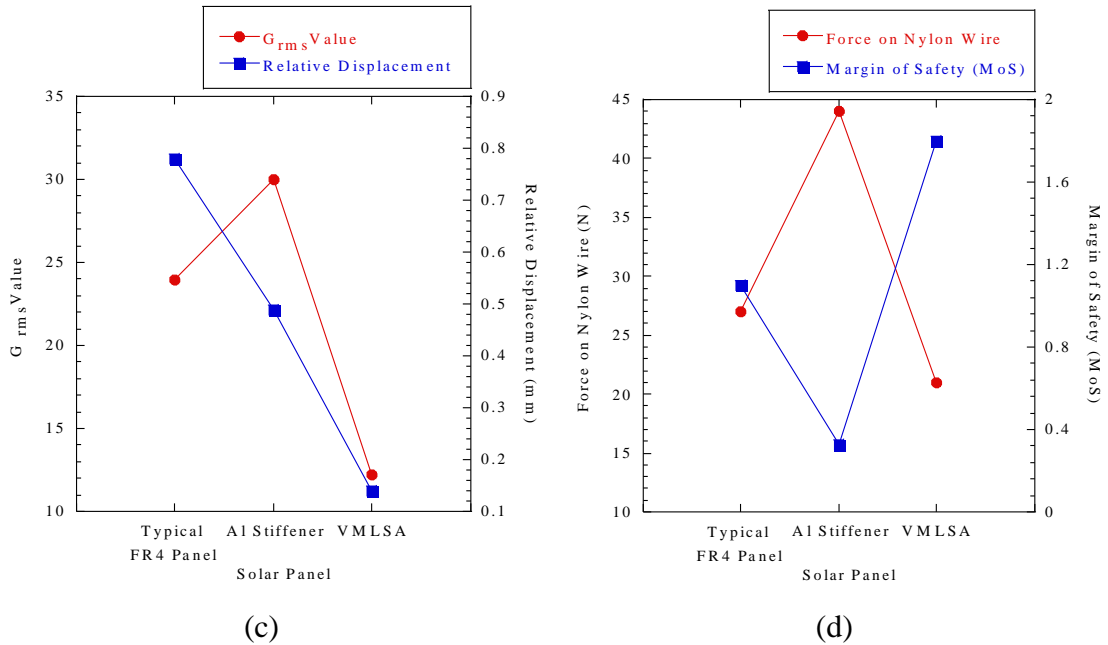
Fig. 34 Simulation Results of Dynamic Behavior of the Solar Panels under Launch
Loads.

D. Thermal Analysis

The performance of the power generation of solar panels can be estimated from its solar cell efficiency, however, the ratio of incident solar radiation to converted power varies total power generation during orbit. There are many other factors influencing solar cell efficiency, and the in-orbit temperature of a solar cell is critical and the nominal temperature can get better efficiency [110]. Since the temperature variation range of a low-earth orbit satellite solar array is usually very wide, nearly -80 ºC to 80 ºC, a severe thermal environment is unavoidable [111]. To ensure the safety of the solar cells and steady power generation from the deployable solar panel, an appropriate passive thermal design is important to minimize the thermal distortion of the solar panel in the severe in-orbit thermal environment of the satellite orbital periods [112]. The thermal design based on active thermal hardware that been used in the larger sized solar panel of big satellites were not investigated in this study owing to the system complexity to implement them in the CubeSat.

1. An Overview of Thermal Design

This section describes the results of a preliminary thermal design and the analysis of STEP Cube Lab-II deployable solar panel through both a numerical method and a simulated thermal model for predicting the thermal behavior of the solar panel in an in-orbit thermal environment. The numerical estimation of solar panel thermal behavior is derived from the simplified one-dimensional thermal governing equation. The worst hot temperature of the solar panel can be predicted using an analytical solution of a single-lumped mass node. For better solar cell efficiency, a thermal surface finish of the backside of a solar panel is required that ensure solar panel temperature remains as low as possible in orbit by radiating heat in the deep space. The effectiveness of passive thermal designs for the solar panel using different thermal coating was investigated with in-orbit thermal analysis according to the various surface finish to derive the most suitable design for minimizing the thermal gradient of the solar panel. For this, an analytical solution of the solar array temperature under the worst hot condition corresponding to each ideal thermal surface type is performed. A detailed solar panel thermal model included in the system-level satellite thermal model was developed and solved numerically. The in-orbit thermal characteristics of the solar panel were determined and the thermal safety of the design was verified with satisfying the allowable temperature limits.

In this work, an analytical solution of a simplified thermal balance governing equation is used to select an adequate thermal surface finish as a thermal surface treatment. For an actual thermal surface finish, the in-orbit temperature profiles of a solar array based on both the one-node simplified model and the detailed thermal model are evaluated and compared. And, the usefulness of an analytical approach is also examined through compared with the detailed thermal analysis.

2. Numerical Method

The worst hot temperature of a solar panel is predicted through an analytical approach from a single-lumped mass thermal model as shown in Fig 35. The thermal

balance governing equation is a 2nd order partial differential equation. Although simplified by several assumptions, it is hardly solved analytically except for a few special cases. This is because a numerical analysis of a detailed thermal model is the only means to a practical solution. An analytical method is rather simple and can be applied to a lumped-mass thermal model, while a numerical method is a general approach to solve a detailed thermal analysis model for predicting an accurate in-orbit temperature profile. However, the main defect of a numerical approach is that the development of a detailed thermal model requires much time and effort. Therefore, if the worst conditions are considered carefully to predict the worst temperature for some cases, an analytical approach can be used for reliable thermal design, which indicates that a thermal control method can be determined based on an analytical solution. A thermal analysis of a solar array can be approached by both analytical and numerical methods.
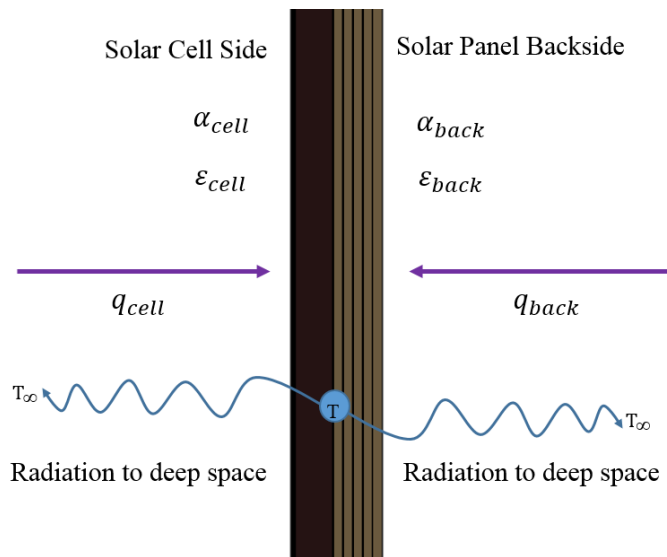
Fig. 35 Simplified Solar Panel Thermal Model through Analytical Approach.

The following assumption has been made to simplify a solar panel thermal model through an analytical approach. The solar panel is assumed to be a single-lumped mass because the solar panel is made up of FR4 material and thus conductive heat transfer is

neglected only radiation exists, both sides of the solar panel are thermally-coupled with the deep space by radiation, and a sun-pointing attitude of a solar array during daylight is considered for the worst hot condition. Based on the abovementioned assumptions, the thermal balance governing equation for a single-lumped mass only with external heating and radiation terms is as follows:

$$mC_p \frac{dT}{dt} = Q_{cell} + Q_{back} - \sigma\epsilon_{cell}A(T^4 - T_\infty^4) - \sigma\epsilon_{back}A(T^4 - T_\infty^4) \tag{4.3}$$

Where, mC_p and T are thermal capacity and solar panel temperature, respectively. The Q_{cell} and Q_{back} are incident heat rate on the solar cell side and backside of the solar panel, respectively. The ϵ_{cell} and ϵ_{back} are IR emittance on the solar cell side and backside of the solar panel. The T_∞ and σ are the deep space temperature and Stephan-Boltzmann constant. Applying the steady-state and deep space condition, which is dT/dt = 0 and T_∞ = 0 K, the solution of the above equation (4.3) become as follows:

$$0 = Q_{cell} + Q_{back} - \sigma\epsilon_{cell}AT^4 - \sigma\epsilon_{back}AT^4 \tag{4.4}$$

The solar panel temperature for the simplified thermal model is evaluated by the following equation:

$$T^4 = \frac{Q_{cell} + Q_{back}}{\sigma A(\epsilon_{cell} + \epsilon_{back})} = \frac{A(q_{cell} + q_{back})}{\sigma A(\epsilon_{cell} + \epsilon_{back})}$$

$$T^4 = \frac{A(q_{cell} + q_{back})}{\sigma A(\epsilon_{cell} + \epsilon_{back})} \tag{4.5}$$

Where, q_{cell} and q_{back} are incident heat flux on the solar cell side and backside of the solar panel.

3. Worst Hot and Cold Case

During daylight, a solar cell side of the solar panel should face towards the direct solar flux perpendicularly to receive as much solar energy as possible. In a low-earth orbit, the earth IR and Albedo are also incidents to the backside of a solar array. The STEP Cube Lab-II CubeSat attitude will be sun-pointing during daylight and eclipse except for the mission operation period. During the mission operation, the satellite is in nadir pointing attitude. The analytical solution for the solar panel in the daylight period of the orbit, the external heating conditions on both sides of the solar panel are as follows:

$$q_{cell} = \alpha_{cell} q_{Solar}$$

$$q_{back} = \varepsilon_{cell} q_{Earth\,IR} + \alpha_{back} q_{Albedo}$$

$$= \varepsilon_{back} q_{Earth\,IR} + \alpha_{back} \beta q_{Solar}$$

However, in the eclipse period of the satellite, the external heating condition is only on the solar cell side of the solar panel due to the earth infrared.

$$q_{cell} = \alpha_{cell} q_{Earth\,IR} \tag{4.6}$$

By applying these conditions in the above equation (4.5), the final analytical solution for determining a solar panel temperature in daylight and eclipse are as follows:

$$T_{daylight} = \sqrt[4]{\frac{\alpha_{cell} q_{Solar} + \varepsilon_{back} q_{Earth\,IR} + \alpha_{back} \beta q_{Solar}}{\sigma(\varepsilon_{cell} + \varepsilon_{back})}} \tag{4.7}$$

$$T_{eclipse} = \sqrt[4]{\frac{\alpha_{cell} q_{Earth\,IR}}{\sigma(\varepsilon_{cell} + \varepsilon_{back})}} \tag{4.8}$$

Heat sources are believed to be a constant maximum value for the worst hot condition in an orbit, so in the analysis, the values of solar flux (q_{Solar}), Albedo (β), and earth IR ($q_{Earth\ IR}$) were considered as low earth orbit standard values of 1420 W/m^2, 0.35, and 249 W/m^2, respectively. As a first step to evaluate the thermal designs of the solar panel, the maximum and minimum temperature in the daylight and eclipse is analyzed according to the four ideal surface finishes on the rear surface of the panel. The absorptivity (α) and emissivity (ε) of the solar cell are considered as 0.61 and 0.85, respectively. Table 23 shows the analytical temperature prediction of the solar panel according to four ideal thermal surface finishes. In this study, we evaluated the global thermal gradient of the solar panel by estimating its temperature deviation between the maximum and minimum temperature values of the solar panel by considering the 1D thermal resistance network model at steady-state temperature for daylight and the eclipse periods. The result shows that solar reflector and flat absorber are the most suitable surface finish in terms of the minimization of maximum temperature in the worst hot case. However, this analytical approach is limited for evaluating the local flatness of thermal distortion on the solar panel.

Table 23 Analytical Thermal Solution Results According to Four Ideal Thermal Surfaces Finishes.

Ideal Surface Finishes	Solar Absorptivity (α)	IR Emissivity (ε)	Max. Temperature (^{o}C)	Min. Temperature (^{o}C)
Solar Reflector	0.01	0.99	47.3	-77.82
Flat Absorber	0.99	0.99	77.6	-77.82
Solar Absorber	0.99	0.01	133.9	-36.91
Flat Reflector	0.01	0.01	102.2	-36.91

4. Thermal Mathematical Model

The analytical approach is sufficient to determine a thermal design under the worst-case conditions although it cannot evaluate in-orbit thermal contours of the solar panel. Thus, to identify a feasible thermal design for minimization of the thermal gradient of the solar panel in an in-orbit thermal environments, a thermal mathematical model (TMM) of the STEP Cube Lab-II as shown in Fig. 36 was constructed by using Thermal Desktop, a CAD-based geometric interface for commercial in-orbit thermal analysis tool of SINDA/FLUINT. The SINDA/FLUINT has often been used to determine the transient and steady-state response of various thermal and fluid flow networks.
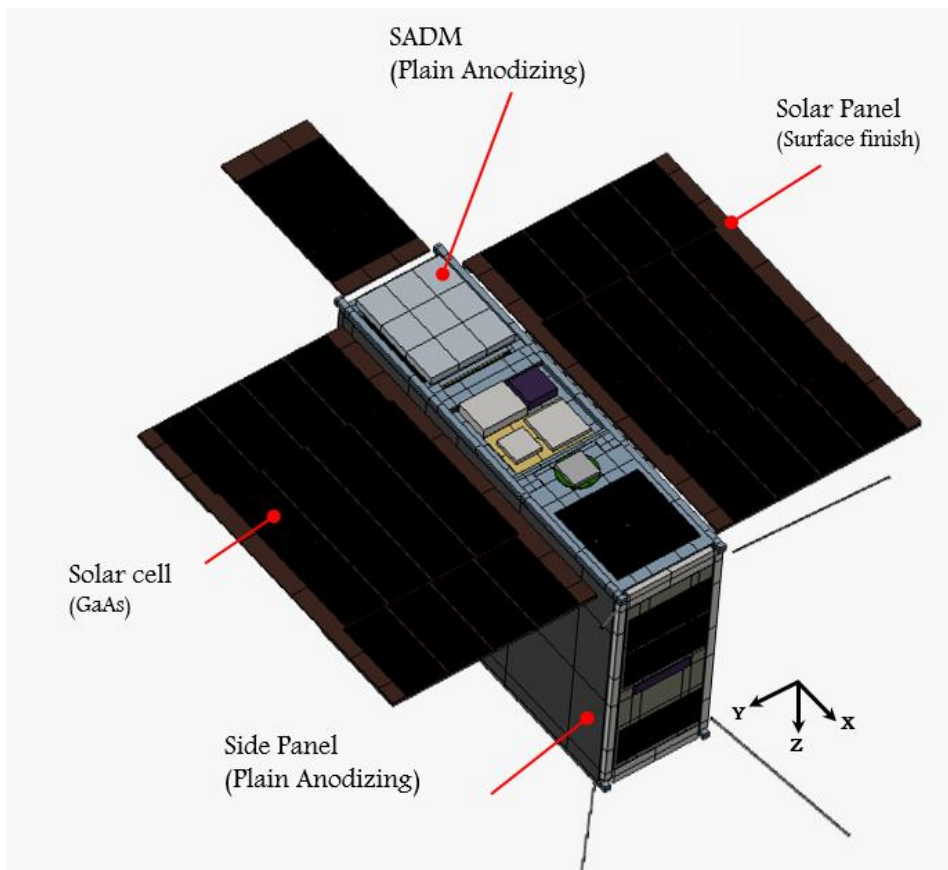

Fig. 36 Thermal Mathematical Model (TMM) of the Solar Panel.

The detailed solar panel thermal model has divided into 5×4 nodes on a panel

surface, which is 325.4 mm × 193 mm in size. A total number of 2230 nodes were constructed for thermal modeling of the CubeSat. Tables 24 and 25 summarize the thermo-physical and optical properties that were used during thermal analysis, respectively. Generally, a fixed-type solar array is attached to the spacecraft bus through the hinges which are made from a very low conductive material, it can be assumed that the solar array is nearly thermally isolated from the spacecraft bus [113]. In the TMM, the thermal conduction from and to the CubeSat structure with the solar panel is assumed nearly thermally isolated although the total isolation is impossible thus the thermal coupling between the solar panel and the CubeSat structure through the hinges were considered as 0.3 W/K that is determined based on the hinge with the black anodizing surface finish. Similarly, the thermal coupling between the solar cells to panel and solar panel to stiffener was considered as 2,000 W/m²/K and 59.18 W/K, respectively. The allowable temperature limit of the solar panel is not defined because the objective is to identify a feasible thermal design based on a comparison of the thermal gradient of the solar panel. However, in general, the allowable solar cell temperature range is specified as -100 ºC to +120 ºC.

Table 24 Thermal-physical Properties Applied for Thermal Analysis.

Items	Material	Density (kg/m³)	Conductivity (W/m-K)	Specific Heat (J/kg-K)	Allowable Temperature (ºC)
Solar Panel & Stiffeners	FR4	1850	0.81 (In-plane) 0.29 (Out-of-plane)	1200	-50 to 110
CubeSat Structure	Al-6061	2700	167.9	961.2	-196 to 585
Solar Cells	GaAs	5320	46.05	350	-100 to 120
Adhesive Tape	3M™ 966	1012	0.178	59.18	-40 to 232

Table 25 Thermo-optical Properties Applied for Thermal Analysis.

Items	Material	Solar Absorptivity (α)	IR Emissivity (ε)	α/ε
Solar Panel & Stiffeners	FR4	0.75	0.89	0.84
Solar Cell	GaAs	0.612	0.85	1.08
Solar Panel Surface Coating	Black Anodizing	0.88	0.88	1.00
	White Paint	0.20	0.88	0.22
	Silver Teflon Tape	0.09	0.78	0.11
	Kapton Tape	0.40	0.67	0.59

The thermal analysis of the solar panel through the TMM as shown in Fig. 36 is based on a passive thermal control strategy using the suitable material selection for solar reflector by surface coatings. For in-orbit thermal gradient minimization of the solar panel under various operating conditions, four thermal design cases on the solar panel are proposed as summarized in Table 26. The selected thermal designs are based on the application of black anodizing, white paint, silver teflon tape, and kapton tape surface finishes on the front and rear surfaces of the solar panel.

Table 26 Thermal Design Surface Coating Cases for the Solar Panel.

Case	Solar Panel Front-side	Solar Panel Rear-side
1	Black Anodizing	Black Anodizing
2	White Paint	White Paint
3	Silver Teflon Tape	Silver Teflon Tape
4	Kapton Tape	Kapton Tape

5. Orbit Profile

The thermal gradient of the satellite is highly influenced by orbital geometry and the resulting patterns in eclipse timing [114]. The STEP Cube Lab-II has no propulsion therefore satellite resides in a similar orbit that it will be ejected by the rocket at approximately 700 km attitude, 97.13° inclination. The orbital period is 96.68 minutes and the eclipse duration varies as a function of the beta angle (β), the angle between the orbit plane and the Earth-Sun vector. The value of β varies between 0° to 75° over the course of several weeks as the orbit slowly precesses. When β = 0°, the orbit plane is coincident with the Earth-Sun vector and the eclipse duration is 35.2 minutes, its maximum value. Conversely, when the β = 45°, the orbit plane is nearly orthogonal to the Earth-Sun vector and the satellite is in daylight throughout the entire orbit, eclipse duration is zero. For the analysis, the orbital parameters and thermal conditions for worst hot and cold cases were assumed as listed in Table 27 to evaluate the critical temperature of the solar panel. The time-dependent external heat fluxes corresponding to the defined orbit are obtained from SINDA/FLUINT. The attitude of the satellite will set in such a way that the solar panel is always facing the Sun direction except for the imaging period. The bottom surface of the satellite (main body (-Z)) axis will point towards the nadir only during the imaging period in the orbit.

Table 27 Orbital Parameters and Environmental Fluxes for Thermal Analysis.

Parameter	Hot Case	Cold Case
Orbit Type	Sun-synchronous	
Altitude (km)	700	
Inclination (deg.)	97.13	
Period (sec.)	5801.23	
Season	Winter Solstice	Summer Solstice
Date (YY/MM/DD)	2022/09/10	2022/06/21
LTDN	17:00	12:00
Beta Angle (deg.)	-75.114	-2.884
RAAN (deg.)	64.214	269.38
Solar Constant (W/m^2)	1346	1287
Albedo Coefficient (%)	0.35	0.30
Earth IR Flux (W/m^2)	249	227
Eclipse Period (sec.)	0	2116

Figures 37 (a) and (b) show examples of orbital profiles of the solar panel under the worst hot and cold conditions, respectively. The worst hot and cold cases were determined based on the orbital winter solstice and summer solstice. The worst hot and cold conditions corresponding to the cases when the CubeSat is in the winter solstice with the highest incoming heat flux and the summer solstice with the lowest incoming heat flux, respectively. The eclipse periods for the hot and cold cases were 0 and 35.26 minutes, respectively, according to the seasonal variation of the beta angle between the
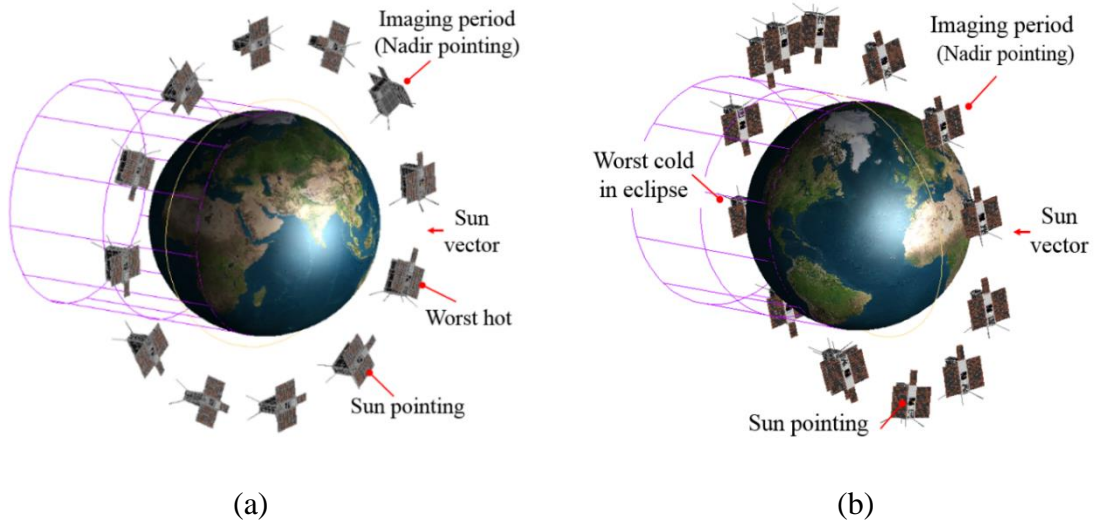
orbital plane and the Sun.

(a)   (b)

Fig. 37 Examples of Orbit Profiles of the STEP Cube Lab-II (a) Worst Hot Case and
(b) Worst Cold Case.

6. Analysis Result

As the first step to evaluate the thermal designs of the solar panel, the temperature of the solar panel was analyzed according to the case 1 thermal coating of black anodizing on the front and rear surface of the solar panels under the worst hot and cold conditions. This is because the solar panel is the most dominant factor for the thermal gradient of the satellite during in-orbit thermal environments due to its large area. The satellite in the worst hot and worst cold in eclipse position of worst hot and cold cases as indicated in Fig. 37 is considered for the analysis result. In this study, we evaluated the global thermal gradient of the solar panel by estimating its surface temperature deviation between the maximum and minimum temperature values of the panel, this approach is limited for evaluating the local flatness on the solar panel.

Figures 38 (a) and (b) show the analyzed maximum (T_{max}) and minimum (T_{min}) temperature profiles of the solar panel in accordance with the thermal design of case 1 at worst hot and cold orbital cases of winter and summer solstices of the satellite,

respectively. The representative temperature contours of the solar panels in accordance to the thermal design of case 1 in orbit periods of winter and summer solstices of the satellite are shown in Fig. 39 and Fig. 40, respectively. That represents the temperature gradient on the panels in the worst period of winter and summer solstices. The results show that the temperature gradient of the solar panel mainly depends on the variation of the solar flux on the panel due to the orbital revolution and roll maneuvering of the satellite in the imaging period. The albedo and earth IR are the dominant factors for temperature gradient on the solar panel. At the worst hot case of the winter solstice, the maximum and minimum solar panel temperatures with case 1 thermal design are 44.2 °C and 15.0 °C, respectively. As there is no eclipse period on the worst hot orbital case, the solar panel temperature is only decreased during the imaging period where the satellite is roll maneuver from Sun pointing to the nadir pointing. However, the temperature is only decreased in the orbital worst cold situation in the eclipse since the solar panels are shaded by the earth in which the imaging cycle has a less dominant effect on the variance of the temperature of the solar panel as the beta angle is close to zero degrees. At the worst cold case of the summer solstice, the maximum and minimum solar panel temperatures with case 1 thermal design are 48.2 °C to 15.0 °C.
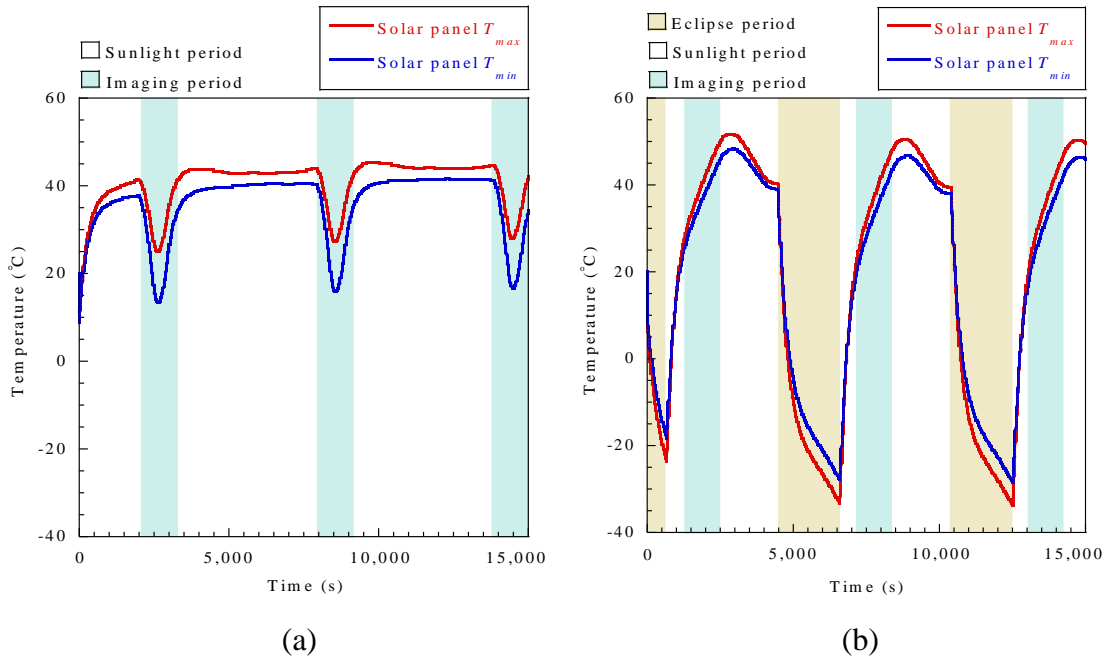
Fig. 38 In-orbit Temperature Profiles of Solar Panel with Case 1 Thermal Design at (a) Worst Hot Case and (b) Worst Cold Case.
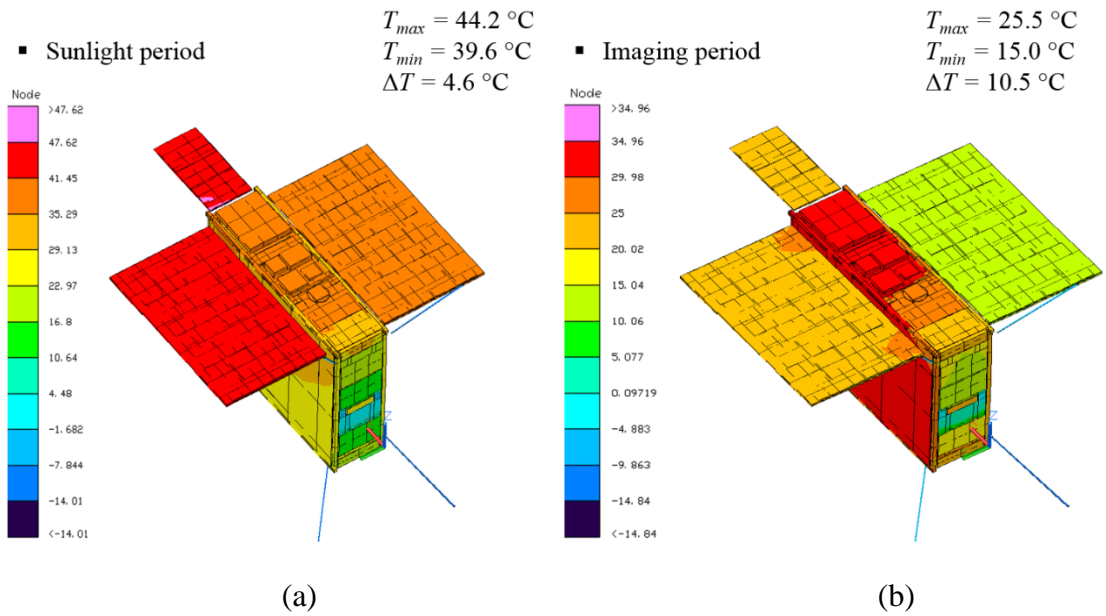

Fig. 39 Temperature Contours of the Solar Panel with Case 1 Surface Finish at Worst Hot Orbital Case of (a) Sunlight Period and (b) Imaging Period.
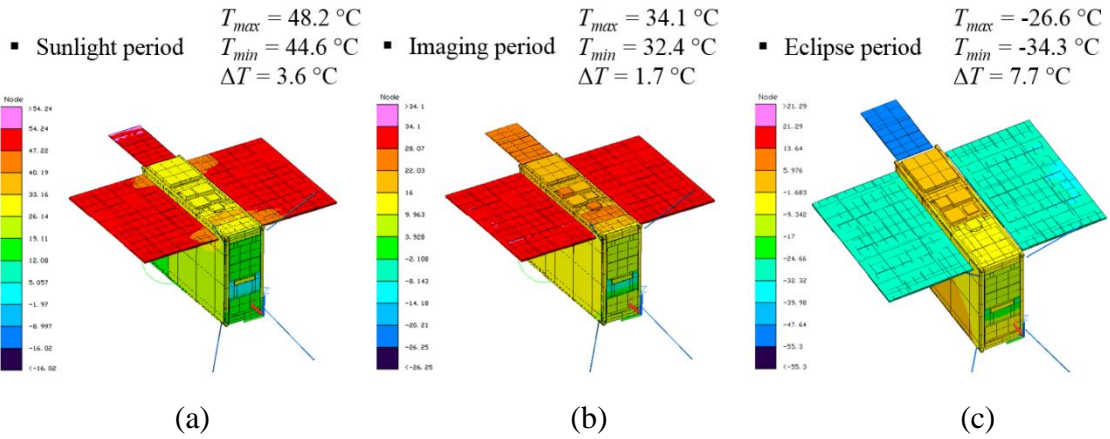
Fig. 40 Temperature Contours of the Solar Panel with Case 1 Surface Finish at Worst Cold Orbital Case of (a) Sunlight Period (b) Imaging Period and (c) Eclipse Period.

Figures 41 (a) and (b) summarize the analyzed temperature gradient of the solar panel in accordance with the various surface finish cases at worst hot and cold orbital cases of the satellite, respectively. In particular, the largest temperature gradient of ΔT = 14.5 °C is observed in the eclipse period of the worst cold orbital case while applying case 2 surface coating because of the much lower solar absorptivity and high emissivity optical property of white paint compared to other cases. The maximum temperature of the solar panel in the sunlight period is lower than the other cases while applying the white paint due to the low absorptivity although the minimum temperature in the eclipse is higher. Thus, the thermal design based on the white paint might be less suitable because it cannot maintain a uniform temperature state of the solar panel in the worst cold case although it shows excellent performance in the summer solstice.
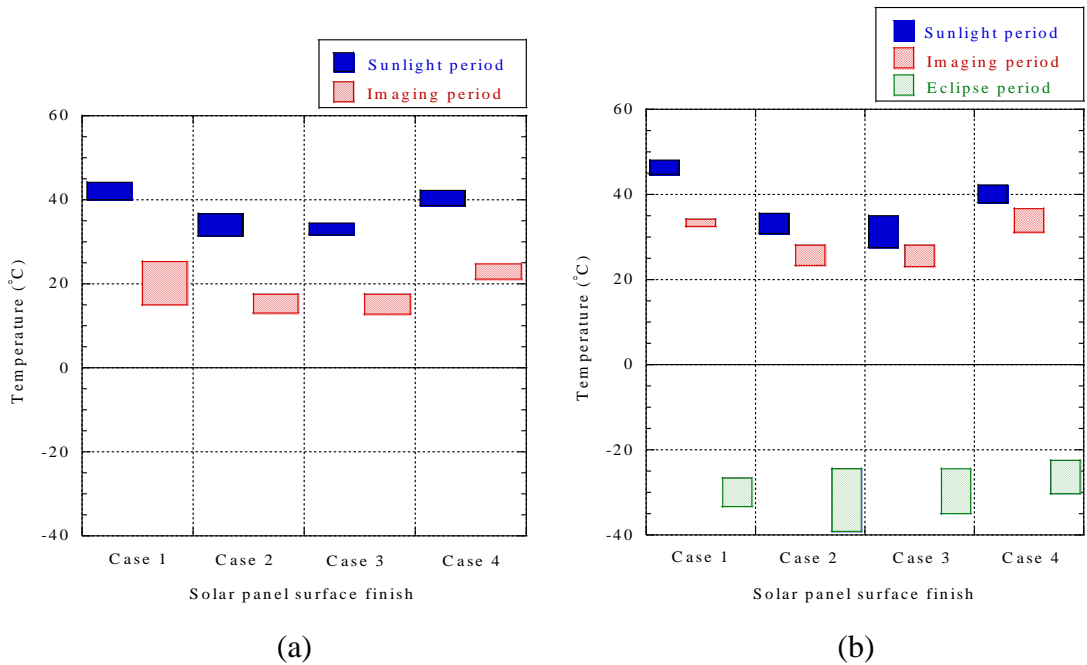
Fig. 41 Maximum Temperature Gradient of the Solar Panel with the Surface Finishes Cases in Orbital Periods of (a) Worst Hot Case and (b) Worst Cold Case.

The minimum temperature of the solar panel in the eclipse period of the worst cold case can be achieved with the application of black anodizing because of the high solar absorptivity and emissivity values than other cases. The maximum temperature in the sunlight period of the worst cold case with the application of black anodizing is 48.2 °C which is greater by 12.7 °C than the white paint case. Moreover, the white paint and silver teflon tape have shown excellent performance in hot case although the minimum temperature in the eclipse is worst. Hence, solar panel thermal design with surface finishes of case 1 and case 4 is feasible for minimization of the thermal gradient during an entire in-orbit mission. Furthermore, the in-plane thermal conductivity of the FR4 is only 0.81 W/m-K thus as shown in the temperature contours of the solar panel in Fig. 39 the temperature gradient on the panel due to the heat transfer from the CubeSat structure is the dominant effect. Therefore by the application of a surface coating or other insulating methods, it is better to insulate the heat transfer through the hinges as possible to minimize the temperature distortion on the solar panel.

V. Experimental Validation Result

A. Viscoelastic Multi-layer Stiffeners for Vibration Attenuation on Solar Panel

The effectiveness of constrained layer passive damping treatment on the PCB based panel for vibration attenuation is experimentally evaluated. The main design driver is to attach thin stiffeners by double-sided viscoelastic acrylic tape on the panel to enhance the damping performance through the shear deformation [115]. Viscoelastic materials possess both elastic and viscous properties. Many polymeric materials exhibit internal damping due to the rearrangement of long-chain molecules when the material undergoes deformation. The viscoelastic material can be applied to the structure in two ways; unconstrained or free layer damping and constrained layer damping. Unconstrained damping is applied to the system by coating viscoelastic material on one or both sides of the base structure, on the other hand, in constrained treatment; the viscoelastic material is sandwiched between two elastic plates. The base and constraining layers can be of different materials. In the unconstrained damping treatment, the viscoelastic material is subjected to extensional deformation during cyclic deformation, whereas in constrained layer damping, the material is subjected to shear deformation. The viscoelastic materials are highly dependent on the working temperature and frequency, and their damping characteristics change under different temperature and frequency ranges [116].

Extensive literature is available on damping of structural vibrations and noise by employing a viscoelastic layer sandwiched between two elastic layers. For instance, Nashif et al. [117] reported that in the optimal working temperature regime, the viscoelastic material operates with a maximum modulus. In addition, they concluded that the energy dissipation in constrained damping treatment is highly dependent on the viscoelastic core layer thickness, structure shape size, and thickness of the constraining layer as well as the vibration frequency. Sun and Lu [118] considered that the

effectiveness of the constrained layer depends on the high difference in the moduli of the elastic and core layers. Hu et al. [119] stated that the attenuation capacity of the constrained layer damping is due to the difference between in-plane displacements of the based and constraining elastic layers and the low stiffness of the core viscoelastic layer. Furthermore, Maly et al. [70] experimentally investigated the life cycle of viscoelastic material for Hubble space telescope solar array 3 damper through subjecting the material specimens to an accelerated life test to assess the damper's ability to maintain nominal performance over the 10-year on-orbit design goal. The results show the stiffness of the system increase over time ranging from 8% to 19% because the viscoelastic bond actually developed further with time, and this conclusion was supported by the post-cycling ultrasonic inspections results of the specimens, however, the minimal change in loss factor, ranging from 0% to 4.5% was observed.

Most of the previous studies of constrained layer damping on structure have concentrated primarily on the technique of finite elements. However, due to the modeling complexity of the composite structure and the difficulty in accurately describing the damping characteristics of viscoelastic material, the dynamic behavior and internal function of multilayer treatments in vibration suppression of structures in the simulation approximation process are not entirely correct [120-122]. Hence, in this study, the experimental method is implemented to validate the effectiveness of viscoelastic multi-layer stiffeners for vibration attenuation on the solar panel, which is the most appropriate way to validate the design.

1. Design Description

To demonstrate the effectiveness of stiffeners with viscoelastic acrylic tapes for launch load attenuation of the solar panel, a 3U sized solar panel as shown in Fig. 42 was fabricated. The demonstration model of the dummy solar panel is mainly comprised of a PCB panel, thin PCB stiffeners, and viscoelastic acrylic tapes. The PCB panel is made out of FR4 material with dimensions 320 mm × 82 mm × 1.6 mm, which provides a mechanical interface for the integration of stiffeners and solar cells. Thin PCB

stiffeners as shown in Fig. 42 of thickness 0.4 mm were attached to the rear surface of the PCB panel by double-sided $3M^{TM}$ 966 acrylic tape.
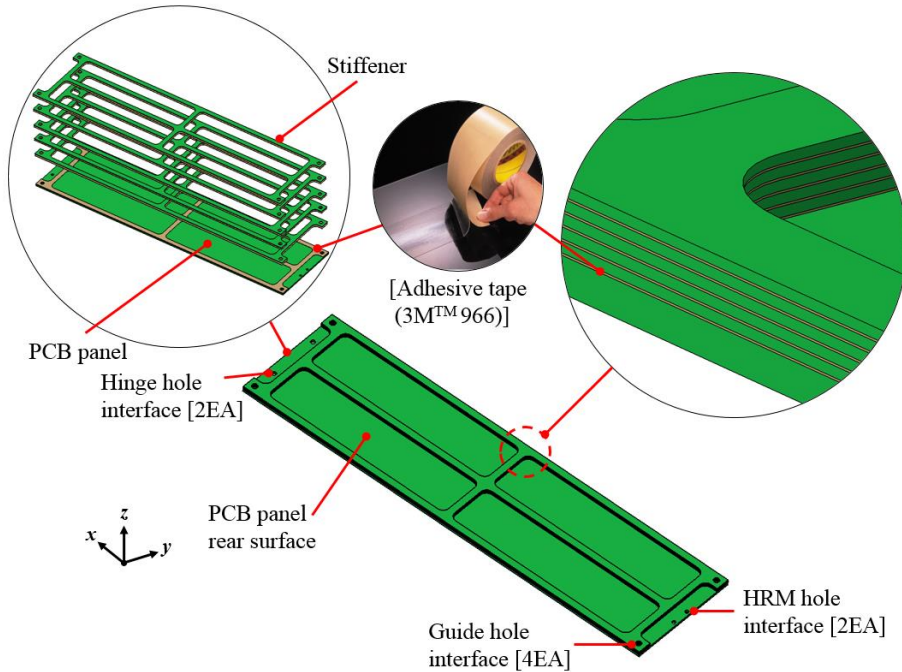
Fig. 42 Illustrative Design Configuration of 3U CubeSat's Deployable Solar Panel.

Figure 43 shows the front and rear view of the demonstration model of the 3U solar panel. The HRM and hinge are not considered in this design because the implementation of HRM could influence the dynamic behaviour of the panel due to the constraint condition variation. However, holes interfaces for HRM and hinge on the panel is built that holes were used to mount the panel on the test jig during the tests. Table 28 summarizes the mass budget of the demonstrated model of the solar panel without employing HRM and hinge. The total mass of the solar panel proposed in this study is 141 g.

- 103 -

(a)   (b)
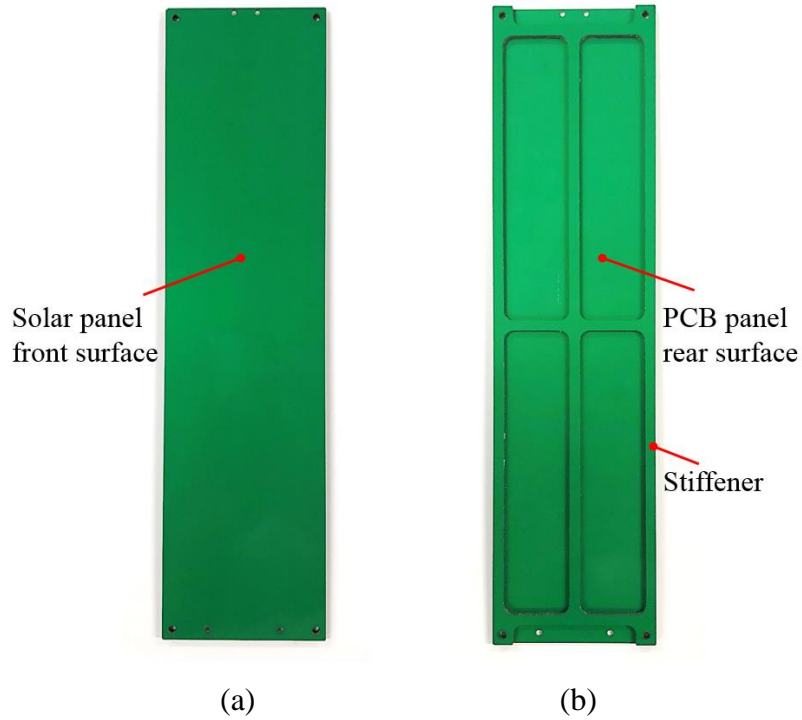
Fig. 43 Demonstration Model of 3U Solar Panel: (a) Front View and (b) Rear View.

Table 28 Mass Budget of Demonstration Model of the Solar Panel.

Item	Mass (g)
PCB Panel	93
5 Layers of PCB Stiffeners	45
3MTM 966 Acrylic Adhesive Tapes	3
Total	141

2. Basic Dynamic Characteristics

The vibration attenuation of the constrained layer damping with viscoelastic materials is highly dependent on geometric parameters such as cross-sectional area, shape, and thicknesses of the viscoelastic and constraining layers because the energy

dissipation actions mainly resulted from the shear deformation behavior between the interlaminated surfaces [123, 124]. To investigate the basic dynamic characteristics of the solar panel, such as damping performance and stiffness, with respect to the number of adhesive tape attachment conditions, free-vibration tests were performed. The following three cases were considered: solar panel without stiffener, solar panels with 3 and 5 layers of stiffener in order to clarify the characteristics of the design in each case. In the above-mentioned cases, the free-vibration tests were carried out at ambient room temperature of 25 ℃ for the solar panel under boundary condition that both hinge and HRM holes interfaces are rigidly clamped, which corresponds to a launch stowed configuration of the solar panel. The roving hammer method was used to excite the solar panel to its free-vibration. An accelerometer sensor to obtain the time domain response was attached at the center of the panel to measure the frequency responses of the solar panel. The experimental test result shown in Fig. 44 demonstrates the time histories of the free-vibration response of the solar panels. Figure 45 shows the PSD acceleration responses of solar panels with various numbers of interlaminated stiffeners. The results show that the vibration of the solar panel can be effectively suppressed by employing the stiffeners with viscoelastic acrylic tapes.
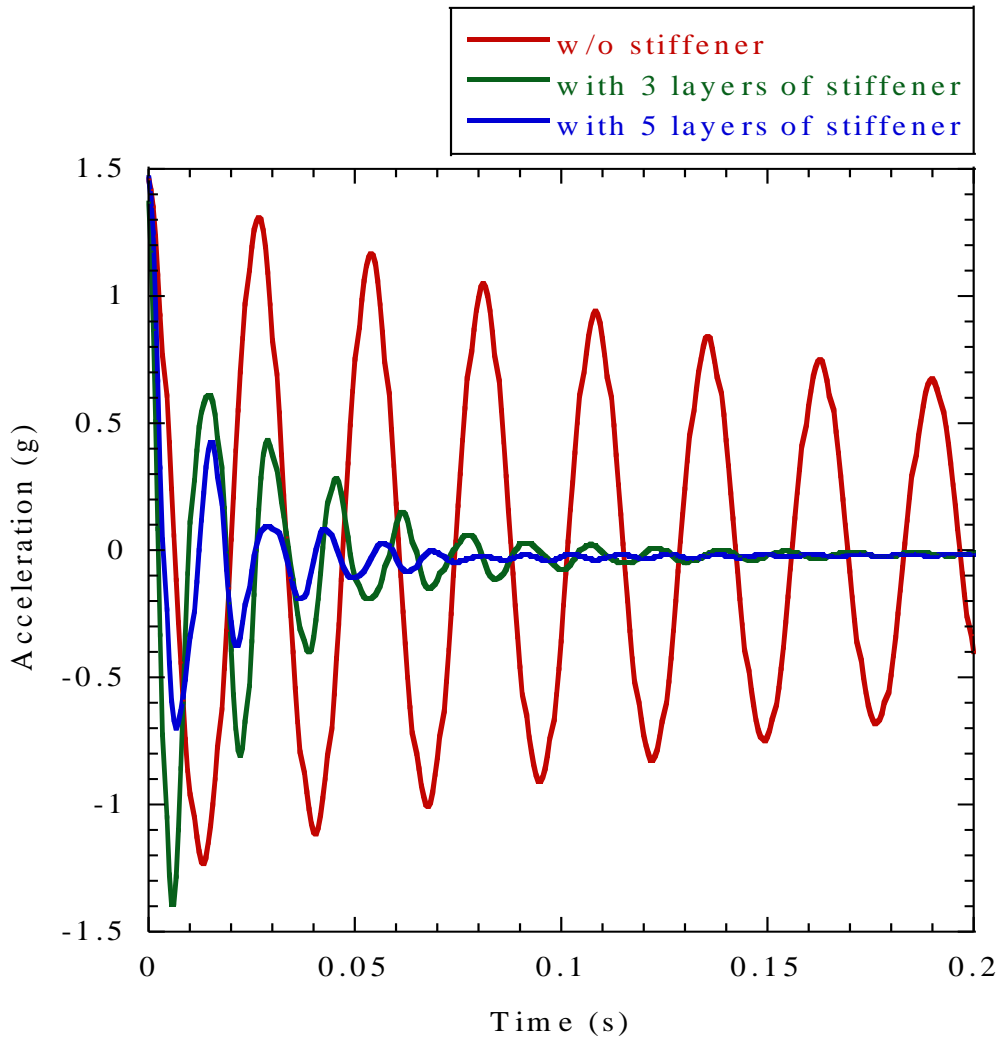
Fig. 44 Free-vibration Test Results of the Solar Panels with Various Number of
Stiffeners.
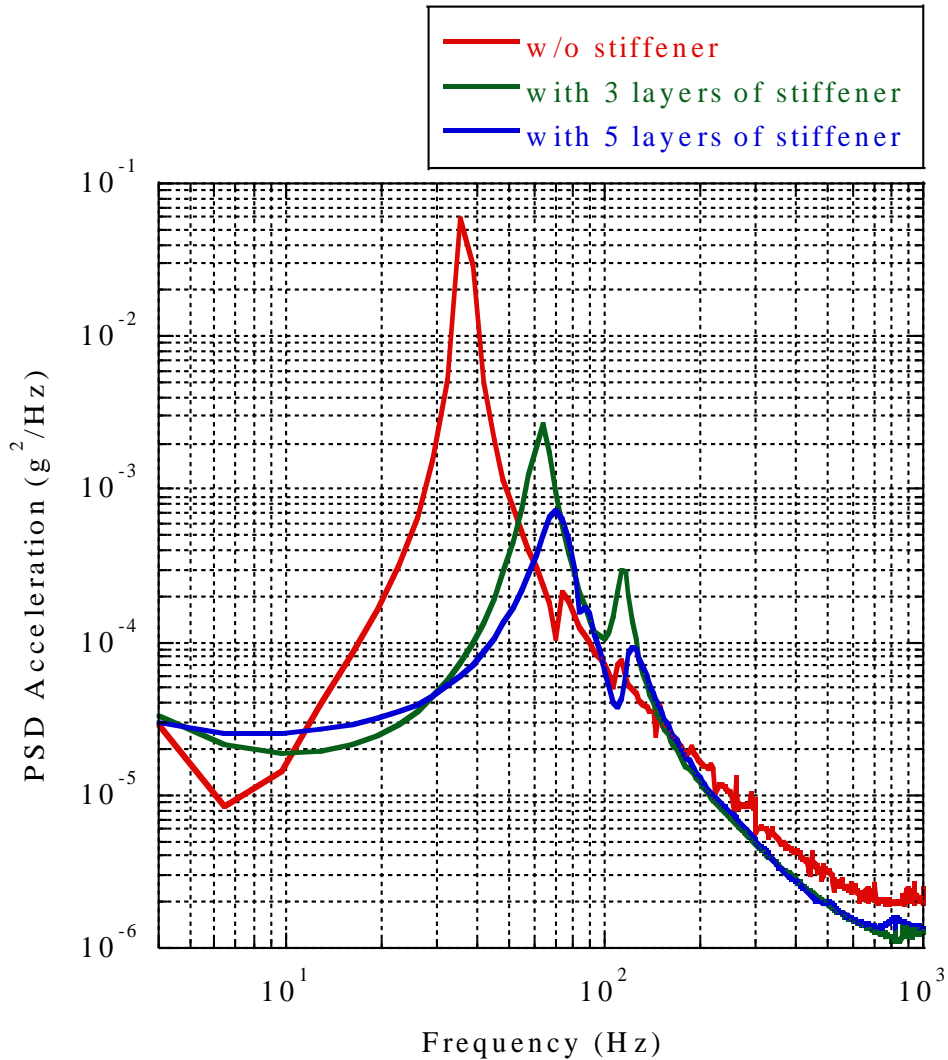
Fig. 45 The PSD Acceleration Responses of Solar Panel with Various Numbers of Interlaminated Stiffeners.

Figure 46 shows the 1st eigenfrequency and damping ratio variation of the solar panel according to the application of stiffener. The damping ratios of the solar panel after application of 3 and 5 layers of viscoelastic stiffener were respectively 0.019 and 0.061, which is higher by factors of 9.5 and 30.5 as compared to 0.002 that measured in the non-stiffener solar panel. Furthermore, the 1st eigenfrequency calculated from the vibration periods of the solar panel without stiffener, with 3 and 5 layers of stiffener

were 36.70 Hz, 63.52 Hz, and 68.81 Hz, respectively. The result indicates that the application of viscoelastic multi-layered stiffener substantially enhanced the vibration damping as well as increased the stiffness of the panel due to the fact that large shear strain, and relatively tough surface roughness achieved by molecular attraction force of acrylic polymers of the viscoelastic acrylic tapes.
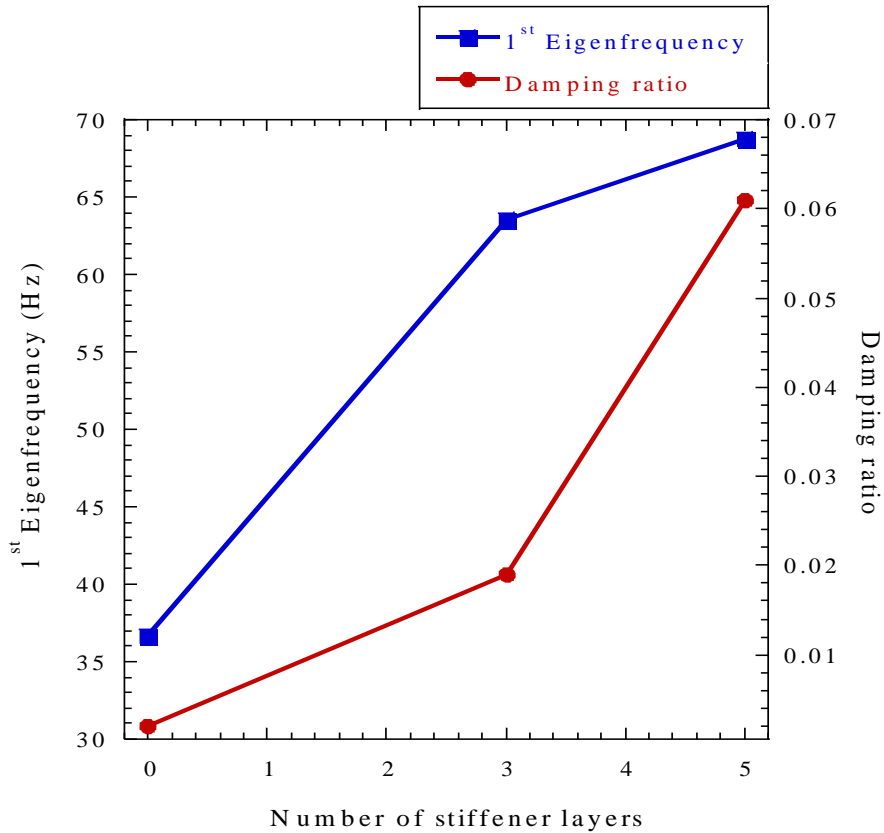
Fig. 46 The 1st Eigenfrequency and Damping Ratio of the Solar Panel According to the Number of Stiffener Layers.

The stiffness difference between the solar panel without stiffener and with the implementation of 3 layers of the stiffener is relatively higher than that observed between the 3 and 5 layers cases. This indicates that increasing the number of stiffeners raised the panel rigidity to some extent, however, not as a linear function of stiffener numbers. However, this kind of asymmetry was not observed in the damping

performance of the panel because the amount of energy dissipated in a viscoelastic layer depends on the magnitude of shear strain in that layer. Thus, the number of viscoelastic stiffeners layers should be taken into account as a design parameter by considering the panel mass, stiffness, and lateral thickness imposed in the system requirements.

For CubeSat applications, where rapid slew maneuvers for the acquisition of a target point are required, the interaction of deployable solar panels with the attitude control system could generate a rigid body motion that can significantly degrade performance in terms of pointing accuracy and acquisition time [125]. With the current trend of large deployable solar panels with low-frequency modes to meet the power requirement in CubeSat design, the residual vibration at the end of attitude maneuver as well as slewing time increases that significantly degrades the performance requirement of future advanced missions [126]. However, the proposed design of solar panel could also substantially suppress the vibration of solar panel during in-orbit operations that may overcome the above issues to some extent. Nevertheless, the properties of viscoelastic materials used in constrained layer damping are generally much more sensitive to temperature that could affect the dynamic characteristics of the solar panel according to the temperature condition. Thus, free-vibration tests of solar panels considering in-orbit deployed configuration were performed at various temperature ranges in the thermal chamber. The objective of this test was to investigate the characteristic variations of the deployed solar panel, such as damping performance and stiffness in various temperature conditions for predicting its design effectiveness under in-orbit operation. Thus, the specified temperature range was set as -20 ℃ to 60 ℃, which covers the expected glass-transition temperature range of 3M^{TM} 966 acrylic tape, although the allowable temperature range is -40 ℃ to 232 ℃. In order to ensure the uniform temperature distribution throughout the specimen panel, the thermal dwell time at a particular test temperature was set to one hour. Figure 47 shows the free-vibration test setup configuration of the solar panel in a thermal chamber. The solar panel was cantilevered on the test jig to acquire the characteristic variation in the low-frequency range that could help to predict design effectiveness under in-orbit deployed configuration. To measure

the frequency responses of the panel during the free-vibration test, an accelerometer sensor was attached at the center of the solar panel.
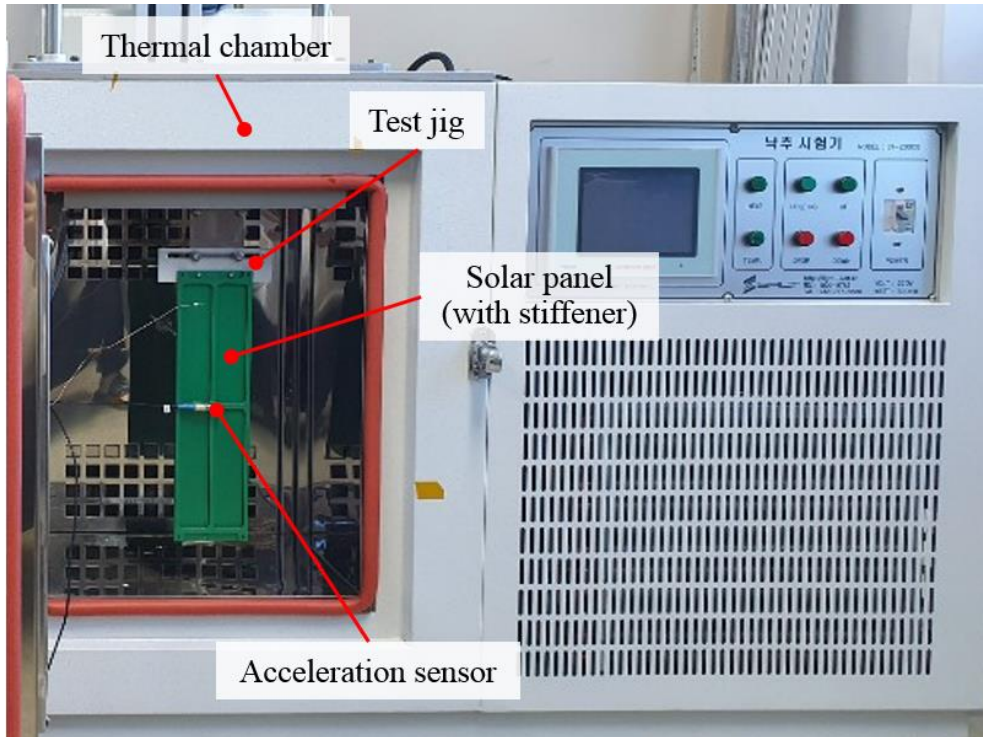
Fig. 47 Free-vibration Test Setup Configuration of the Solar Panel in a Thermal Chamber.

Figure 48 shows the 1st eigenfrequency of solar panels in accordance with temperature variations. The result indicates that the stiffness of a solar panel varies with environmental temperature due to the structural phase transition effect of the material. The solar panel with 5 layers of stiffener exhibited relatively higher stiffness overall temperature conditions, compared to the other cases. This is explained by the fact that nearly stable adhesive strength is maintained on thin multiple stiffeners by high-temperature acrylic tapes such that the stiffeners used as a constraining layer accumulate the equivalent stiffness of the panel.
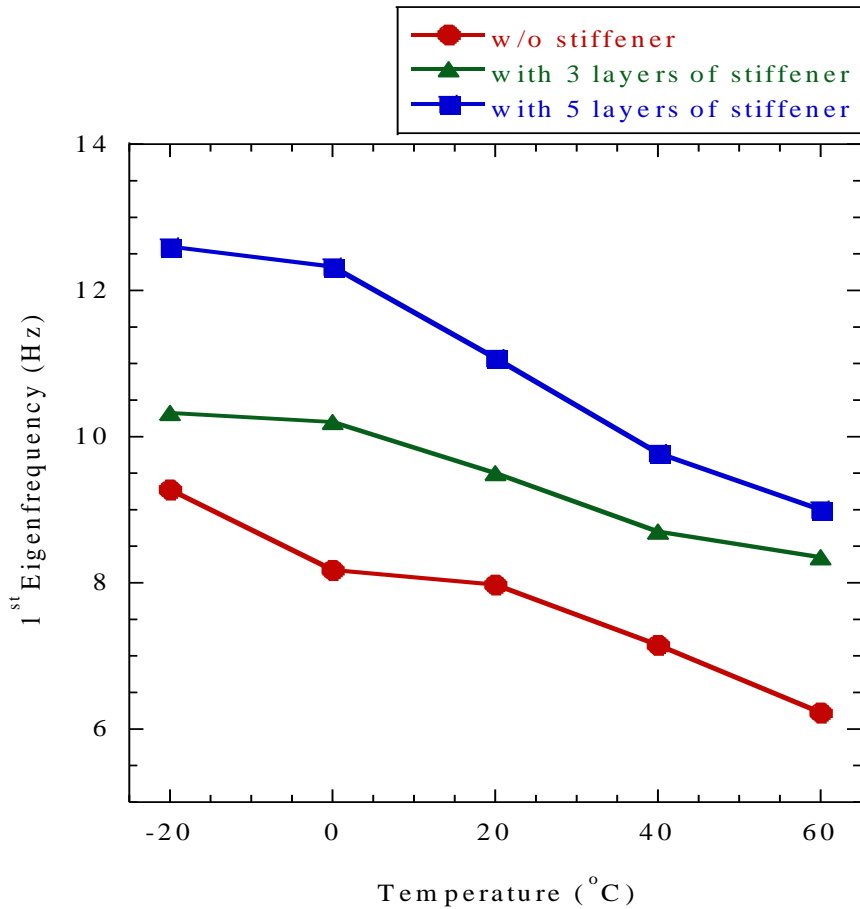
Fig. 48 The 1st Eigenfrequency of the Solar Panels under Various Temperature
Conditions.

Figure 49 shows the damping ratio of the solar panels in accordance with the
temperature variations. Likewise to stiffness, the damping ratio of the solar panel is also
profoundly dependent on the temperature because the energy dissipation action is
accomplished mainly by the shear strain of viscoelastic layers. At lower temperatures,
so-called glassy region, the viscoelastic acrylic tape instigate to behave as an elastic
material thus the damping performance of the panel remains lower owing to the high
storage modulus. As the temperature increases, the damping ratio of the solar panel is
relatively higher because the viscoelastic acrylic layer dissipates maximum vibration
energy owing to the shear deformation until the glass transition temperature is reached

[127]. Meanwhile, this is the point of maximum shear strain and further increase in temperature results decreasing the solar panel's damping ratio owing to the viscous molecules of adhesive tape instigating a rubbery state above the glass transition temperature. Where both the storage modulus and the loss modulus of viscoelastic material remain small, minimum energy dissipation is therefore obtained from the cyclic shear deformation of adhesive tapes. As shown in the result, all panels showed similar damping behaviour with temperature variation, although the solar panel employing 5 layers of stiffener exhibited a relatively higher damping magnitude than other cases due to the cumulative shear strain contributed by increased cross-sectional area of adhesive tapes.
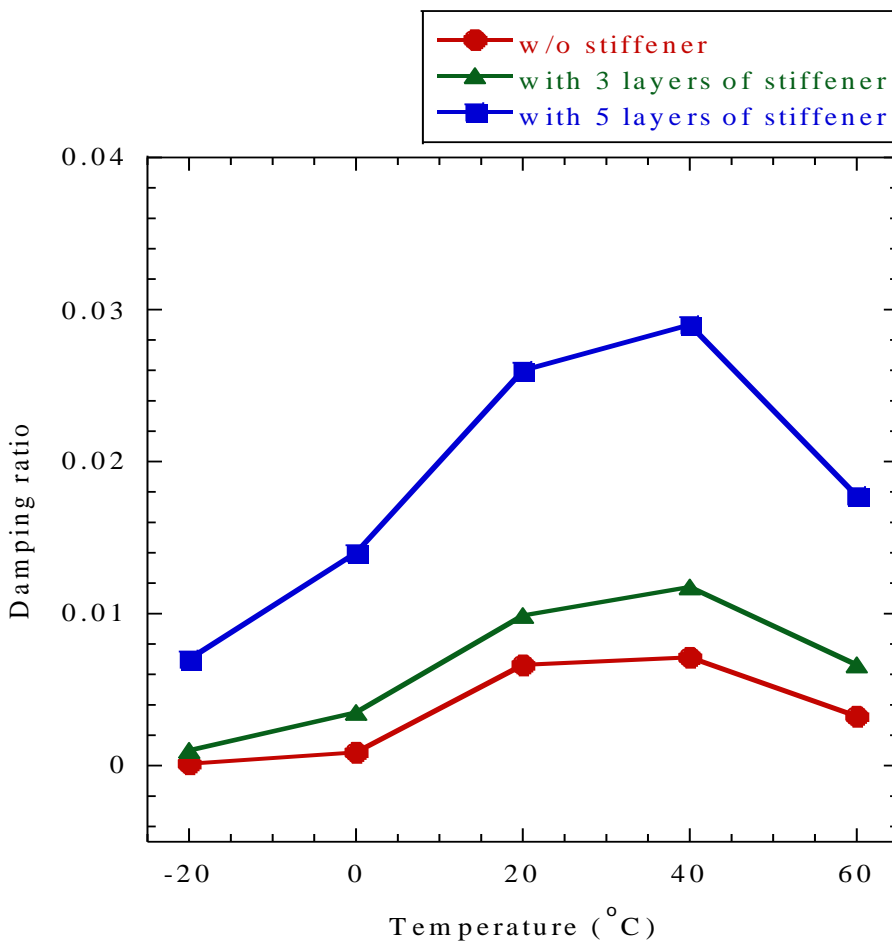

Fig. 49 Damping Ratio of the Solar Panels under Various Temperature Conditions.

3. Launch Vibration Test

To evaluate the structural safety and damping performance of the viscoelastic stiffener based solar panel in launch environments, launch vibration tests such as sine and random vibration tests were carried out under the qualification level of the launch load specified in Tables 16 and 17. The main objective of these tests was to verify the design effectiveness of the highly damped solar panel system with viscoelastic acrylic tapes to ensure the structural safety of solar cells in launch vibration loads.

Figure 50 shows an example of a launch vibration test configuration of the solar panel along with z-axis excitation. The demonstration model of the solar panel was rigidly mounted on the electrodynamic vibration shaker (J260/SA7M, IMV Corp.) through the bolt fastening on the HRM and hinge hole interfaces. An accelerometer sensor was attached on the test jig to control the input vibration load. The output acceleration responses of the solar panel were measured by the accelerometer attached at the center of the solar panel. The test was performed at an ambient room temperature of 18 ℃. The structural safety of the solar panel is validated by comparing the variation of the 1st eigenfrequencies of the panel obtained through low-level sine sweep (LLSS) tests performed before and after each vibration test. In order to judge the structural safety of the specimen under launch load, the 1st eigenfrequency variation in LLSS should be less than 5%.
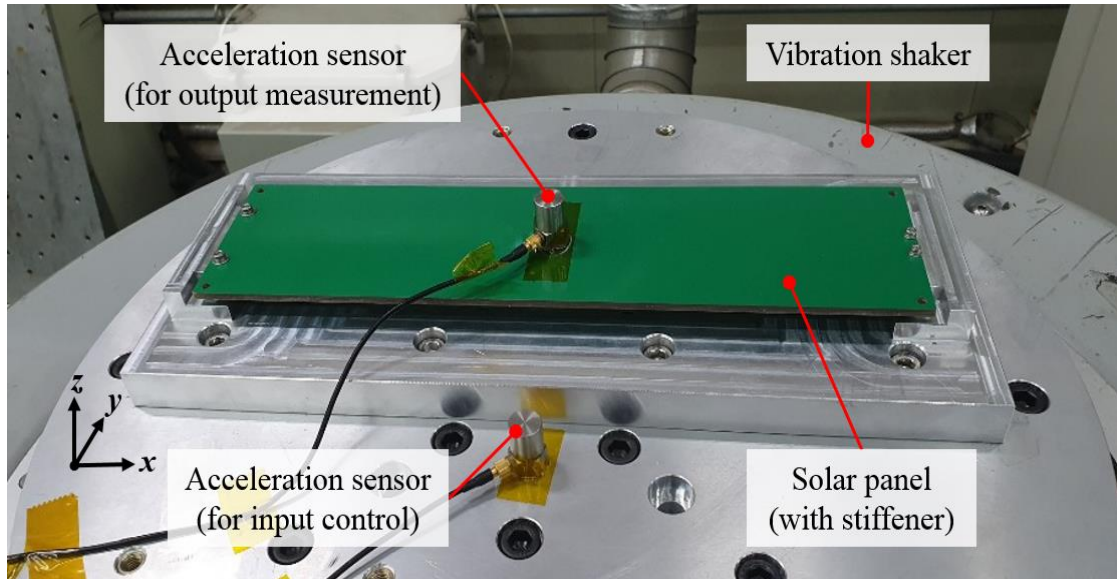
Fig. 50 Launch Vibration Test Setup Configuration of the Solar Panel.

Figure 51 shows the sine vibration test results of solar panels along with z-axis excitation. The z-axis is the most critical axis because it induces the largest dynamic deflection of the solar panel. With respect to the maximum 2.5 g sine vibration input load, the maximum acceleration response of the solar panel without stiffener was 43.72 g which was observed at 47.6 Hz. Moreover, at the same input vibration load, the maximum acceleration response of the solar panels with 3 and 5 layers of stiffeners was 16.59 g and 11.45 g at 58.5 Hz and 73 Hz, respectively. As seen in the results, the solar panel's damping efficiency and stiffness were substantially increased with respect to the number of attached stiffeners. Among those, the solar panel with 5 layers of stiffener exhibited higher damping performance i.e., lower amplification factor than other cases because of the increased number of viscoelastic layers that upsurge shear deformations during panel deflection.
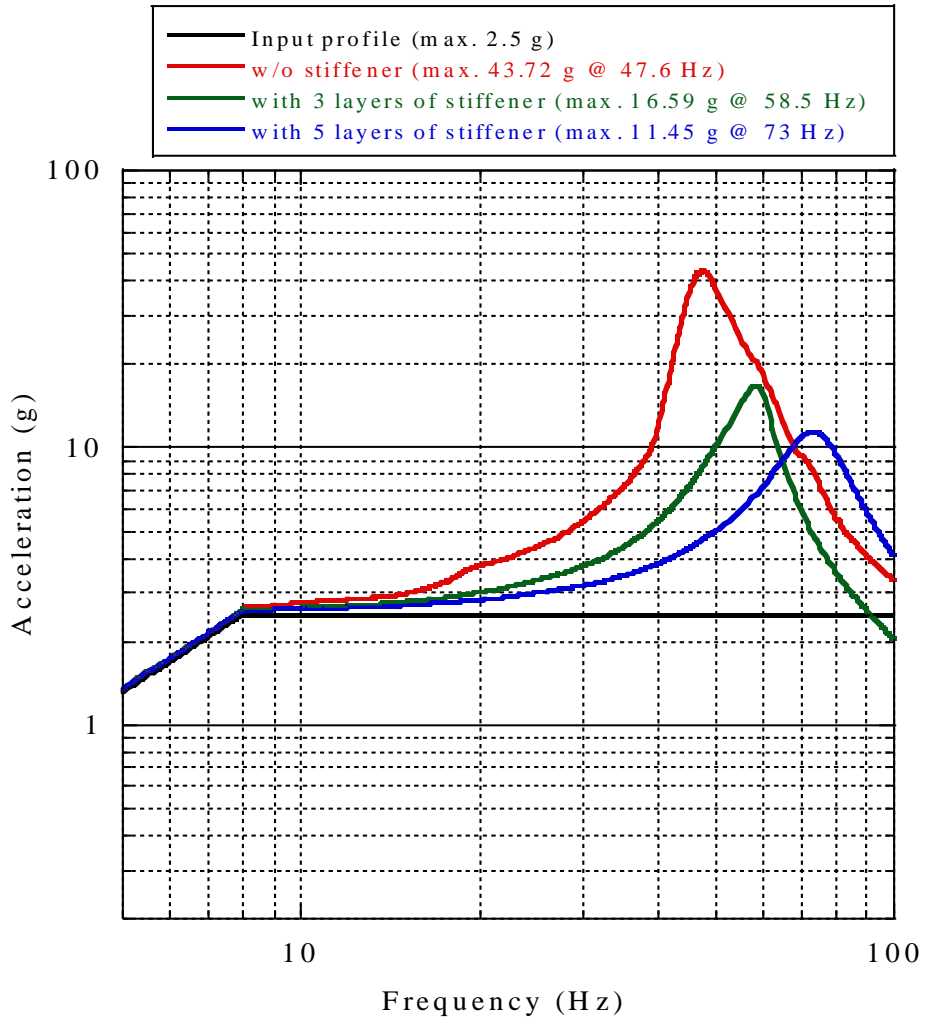
Fig. 51 Sinusoidal Vibration Test Results of the Solar Panels in the *z*-axis Excitation.

Figure 52 shows the random vibration test results along with the *z*-axis excitation of solar panel. The G_{rms} values obtained from acceleration power spectral density (APSD) profiles of a solar panel without stiffener, with 3 and 5 layers of stiffener were 38.42, 14.03, and 12.63, respectively. The output response of the solar panel with 5 layers of the stiffener was lower by a factor of 1.12 than that of the input 14.1 G_{rms} level. Likewise, to the above sine vibration test results, solar panels showed similar dynamic behaviour under a random vibration load.
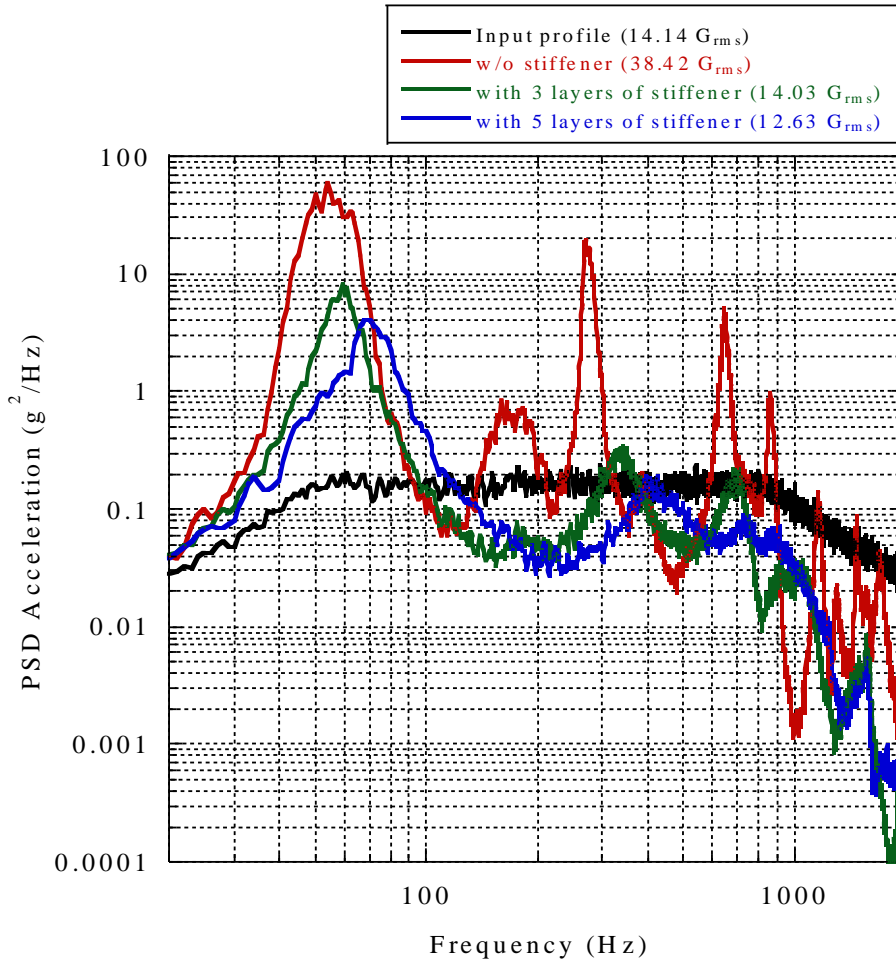
Fig. 52 Random Vibration Test Results of the Solar Panels in the *z*-axis Excitation.

Table 29 compares the 1st eigenfrequencies of the solar panels obtained from the LLSS tests that were performed before and after each vibration test. The tabulated LLSS result shows that the 1st eigenfrequency shifted was within 3.42% throughout the test sequences of the panels, which is within the 5% criterion. In addition, after completion of the launch vibration tests, the visual inspection of the solar panel does not report any crack, dissociation, and plastic deformation on the stiffeners although it is not shown here. These tests and inspection results indicate that the structural safety of the solar panel employing viscoelastic multi-layered stiffeners was successfully verified in qualification level launch environment tests.

Table 29 LLSS Test Results of Solar Panels Before and After Full Level Vibration Test.

Test	Solar Panel	Status	1st Eigenfrequency (Hz)	Difference (%)
Sine Vibration	W/o Stiffener	Before	47.6	2.90
		After	46.2	
	With 3 Layers of Stiffener	Before	58.5	3.41
		After	56.5	
	With 5 Layers of Stiffener	Before	73.0	0.68
		After	73.5	
Random Vibration	W/o Stiffener	Before	47.6	2.90
		After	46.2	
	With 3 Layers of Stiffener	Before	58.5	3.42
		After	56.5	
	With 5 Layers of Stiffener	Before	72.5	1.37
		After	73.5	

Table 30 summarizes the relative dynamic displacement derived from the sensor response measured at the center of the solar panel during the worst excitation axis along the z-direction. The maximum dynamic displacement of the solar panels without stiffener, with 3 and 5 layers of stiffener, under random vibration load, estimated from the three-sigma value of G_{rms} response were 1.39 mm, 0.13 mm, and 0.04 mm, respectively. The dynamic deflection of the solar panel employing 5 layers of stiffener

is significantly reduced by a factor of 34.75 as compared to the solar panel without stiffener. This is owing to the higher vibration attenuation resulted from the increased shear area of viscous layers of acrylic tape. Moreover, the increased natural frequency of the panel also contributed to the reduction in dynamic displacement. Thus, solar panel employing constrained layer damping with viscoelastic acrylic tapes is effective for achieving the design goals of launch load attenuation and minimization of the dynamic deflection of the panel.

Table 30 Estimated Dynamic Displacement of Solar Panels in Vibration Loads.

Test	Solar Panel	Max. Relative Displacement (mm)
Sine Vibration	W/o Stiffener	0.49
	With 3 Layers of Stiffener	0.12
	With 5 Layers of Stiffener	0.05
Random Vibration	W/o Stiffener	1.39
	With 3 Layers of Stiffener	0.13
	With 5 Layers of Stiffener	0.04

4. Highly Damped Deployable Solar Panel Module with a Two Pogo Pin-based HRM

After verifying the effectiveness of constrained layer damping with viscoelastic acrylic tapes for launch load attenuation and minimization of the dynamic deflection of the panel, the dynamic characteristics of the panel in module level is investigated through the free-vibration tests. In order to evaluate the basic dynamic characteristics variation of the panel according to the boundary conditions (with and without implementation of HRM and hinge) a demonstrated model of two pogo pin-based mechanism as shown in the Fig. 20 is fabricated and implemented in the dummy 3U

sized solar panel with five layers of stiffeners. A torsional spring based hinge is used for the panel deployment. Figures 53 (a) and (b) show the front and rear view of demonstration model of highly-damped deployable solar panel module with two pogo pin-based HRM, respectively. The free-vibration tests was performed at ambient room temperature of 25 ℃ in the panel stowed state with consideration of HRM and hinge.

(a)   (b)
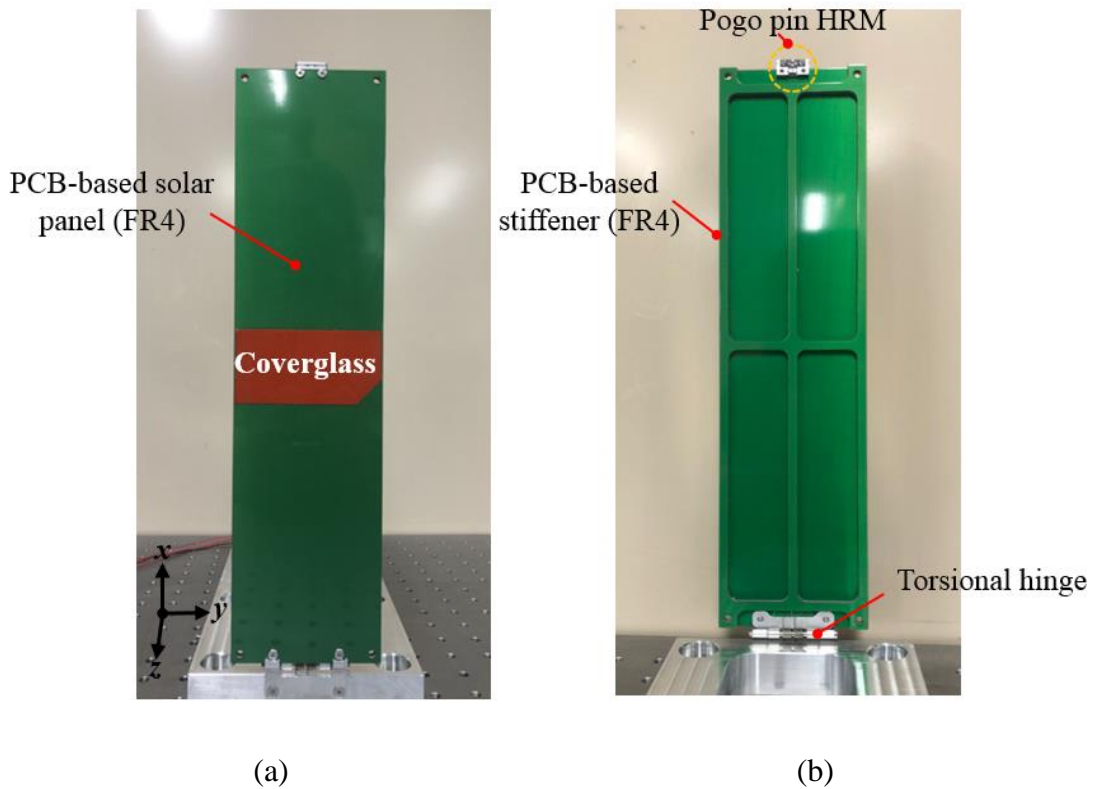
Fig. 53 Demonstration Model of Highly Damped Deployable Solar Panel Module with Two Pogo Pin-based HRM: (a) Front View and (b) Rear View.

Figure 54 summarizes the values of the damping ratio and 1st eigenfrequency of the solar panels based on the clamping boundary conditions. The results reveal that the 1st eigenfrequency of the solar panel module was 58.98 Hz, which is 10 Hz lower than that of the rigidly mounted solar panel employing the same number of stiffeners. This dissimilarity in stiffness was anticipated owing to differences in the solar panel clamping

condition. However, the solar panel damping ratio calculated from the logarithmic decrement equation was 0.118, which is higher by a factor of 1.93 than that of the rigidly mounted solar panel interlaminated with the same number of viscoelastic layers. This is because additional damping occurred at the mechanical tolerance gap of the hinge in the form of friction, and the nylon wire knot of the HRM brackets served as a spring element. Therefore, the damping ratio at the center of the panel increased slightly, as the transmitted vibration load attenuated additionally in the solar panel mounting interfaces. These test results confirm the effectiveness of the viscoelastic multi-layer stiffeners for transmitted vibration attenuation in module level.
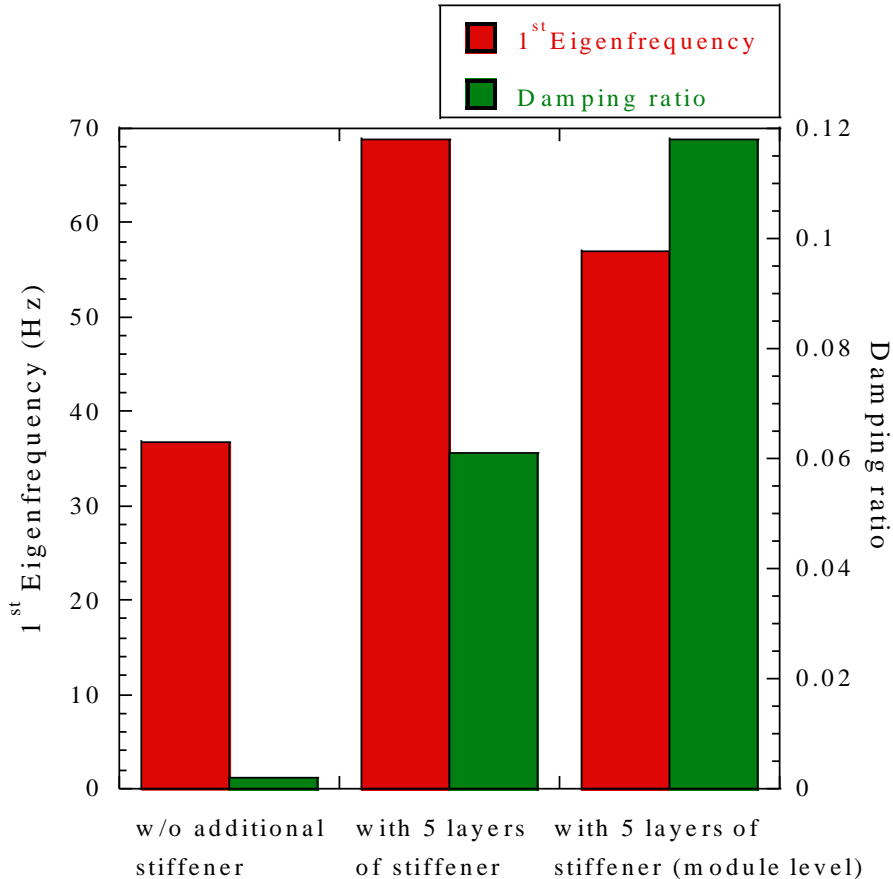
Fig. 54 Basic Dynamic Characteristics of the Solar Panels According to Clamping Boundary Conditions.

Furthermore, to check the functionality of optimized design of two pogo pin based mechanism, the release function test of the solar panel was performed. Figure 55 shows the time history of the input voltage, separation signal, and acceleration of the solar panel measured during the test. The release status data were obtained using the XOR gate of the electrical circuit through the DAQ channel; these data indicate that the solar panel was released within 0.64 s from the initiation of burn wire triggering. In addition, the acceleration response of the solar panel demonstrates that the full deployment of the panel took 2.82 s from the completion of the release action. This test result indicates that two pogo pin-based mechanism functioned well, and the solar panel deployment status was determined in accordance with the temporal electrical connection accomplished by the pogo pins.

Fig. 55 Time Histories of the Input Voltage, Separation Signal, and Acceleration Response Obtained from Release Test of the Solar Panel.

B. STEP Cube Lab-II's Deployable Solar Panel Module

1. Qualification Model

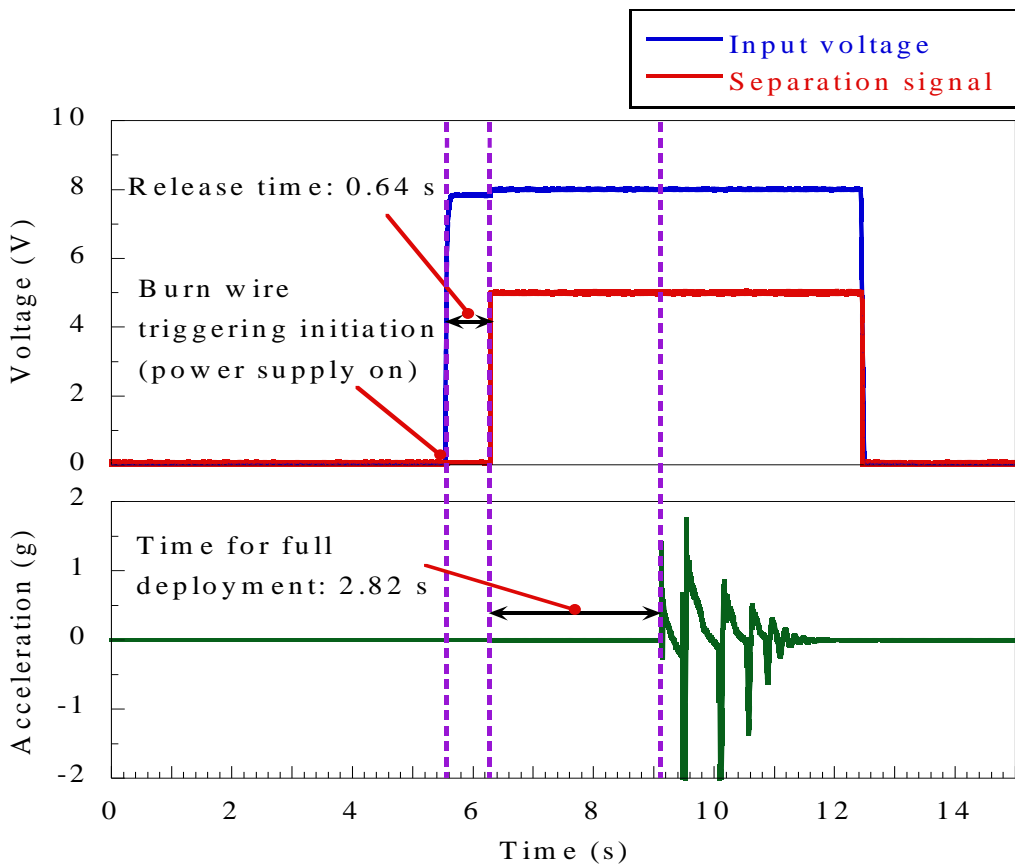After validation of viscoelastic multi-layered stiffeners on the panel for the launch loads attenuation and minimization of dynamic deflection and the applicability of the pogo pin based wire cutting mechanism as an HRM, a qualification model of 6U sized highly damped deployable solar panel module was manufactured and experimentally evaluated for use in the STEP Cube Lab-II. The solar panel proposed herein is effective in guaranteeing the structural safety of solar cells under a launch environment owing to the superior damping characteristics achieved using multi-layered stiffeners with viscoelastic acrylic tapes. Figures 56 (a) and (b) show the qualification model of the STEP Cube Lab-II solar panel module stowed and deployed configuration, respectively.

(a)   (b)
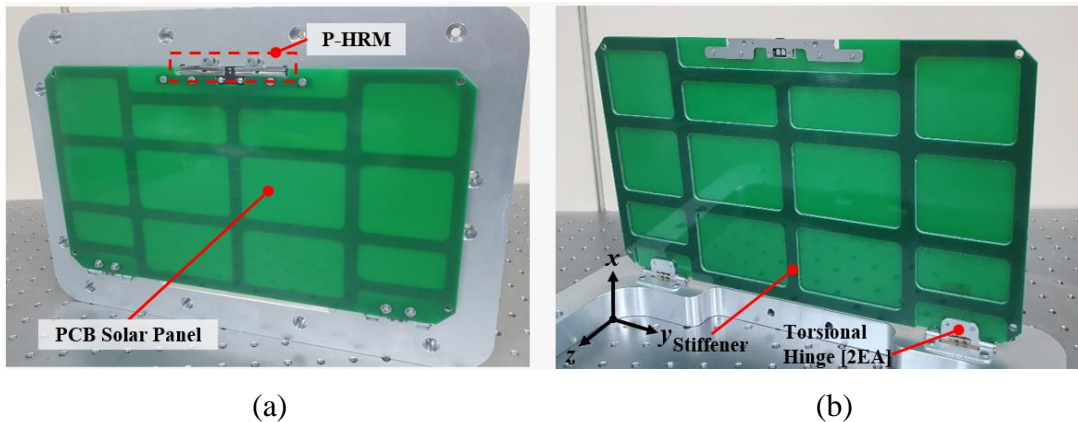
Fig. 56 Qualification Model of the STEP Cube Lab-II Solar Panel Module: (a) Stowed and (b) Deployed.

The five thin stiffeners made up of FR4 material of thickness 0.4 mm were attached on the rear surface of the PCB panel with the adhesive tapes. The stiffeners number on the panel were determined through the experimental test results of the 3U dummy solar panel discussed in the above section, considering the accommodation in P-POD rail interface for dynamic clearance, and the total mass of the solar panel module. Figure 57 shows the integration process of the stiffeners on the PCB panel. Firstly, prepare the

materials and integration tools such as PCB panel, stiffeners, 3M966 tape, integration jig, isopropyl alcohol (IPA), torque wrench, knife and cleaning cloth then wipe the stiffeners and PCB panel using cloth wetted with IPA to remove contaminations. Cut the tape according to the shape of stiffener by knife tip then put it in integration jig through the guide hole interfaces, repeat the process up to the specified number of stiffeners that have to attach on the panel. The PCB panel is then placed on the last stiffer attached with tape after that top guide jig is clamped by M3 bolts tightened on the jig with a desirable torque of 1.1 N-m to apply compression force on the specimen. The adhesive bonding resin of tape was cured for 72 h for secure attachment as recommended on the adhesive tape datasheet [69].
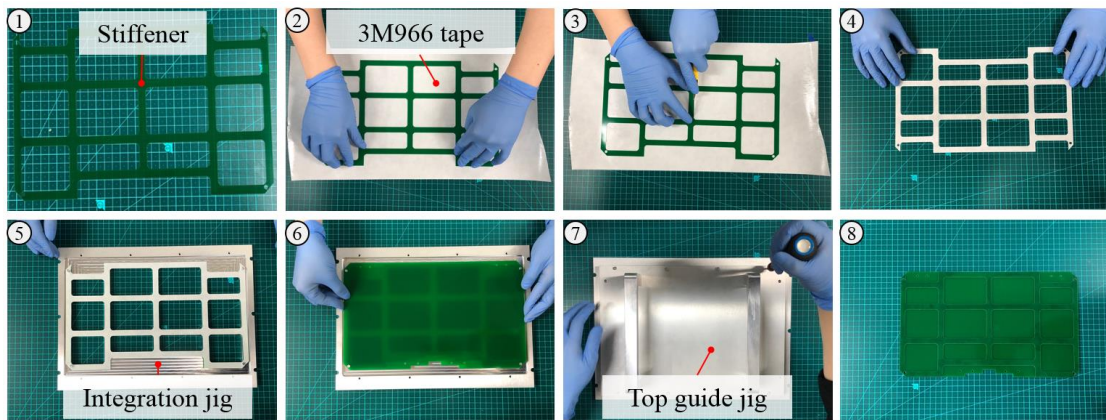
Fig. 57 Integration Process of Stiffeners on the PCB Panel.

The total thickness of the solar panel after integration of the five layers of stiffeners on the PCB panel is 3.7 mm that allows an additional margin of 3.3 mm lateral edge gap on P-POD for a dynamic clearance [34]. Table 31 summarizes the mass budget of the demonstrated model of the solar panel module. The total mass of solar panel module proposed in this study is 306.5 g, which is lower by a factor of 2.04 than that of the 6U sized solar panel module stiffened by applying additional high-pressure laminated G10 material [32].

Table 31 Mass Budget of Demonstration Model of the 6U Solar Panel Module.

Items	Mass (g)
PCB panel	201.5
Five Layers of PCB Stiffeners	85
Five Layers of Adhesive Tapes	3
Pogo Pin-based HRMs	6
Torsional Hinges and Fasteners	11
Total	306.5

2. Basic Dynamic Characteristics

To demonstrate the effectiveness of the proposed solar panel for transmitted vibration attenuation at the module level, a free-vibration test was performed at ambient room temperature of 25 ℃ in the panel rigidly mounted state (bolt fastening on the hinge and HRM hole interfaces of the panel) as shown in Fig. 58. The free-vibration test of a typical solar panel without attaching the stiffeners is also carried out for comparison with the results obtained from the proposed design.
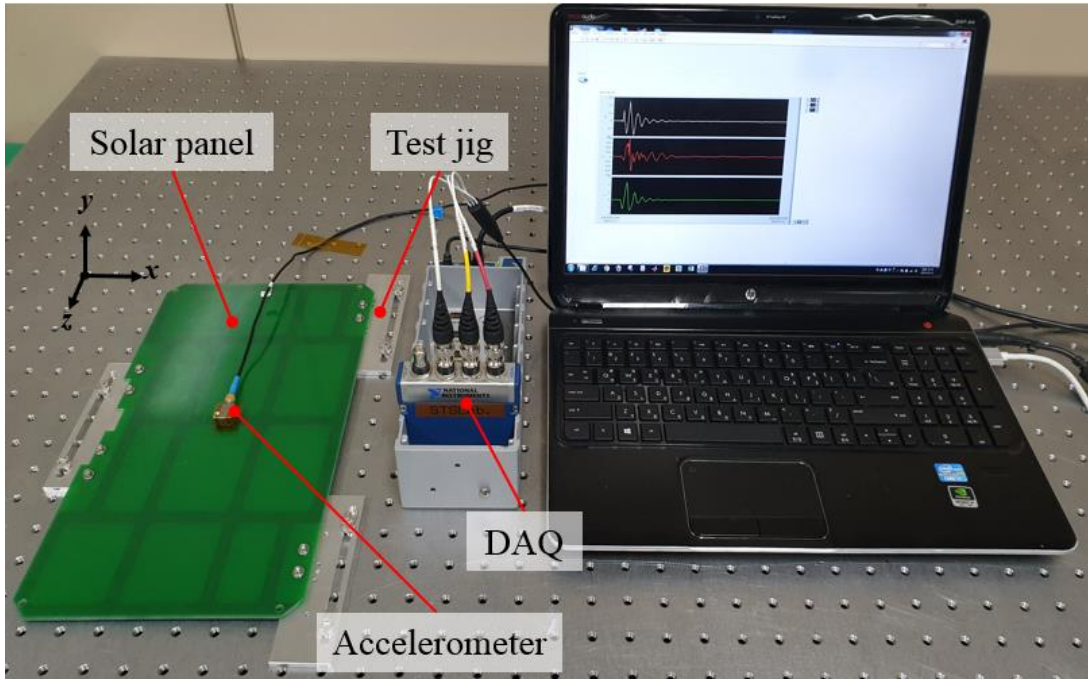
Fig. 58 Free-vibration Test Setup Configuration of the Solar Panel in A Rigidly Clamped State.

The time history of solar panels acceleration response are plotted in Fig. 59. Figure 60 shows the power spectral density (PSD) acceleration responses of solar panels. Figure 61 summarizes 1st eigenfrequency and damping ratio of the solar panels based on stiffener attachment conditions. The results reveal that the 1st eigenfrequency of the proposed solar panel was 110.1 Hz in a rigidly mounted state. The result is similar to that estimated from the simulation results of the panel without HRM and hinge presented in Table 20. However, the stiffness of the panel might be slightly varied in module level due to the different boundary conditions. Furthermore, the damping ratio of the typical FR4 solar panel and VMLSA calculated from the logarithmic decrement equation were 0.036 and 0.141, respectively. The damping ratio of VMLSA is higher by a factor 3.9 than that of the typical solar panel. As predicted in the above section, the result shows that application of viscoelastic multi-layered stiffener substantially enhanced the vibration damping as well as increased the stiffness of the solar panel due to the fact that

large shear strain, and relatively tough surface roughness achieved by molecular attraction force of acrylic polymers of the viscoelastic acrylic tapes.
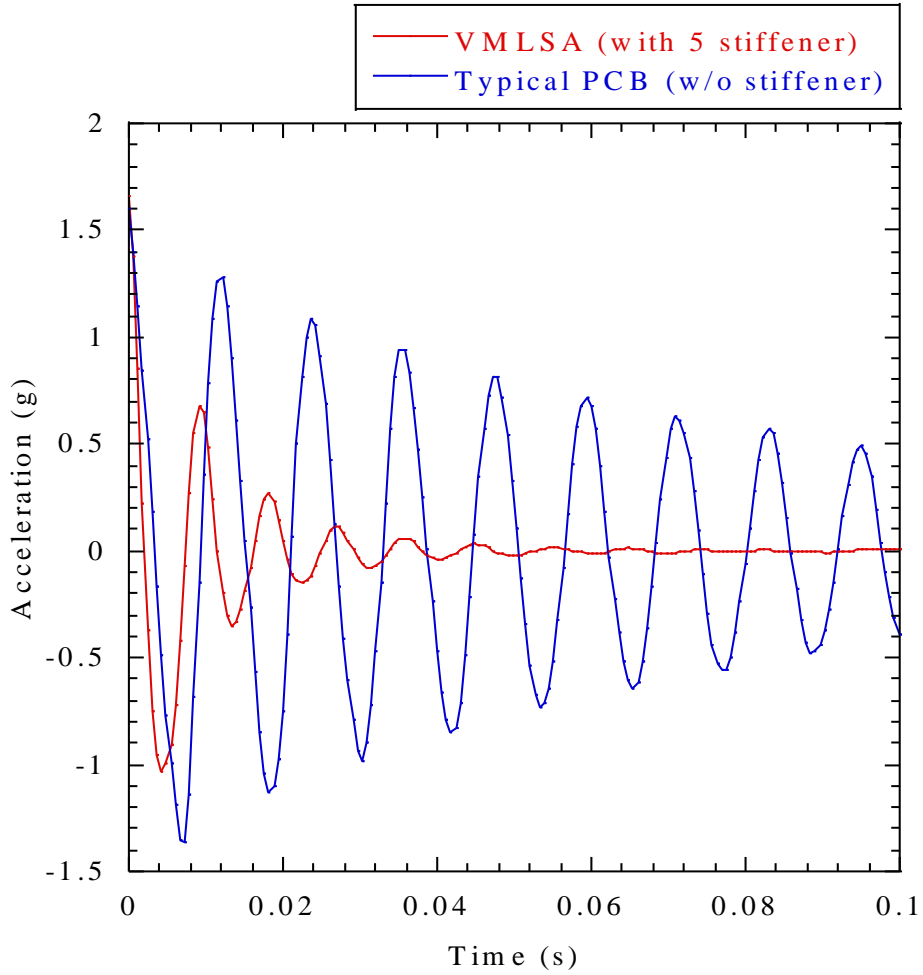
Fig. 59 Time Histories of the Free-vibration Tests of Solar Panels in A Rigidly Clamped State.
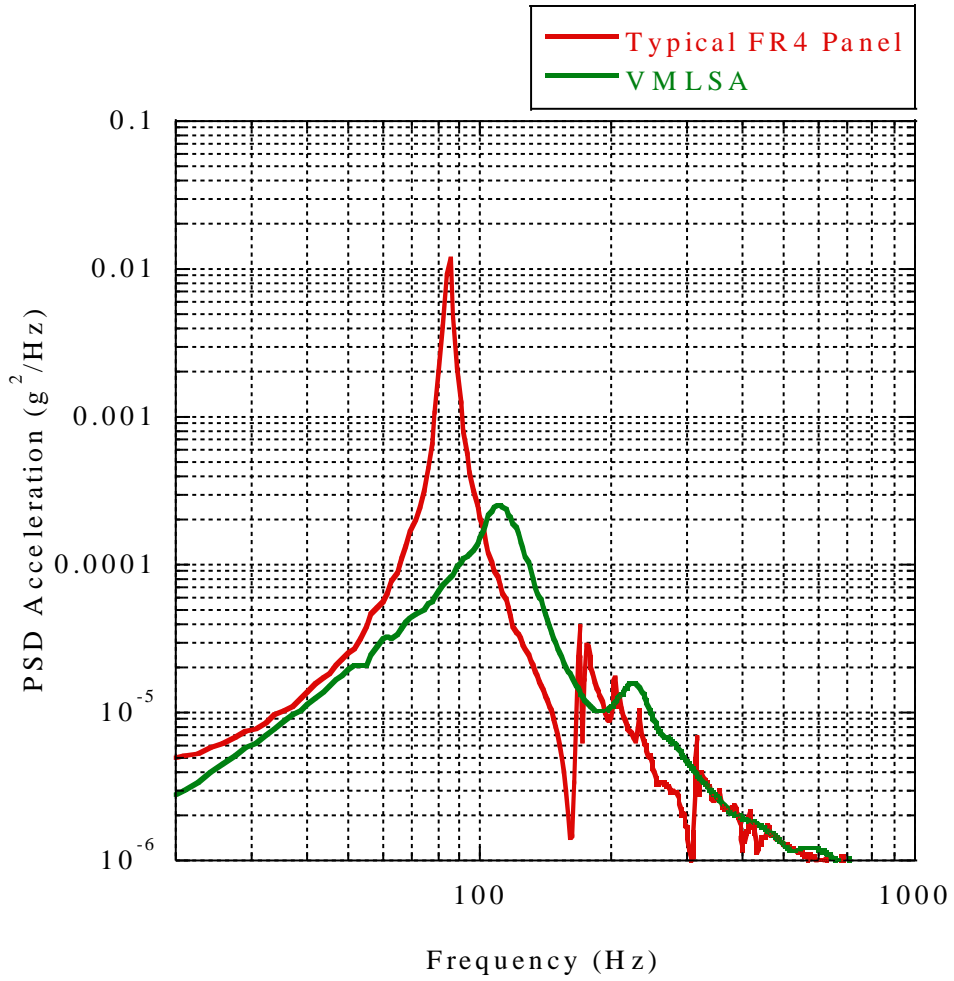
Fig. 60 The PSD Acceleration Responses of the Solar Panels in A Rigidly Clamped
State.
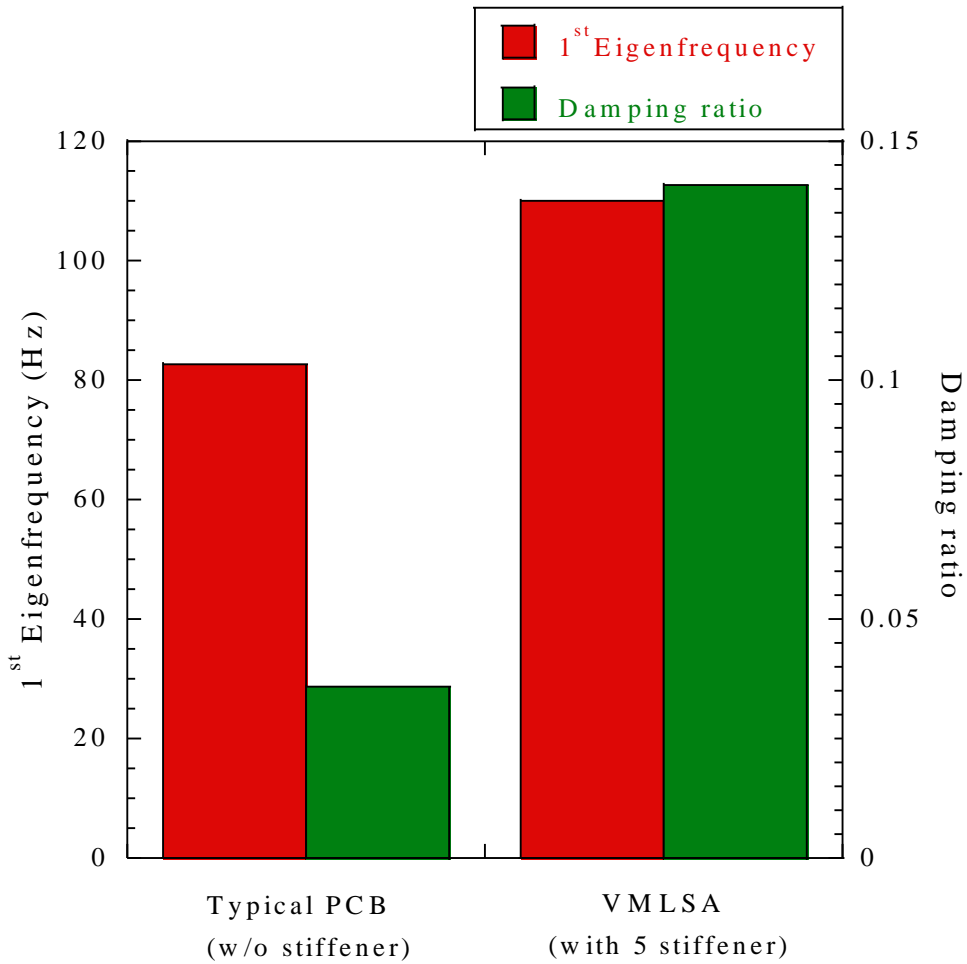
Fig. 61 Basic Dynamic Characteristics of Solar Panels in Stowed Configuration.

In recent years, the complexity of CubeSat missions has been increasing steadily as the platform capability has drastically improved. Missions involving high-accuracy fine-pointing stability for Earth observation and interplanetary explorations are no longer out of the reach of CubeSats. The in-orbit low and medium frequency vibration can also be critical for some on-board equipment and sensors, the microvibrations may degrade the image balance of an observation satellites [128]. In these cases, the use of vibration attenuation systems based on viscoelastic materials makes it possible to reduce or even eliminate these criticalities. The STEP Cube Lab-II also have optical payloads and sensors thus to verify the effectiveness of VMLSA employing viscoelastic constraint

layer damping strategy for the rapid attenuation of panel chattering vibration during its in-orbit performance, we have performed free-vibration test in solar panel deployed state. Figure 62 shows the free-vibration test setup configuration of the solar panel at deployed state. In order to mitigate the gravitational effect, the solar panel was cantilevered on the test jig in such a way that the hinge rotational axis was perpendicular to the test table.
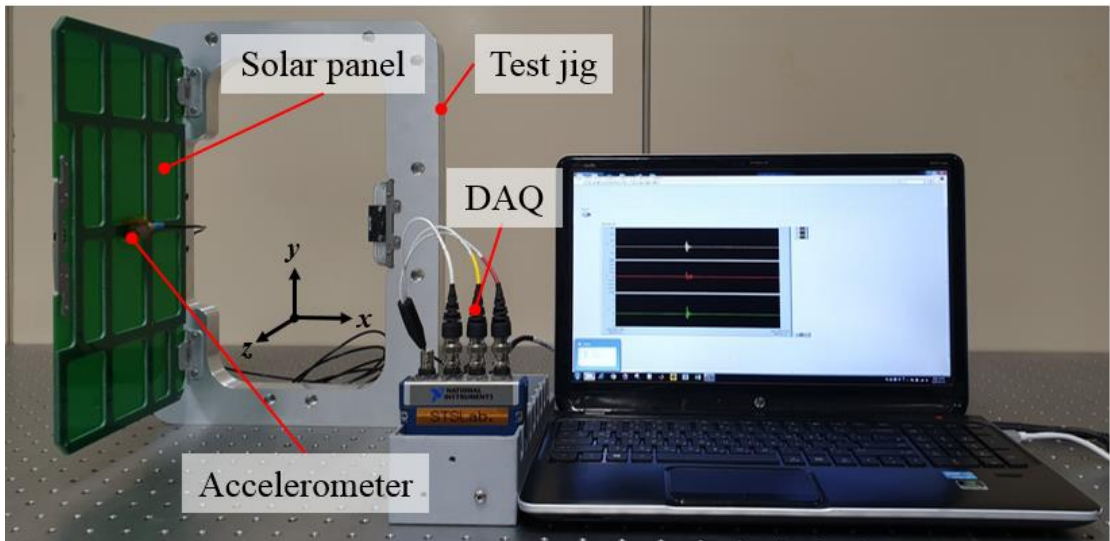
Fig. 62 Free-vibration Test Setup Configuration of the Solar Panel at Deployed Configuration.

Figure 63 shows the time histories of the free-vibration tests of solar panels in the deployed configuration. Figure 64 shows the power spectral density (PSD) acceleration responses of solar panels calculated from the time domain data. The results show that the chatter frequencies of VMLSA are significantly attenuated. Figure 65 summarizes the basic dynamic characteristic of the solar panel with and without the application of stiffeners. The 1st eigenfrequency of VMLSA in the deployed configuration is 1.4 Hz, which is higher by a factor of 1.16 than that of the typical solar panel of 1.2 Hz. Furthermore, the damping ratio of VMLSA is 0.13 which is higher by a factor of 6.7 than a typical solar panel. However, the mass of the VMLSA is increased by a factor of

1.47 as compared to the typical FR4 PCB panel. The results indicate that the viscoelastic constraint layer damping strategy could also substantially suppress the residual vibration on the panels caused by the rigid body motion of satellite during the attitude slew maneuvers for the acquisition of a target point. That could significantly minimize the performance degradation of the satellite employing larger size solar panels in terms of pointing accuracy and acquisition time. These test results confirm that the proposed solar panel guarantees enhanced dynamic characteristics, such as stiffness and damping performance, in both stowed and deployed configurations that cannot be achieved with the typical current state-of-the-art solar panel design strategies.
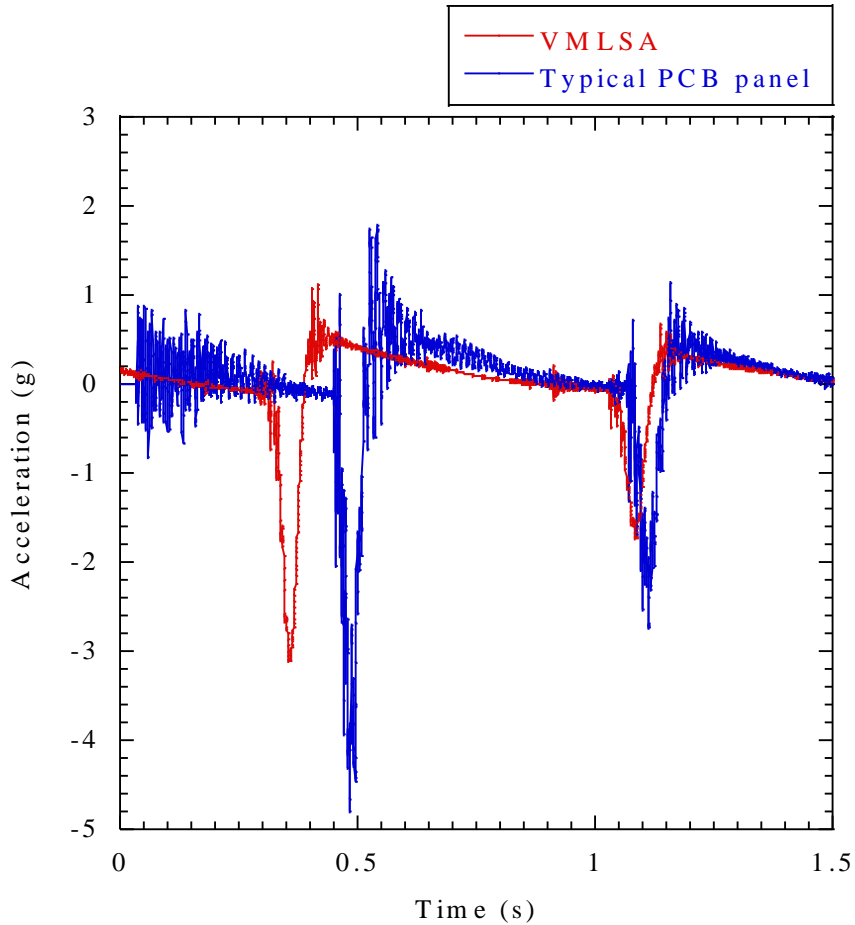
Fig. 63 Time Histories of the Free-vibration Tests of Solar Panels in Deployed Configuration.
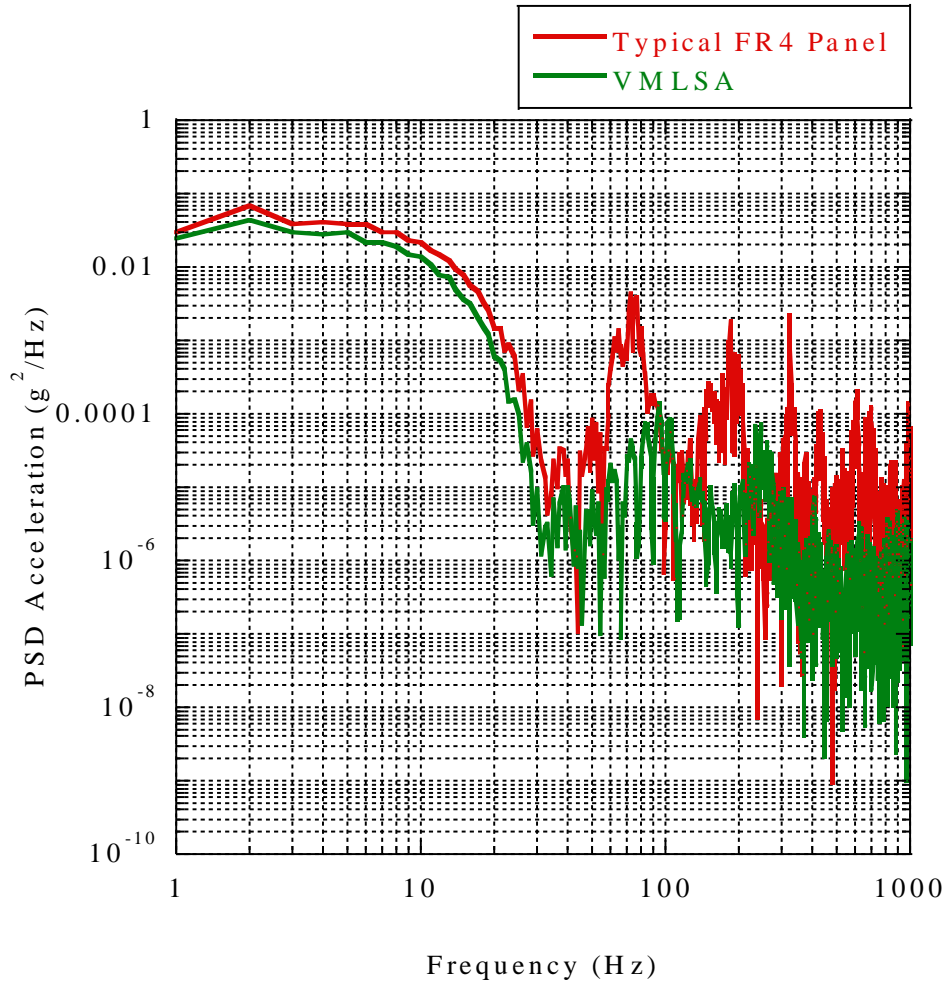
Fig. 64 The PSD Acceleration Responses of the Solar Panels in Deployed
Configuration.
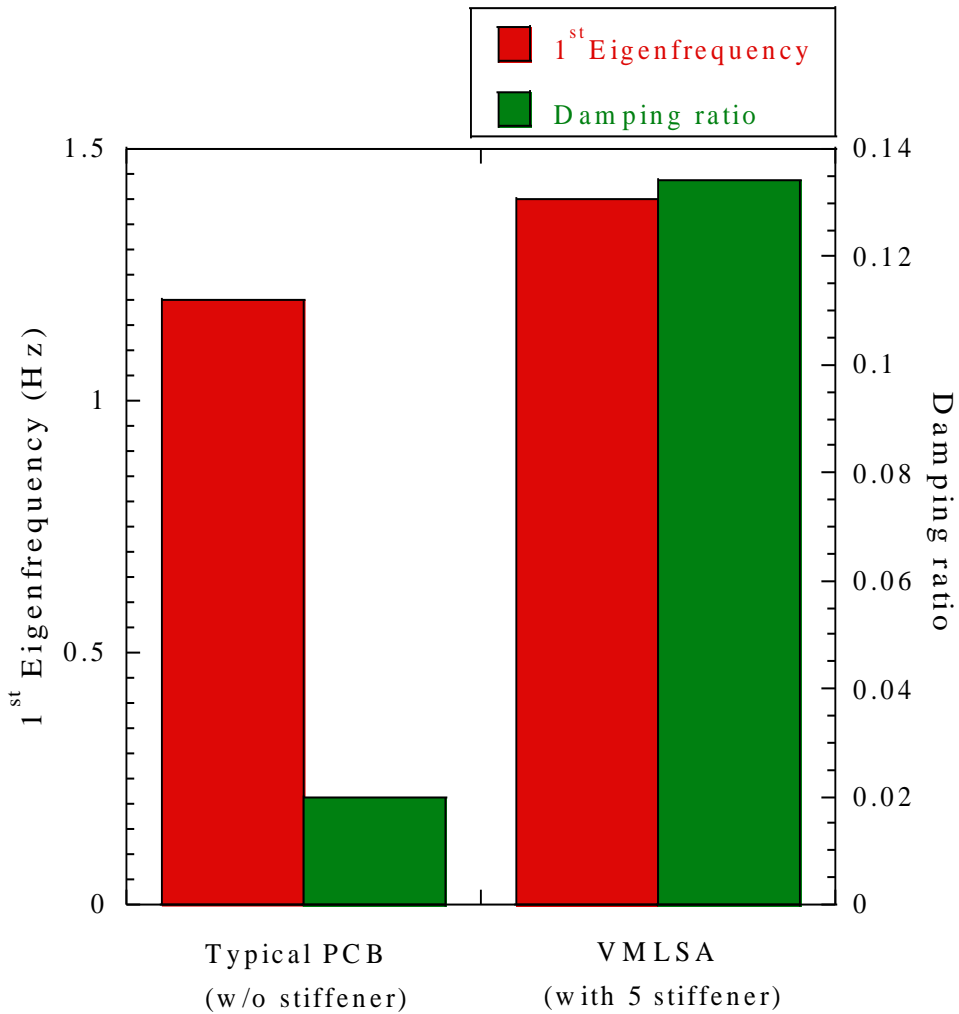
Fig. 65 Summarization of Basic Dynamic Characteristics of Solar Panels in Deployed Configuration.

3. Release Function Test

Functional tests are intended to verify the mechanical and electrical performance of components at the unit and subsystem levels, which are generally performed at ambient temperature and pressure conditions prior to environmental tests to establish a performance baseline. After the test article has been subjected to the required environments, additional functional test are conducted to determine the impact of the environments on the test article.

To validate the stable release function of the proposed three pogo pin-based deployment mechanism of the solar panel, release function tests were performed at ambient room temperature using the experimental test setup shown in Fig. 66. In order to minimize the gravitational effect during panel deployment, the solar panel module was installed horizontally such that the hinge's rotational axis was perpendicular to the test table. The qualification model of HRM, as shown in Fig. 22, was connected to a power supply for mechanism activation and to a data acquisition (DAQ) system for monitoring the input voltage and solar panel separation status signal during the test. The input voltage to the burn resistor for mechanism activation was set to 8 V, which can be sufficiently provided by the 6U CubeSat power system using commercial Li-ion batteries at an initial orbital ejection phase. In addition, an accelerometer was attached to the center of the solar panel to measure the panel acceleration during deployment.
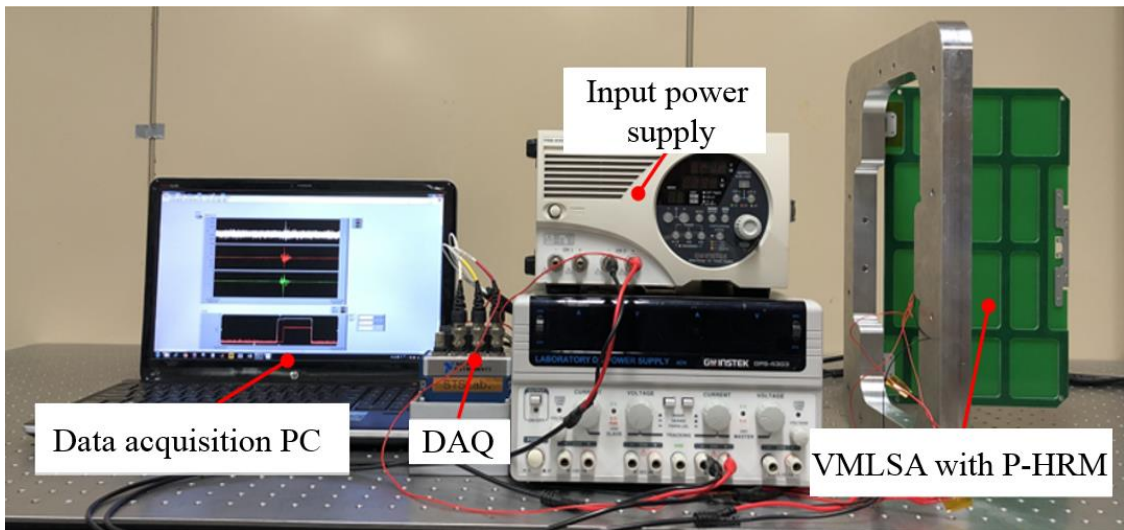
Fig. 66 Release Function Test Setup of the Qualification Model of STEP Cube Lab-II Solar Panel.

Figure 67 shows the time history of the input voltage, separation signal, and acceleration response of the solar panel measured during the test. The release status data were obtained through the output of buffer IC of the electrical circuit shown in the

electrical block diagram (in Fig. 23) through the DAQ channel; these data indicate that the solar panel was released within 0.72 s from the initiation of burn wire triggering. In addition, the acceleration response of the solar panel demonstrates that the full deployment of the panel took 1.58 s from the completion of the release action. This test result indicates that the proposed mechanism functioned well, and the solar panel deployment status was determined in accordance with the temporal electrical connection accomplished by the pogo pins as intended in the design.
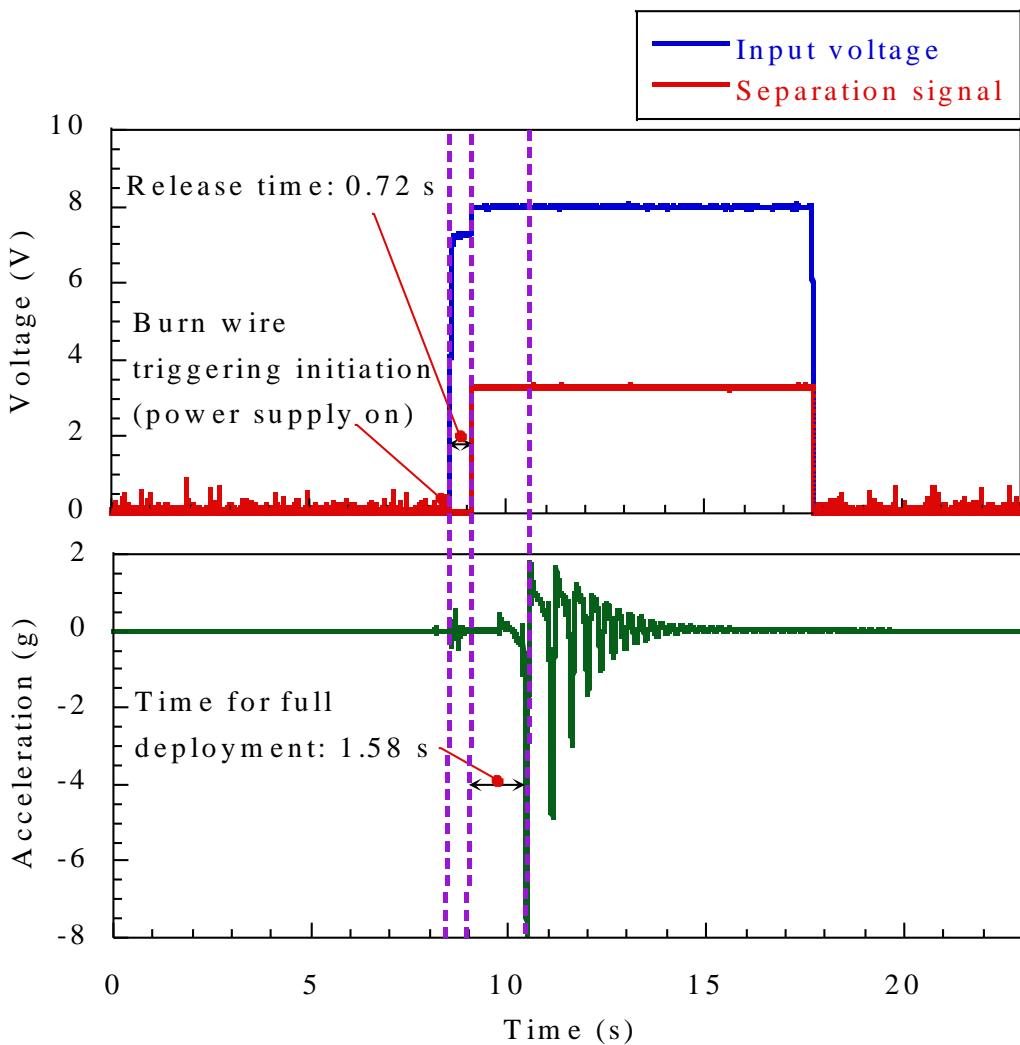
Fig. 67 Time Histories of the Input Voltage, Separation Signal, and Acceleration Response Obtained from Release Test of the VMLSA.

The several numbers of release function tests of the mechanism were required throughout the CubeSat development and testing phase. According to ECSS-E-ST-33-01C [83], for a minimum of 10 normal on-ground release tests, including run-in, acceptance testing, and one in-orbit release, the mechanism should be verified by performing at least 10 repeatability tests at ambient room temperature. Thus, to validate the repeatability of the proposed mechanism, repetitive release function tests were performed with the same test configuration, as shown in Fig. 66. The results plotted in Fig. 68 indicate that the mechanism was operating well with no failure on the burn resistor during 10 repetitive activations of the mechanism; however, the release time varied slightly owing to the workmanship to apply tension on the nylon wire knot during the tightening process. The average release time of the mechanism with one, two, and three number of wire windings during the 10 times of repetitive activation in each case was 0.77 s, 0.89 s, and 1.1 s, respectively. These results indicate that the mechanism assured sufficient repeatability for use in CubeSat applications. Furthermore, Park et al. [32] performed the release function test of solar panel as functions of thickness of nylon wire within the qualification temperature range of nylon wire of -40 $^{\circ}$C to +60 $^{\circ}$C. The release time of the panel was slightly higher at low temperatures as compared to the high-temperature environment due to the environmental effect on the variation of heating time of the burn resistor. However, the release time variation from 0 $^{\circ}$C to +60 $^{\circ}$C was nominal.
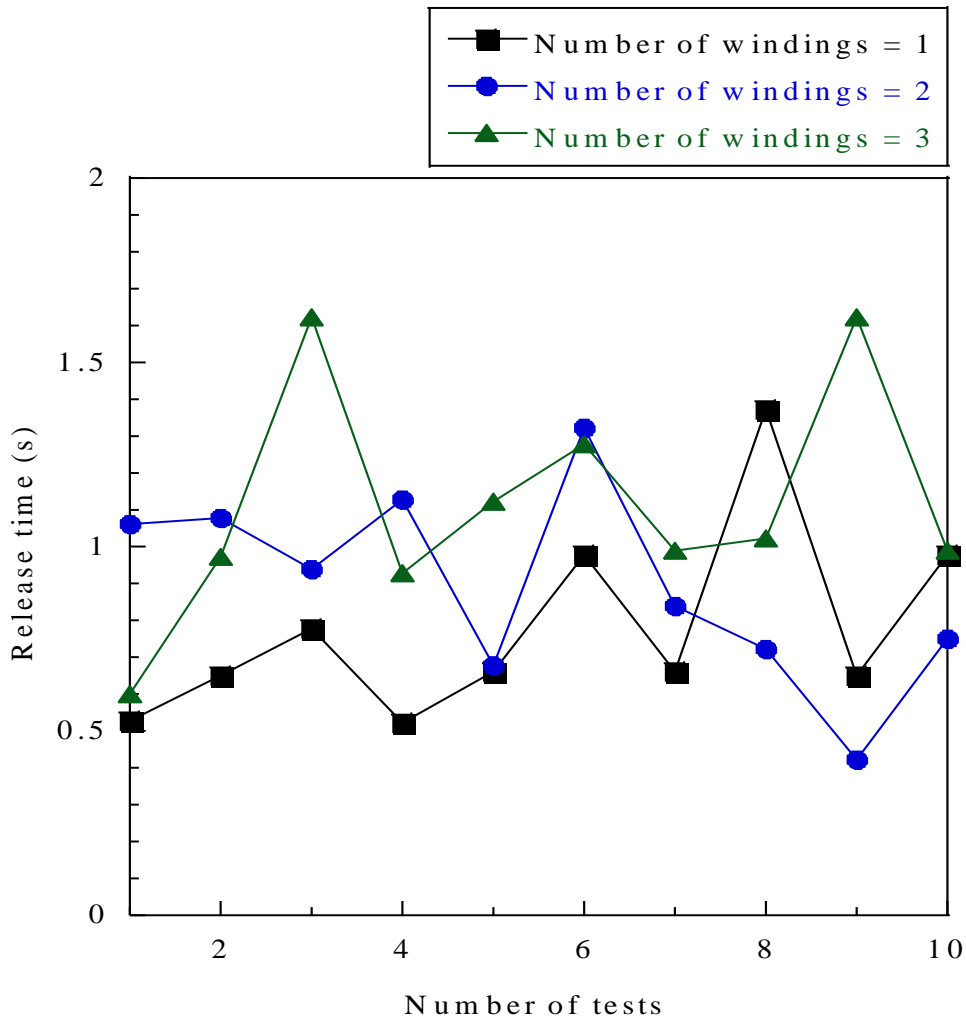
Fig. 68 Release Times of the Solar Panel during Repetitive Release Function Tests of
the Mechanism.

4. Radiation Test of the Electrical Components used in the P-HRM

In relative to the space radiation environment, the radiation hardness of electronic devices is defined according to two key aspects: cumulative effects and single event effects. The tolerance to the cumulative effects of ionizing radiation is one of the most important parameters to keep into account when selecting electrical components for space application. The TID test of the electrical interface PCB was conducted under the low-level energy spectrum of 1.17 to 1.33 MeV by Cobalt-60 (^{60}Co) radiation source at

the Korea Atomic Energy Research Institute for radiation hardness assurance of the P-HRM in a harsh space environment. Figure 69 shows the test set-up configuration of the electrical interface PCB at the TID test. The dose rate of the ^{60}Co was 1.67 krad per hour. The test duration was set to one hour because the deployment of the solar panel typically initiates within several minutes to an hour of orbital injection of CubeSat. The voltage on the pogo pin was continuously monitored during the test period in order to observe the electrical malfunction on the circuit due to the cumulative radiation exposure. Figure 70 shows the time history of the pogo pin voltage measure during the test. The result does not report any drastic variation of the pogo pin voltage while the electrical interface PCB was exposed to the 1 hr cumulative radiation dose. The slight fluctuation of voltage is owing to the noise at the DAQ channel, which was also observed in the solar panel release function tests performed in the ambient room environment.

However, for low earth orbit, the TID exposure can range from 4 krad(Si)/yr to 40 krad(Si)/yr for effective shielding thicknesses of 10 mils of aluminum [129]. The MicroMAS system is designed for a one-year mission in LEO with a nominal orbit of 402 x 424 km and 51.6 degree inclination. Based on estimates from the SPENVIS tool, the expected mission dose is approximately 1.2 krad(Si) [130]. Furthermore, the HiREV [13] 6U CubeSat with the sun-synchronous orbit of 500 km has radiation shields of 1 mm thickness. In this design, the total ionizing dose (TID) of the internal subsystem is approximately 9.2 krad analyzed by SHIELDOSE-2 in SPENVIS. The estimated analytical total dose for the STEP Cube Lab-II is 10 krad. Thus, an additional TID test of the mechanism is required at a system level to guarantee radiation hardness of the P-HRM under cumulative exposure over the mission life of CubeSat.
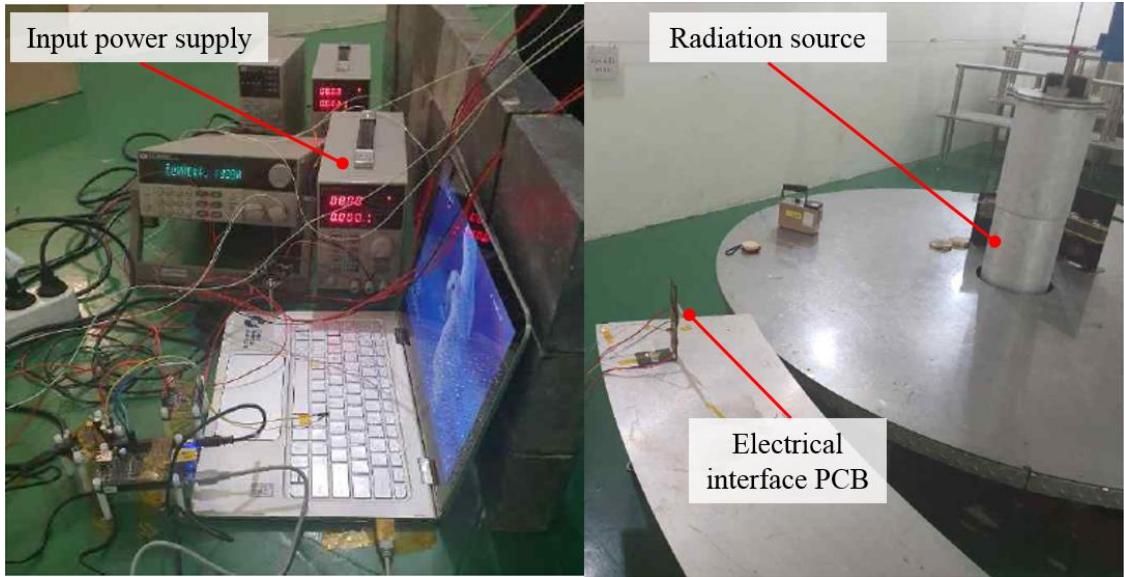
Fig. 69 The TID Test Set-up Configuration of Electrical Interface PCB.
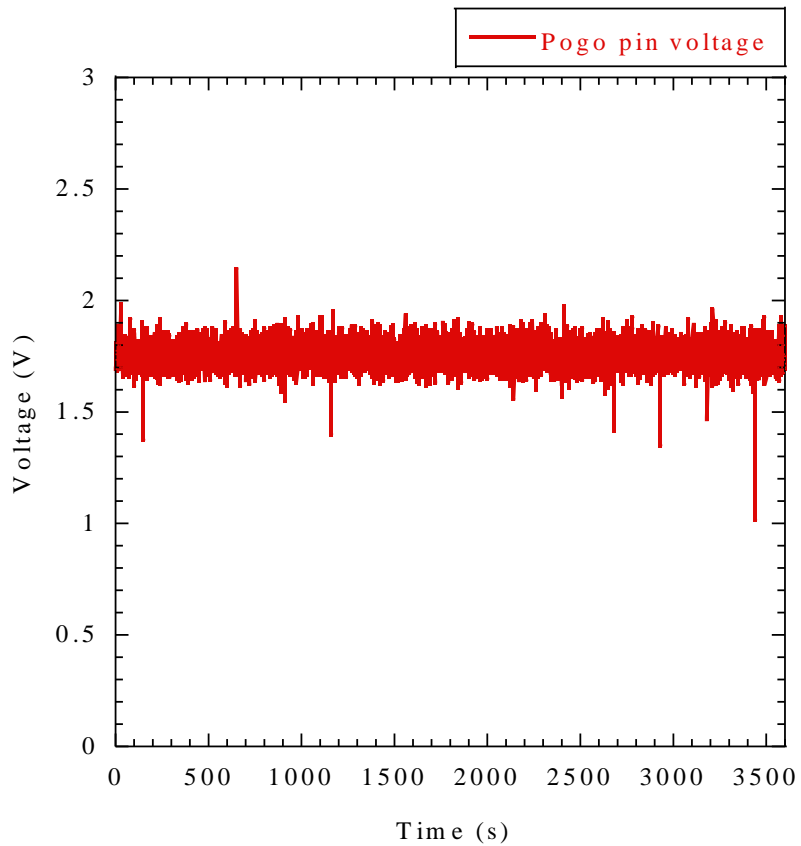
Fig. 70 Time History of the Pogo Pin Voltage during the TID Test.

Furthermore, the SEE test of the P-HRM PCB was conducted at the Proton Accelerator Research Center in Gyeongju, South Korea. Figure 71 shows the test set-up configuration of the electrical interface PCB during the SEE test. The test specimen was subjected to the conditions of 5 kRad with a high-level energy spectrum of 100 MeV. The current at the pogo pin is measured during the test. Figure 72 shows the time history of the pogo pin current obtained in the SEE test. The steadiness of the current reveals that no SEE event occurred even though the PCB was exposed to the harsh radiation environment. After finishing the radiation tests, the solar panel deployment test is carried out with the same electrical interface PCB to verify the functional performance of the electrical system of P-HRM. The solar panel was successfully deployed which validates the radiation hardness of electronic components used in the P-HRM.
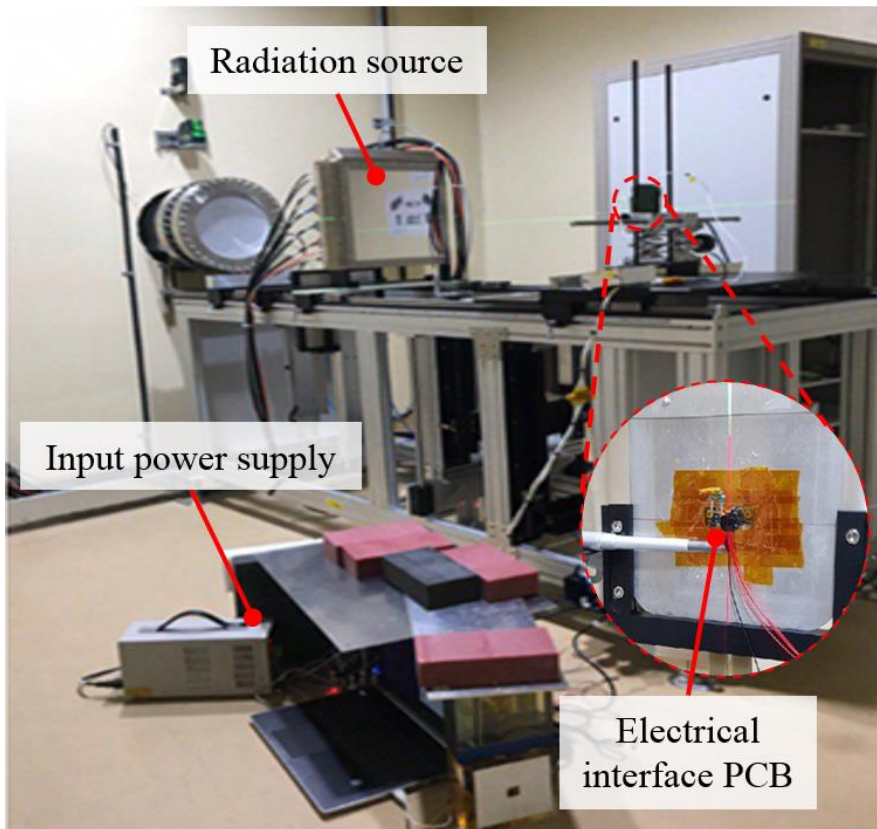
Fig. 71 The SEE Test Set-up Configuration of Electrical Interface PCB.
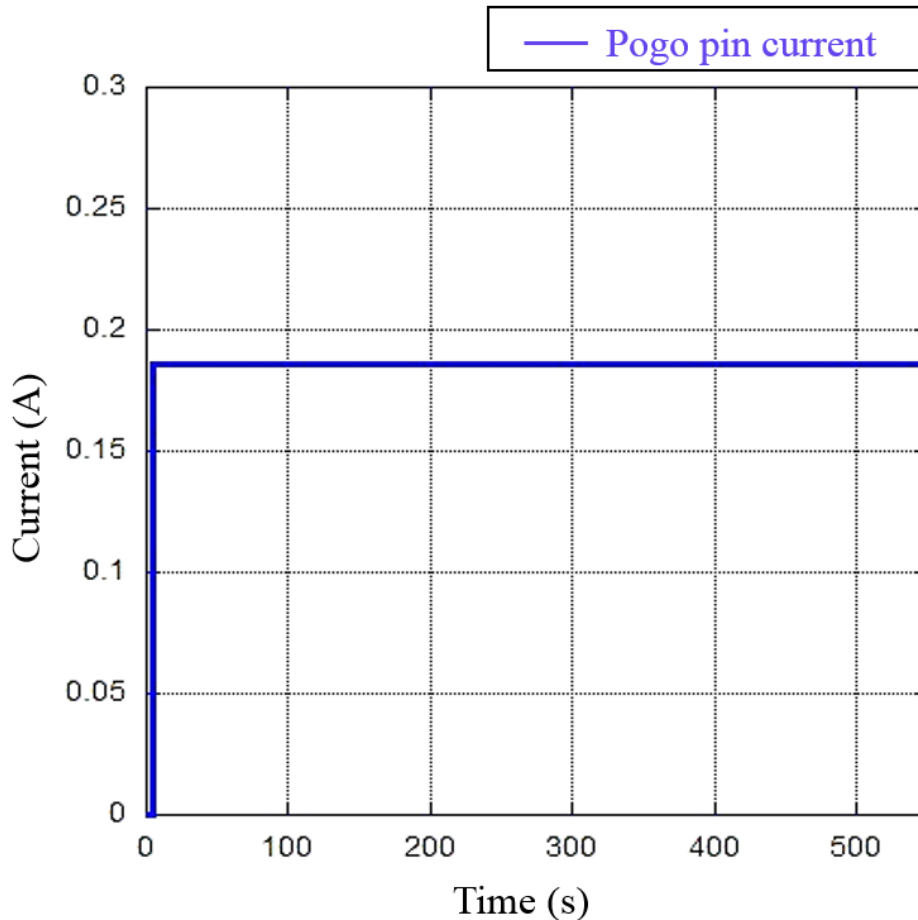
Fig. 72 Time History of the Pogo Pin Current during the SEE Test.

5. Launch Vibration Test

To verify the structural safety and damping performance of the qualification model of the solar panel module in a launch environment, launch vibration tests, such as sine and random vibration tests, were performed under the qualification level of the launch load specified in Tables 16 and 17. The main objective of these tests was to verify the design effectiveness of the highly damped deployable solar panel module with a pogo pin-based burn wire cutting HRM to ensure the structural safety of the solar cells in the launch vibration loads. Figure 73 shows an example of a launch vibration test configuration of the qualification model of the solar panel module on the electrodynamic vibration shaker (J260/SA7M, IMV Corp.) along with the *z*-axis excitation, which is the

most critical axis as it induces the largest dynamic deflection of the solar panel. Accelerometers were attached to the test jig and shaker slip table to monitor the input vibration loads. The output acceleration responses of the solar panel were measured using an accelerometer attached near the center of the solar panel. The test was performed at an ambient room temperature of 20 ℃. The structural safety of the solar panel module was validated by comparing the variation in the 1st eigenfrequencies of the panel, which were obtained through low-level sine sweep (LLSS) tests performed before and after each vibration test. In order to judge the structural safety of the specimen under the launch load, the 1st eigenfrequency variation in the LLSS should be less than 5%. After completing all the vibration tests, the release function test was performed on the solar panel to evaluate the reliability of the mechanism.
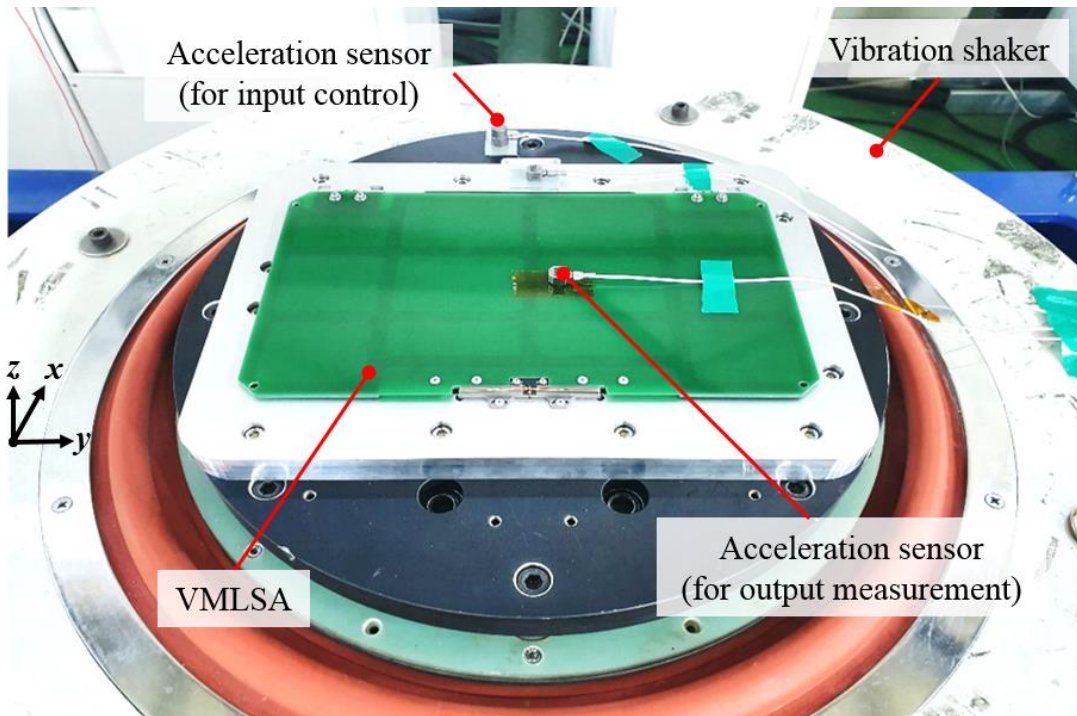
Fig. 73 Launch Vibration Test Setup Configuration of the Qualification Model of the Solar Panel Module.

A modal survey test was performed before and after each vibration test to verify the

structural safety of the solar panel module. A low-level sinusoidal vibration excitation with an amplitude of 0.5 g was applied to the solar panel module. Figure 74 shows the *z*-axis low-level sine sweep response of the solar panels in the *z*-axis excitation performed before the full level vibration tests that determine the natural frequency of the panel. Moreover, that also helps to check natural frequency shift before and after the full-level vibration tests of the panel for the test result evaluation. The results shows that the first eigenfrequency of the VMLSA along the *z*-axis was 75.0 Hz, which is 1.53 times higher than that of the typical PCB panel. However, the VMLSA first eigenfrequency is 1.25 times lower value compared with the simulation analysis result of 94.4 Hz. This is because of the mechanical holding constraint of the solar panel by the nylon wire was simply modelled by RBE2 rigid body element in the analysis that provided a much stiffer constraint compared to the actual boundary condition applied by nylon wire winding knot. Additionally, the presence of backlash in the torsional hinges also contributed for the reduction of natural frequency of the solar panel module compared with the simulated result.
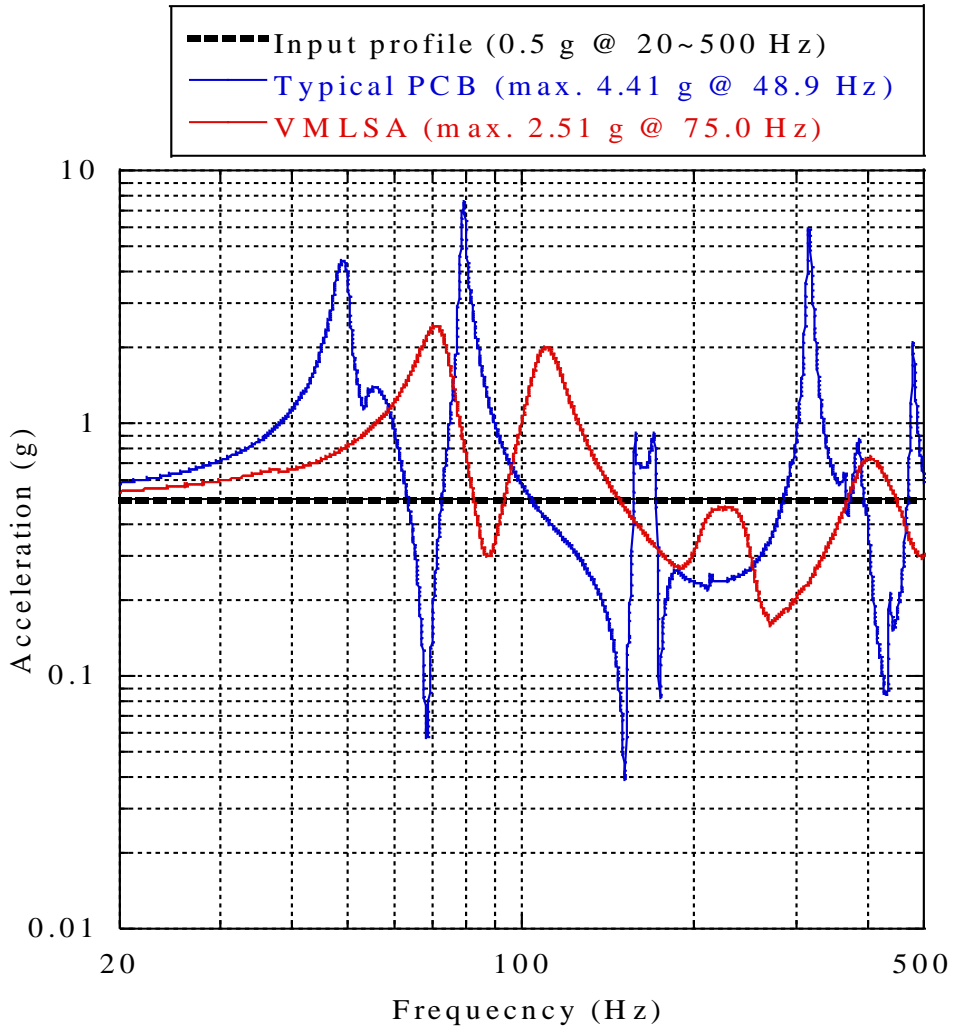
Fig. 74 Low-level Sine Sweep Results in the *z*-axis Excitation.

The full-level sine vibration test results of the solar panel module along the *x*-, *y*-, and *z*-axis excitations are presented in Fig. 75. In the figure, only the corresponding axis vibration responses of the solar panel with the excitation axis are presented, as the corresponding axis has a larger dynamic response than the other axis of the panel. In the sine vibration tests, the qualification-level input loads specified in Table 16 were applied to the solar panel along each axis; however, the *z*-axis was the most critical axis because it induced the largest dynamic deflection of the solar panel. With respect to the maximum 2.5 g sine vibration input load in each axis, the maximum acceleration

responses of the corresponding *x*-, *y*-, and *z*-axes with the excitation axes within the input frequency range were 2.5, 2.5, and 10.26 g, respectively. The solar panel's maximum resonance response of 10.26 g was observed at 75 Hz on the *z*-axis during the same axis excitation of the panel.
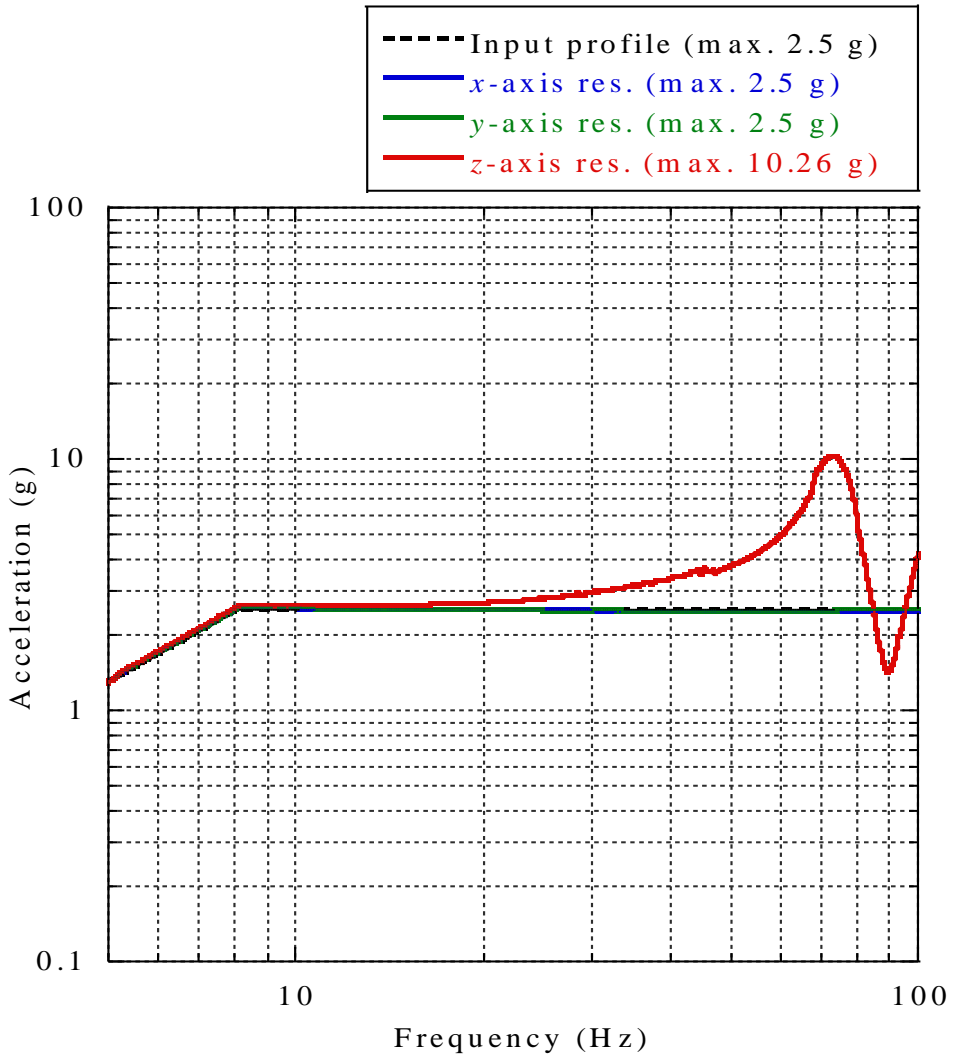
Fig. 75 Sinusoidal Vibration test Results of Solar Panel's Corresponding Axis in the *x*-, *y*-, and *z*-axis Excitations.

Figure 76 shows the random vibration test results of the solar panel along each

excitation axis with respect to the input level of 14.1 G_{rms}. The corresponding axis G_{rms} values of the solar panel along the *x-, y-,* and *z*-axis excitations, calculated from PSD acceleration profiles, were 16.57, 16.36, and 13.51, respectively. The G_{rms} of the solar panel in the *z*-axis was lower by a factor of 1.04 than that of the input level.
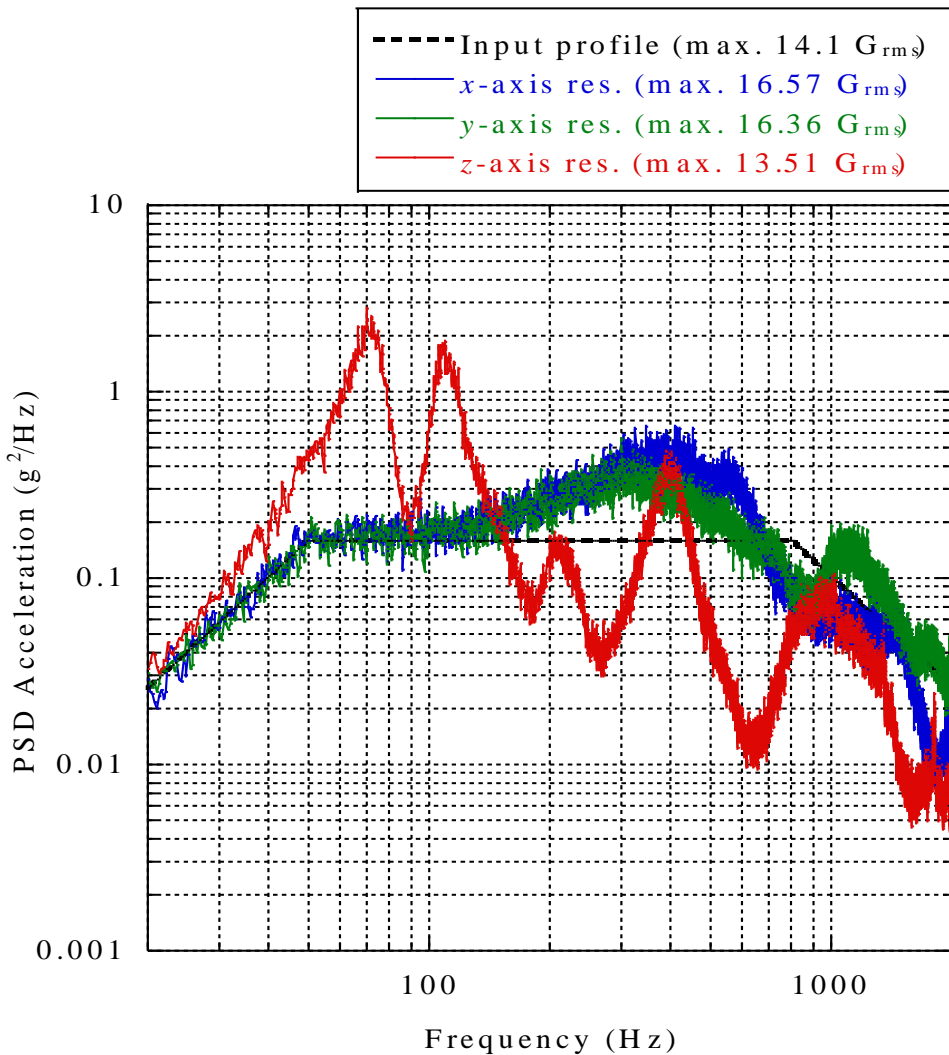
Fig. 76 Random Vibration Test Results of Solar Panel's Corresponding Axis in the *x*-, *y*-, and *z*-axis Excitations.

Figure 77 shows the representative modal survey results of the acceleration response

measured at the solar panel along *z*-axis excitation. The result obtained prior to the full level vibration tests indicate that the first eigenfrequency of the panel was 75.0 Hz along the *z*-axis, which, after the sine and random vibration tests appeared at 74.3 Hz and 70.79 Hz, respectively. The frequency-shifted after exposed in the full level severe launch vibration tests is minimal.
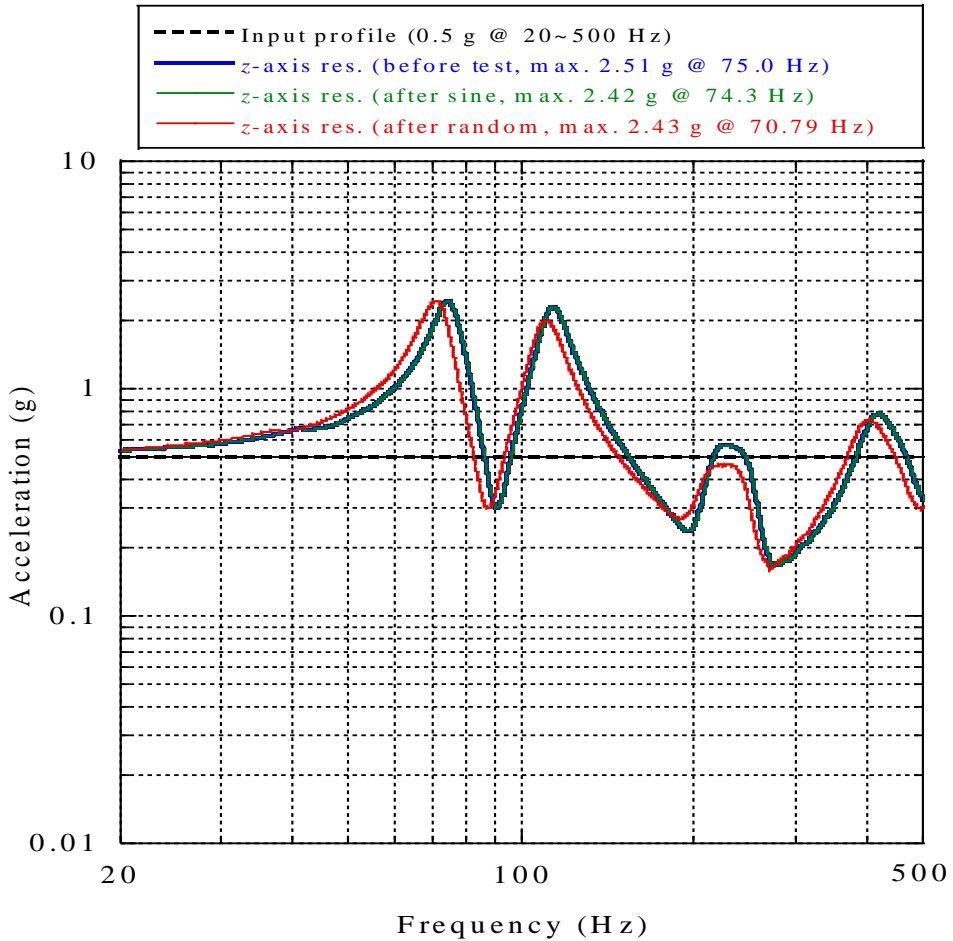
Fig. 77 Low-level Sine Sweep Results in the *z*-axis Excitation Before and After vibration Tests.

Table 32 summarizes the 1st eigenfrequencies of the solar panel in each axis obtained through the LLSS tests performed before and after each vibration test. The tabulated result shows that the 1st eigenfrequency shift was within 4.85% throughout the

test sequences of the panel, which was within the 5% criterion. In addition, after the launch vibration tests have been completed, the solar panel was visually inspected, and no crack, dissociation, or plastic deformation were observed on the laminated stiffeners. These tests and inspection results indicate that the structural safety of the proposed solar panel module was successfully validated in the qualification-level launch environment tests.

Table 32 LLSS Test Results of the Solar Panels Before and After Full Level Vibration Tests.

Test	Axis	Status	1st Eigenfrequency (Hz)	Difference (%)
Sine Vibration	x	Before	835.2	0.19
		After	833.6	
	y	Before	602.4	0
		After	602.4	
	z	Before	75.0	0.93
		After	74.3	
Random Vibration	x	Before	833.6	0.19
		After	832.0	
	y	Before	602.4	0
		After	602.4	
	z	Before	74.3	4.85
		After	70.7	

6. Comparison between Simulation and Experimental Dynamic Analysis Results

The relationship between simulation and experimental analysis results has been performed. Table 33 presents the solar panels' dynamic response results in simulation and experimental tests. Figure 78 shows the analyzed and measured PSD acceleration response of the VMLSA. The analyzed G_{rms} responses and relative displacement values of the VMLSA correspond with the measured ones with only a maximum difference of 1.31 and 0.02 mm, respectively. The relative percentage difference of G_{rms} values is 9.6 %. The noticeable difference between the 1st eigenfrequency of VMLSA in simulation and experimental results might be owing to the hinge backlash in the shaft and the temperature condition of the test facilities. In the simulation analysis, the hinge shaft was simulated by making RBE3 without constraint on the rotational axis and CBAR elements. The backlash between the hinge brackets and hinge shaft was not considered in the simulation analysis. Furthermore, some differences in the higher frequencies are observed, although it does not produce a problem for analysis results since the 1st peak response is dominant in terms of the structural safety of the solar panel. Thus, the FEM simulation analysis and experimental tests results are reliable to predict or approximation a structural safety of the solar panel.

Table 33 Solar Panels Dynamic Response Results in Simulation and Experiment Tests.

Case		Mass (g)	Dynamic Response Result		
			1st Eigenfrequency (Hz)	G_{rms}	Relative Displacement (mm)
Typical FR4 Panel	Simulation	208	52.69	23.97	0.78
	Experimental		48.90	23.21	0.71
Relative Error			3.79	0.76	0.07
VMLSA	Simulation	306.5	83.83	12.20	0.14
	Experimental		75.00	13.51	0.12
Relative Error			8.83	1.31	0.02
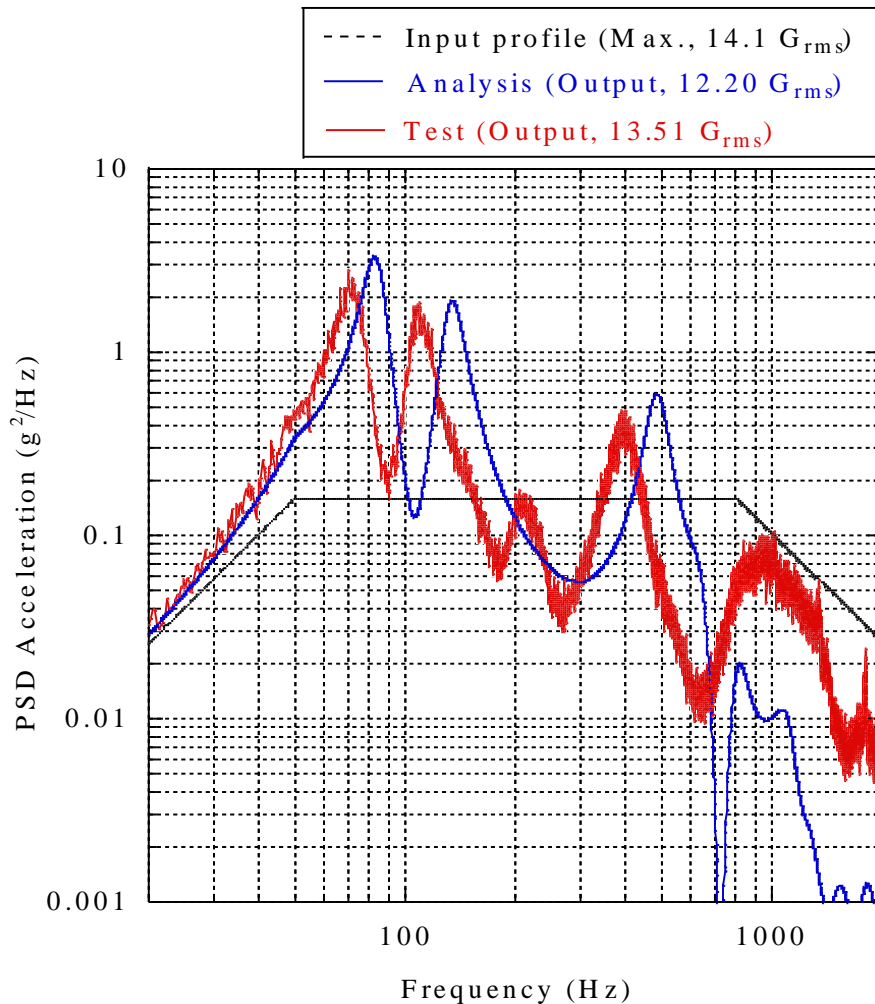
Fig. 78 Analyzed and Measured PSD Acceleration Response of the VMLSA.

7. Thermal Vacuum Test

Thermal environment test typically include thermal cycling and thermal vacuum tests at the unit level. Thermal cycling and thermal vacuum tests are intended to verify performance of the test article in the expected temperature and vacuum environments as well as to stress components to detect workmanship and materials deficiencies. In this work, the TV test of the solar panel module is conducted in a ϕ1m TV chamber to validate the structural safety of the solar panel and the functionality of the pogo pin-based mechanism under a space-simulated TV environment. Figure 79 shows the TV test setup of the solar panel module. Thermocouples were attached to the solar panel and

mechanism to measure the temperature of the specimen during the test although it is not shown in the figure. A thermocouple mounted on the electrical interface PCB of the HRM was considered as the temperature reference point (TRP) to assess the stabilized target temperature. The solar panel module was exposed to six thermal cycles, with the qualification temperature ranging from -40 ℃ to 60 ℃ under a chamber pressure of less than 10^{-5} torr. The target temperature of the TRP on the specimen was achieved by controlling the shroud temperature of the TV chamber at a rate of 1 ℃ per hour, and the dwell time at the hot and cold plateaus was set to 1 h.
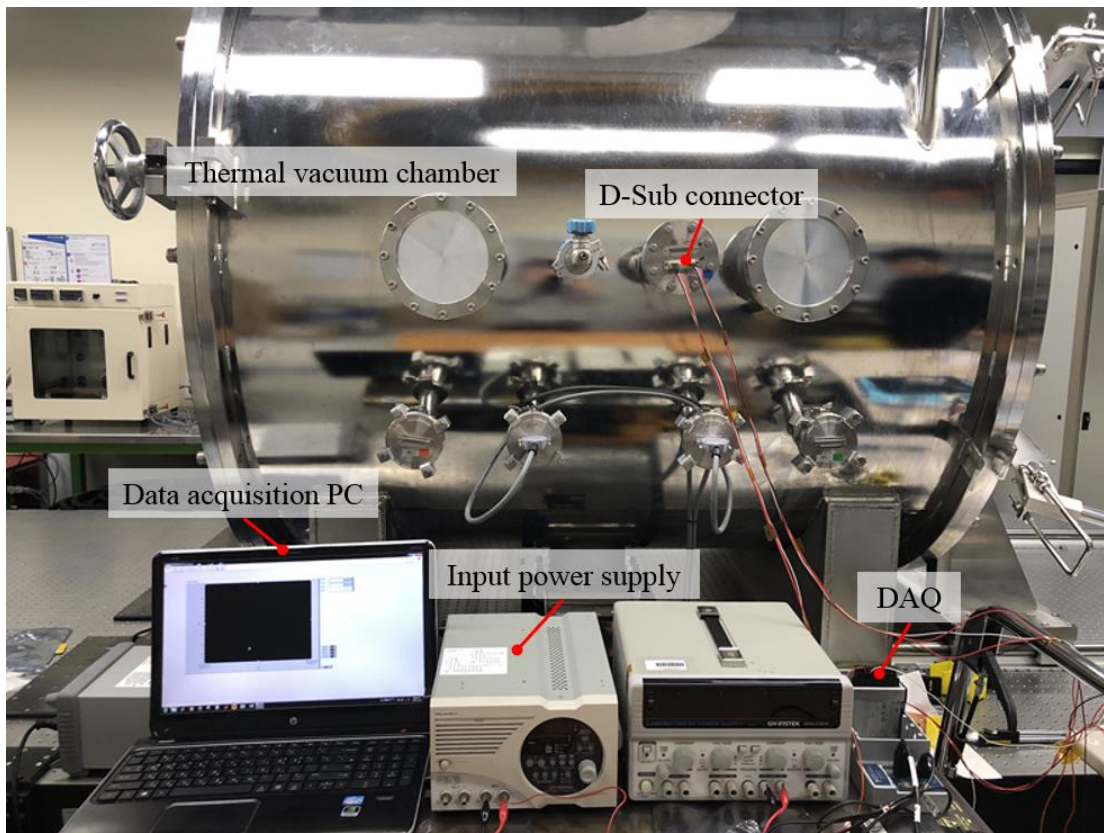
Fig. 79 TV Test Setup Configuration of the Solar Panel Module.

Figure 80 shows the temperature profiles of the solar panel module obtained from the TV cycling tests. The state of health (SOH) check of the solar panel and the mechanism were conducted through the visual inspection at the dwell time of all the hot

and cold soak phases. Moreover, the release function test of the mechanism was performed at -20 ℃ in the 3rd cold soak phase because it was the worst condition for the mechanism activation at the initial orbital ejection period of the satellite. The solar panel was successfully released in 5.20 s without any anomalies after triggering input voltage was applied; however, the release time was substantially higher than that measured under ambient room conditions owing to the variation in the heating time of the burn resistor for cutting the nylon wire. Additionally, the electrical power dissipation in the input power supply of the wire to the mechanism and the time delay of the deployment relay signal to the DAQ system in an extremely cold environment under the TV chamber are also factors in increasing the release time [131]. As the deployment of the solar panel is typically initiated after several minutes to hours of orbital ejection of the CubeSat, the onboard electrical power system of CubeSats has sufficient power to release the solar panel. As shown in the time history of the temperature profile, the first three cycles of the TV test were performed in the temperature range of -20 ℃ to 60 ℃. After verifying the release function test of the mechanism, the remaining test cycles were performed in the qualification temperature range of the solar panel.
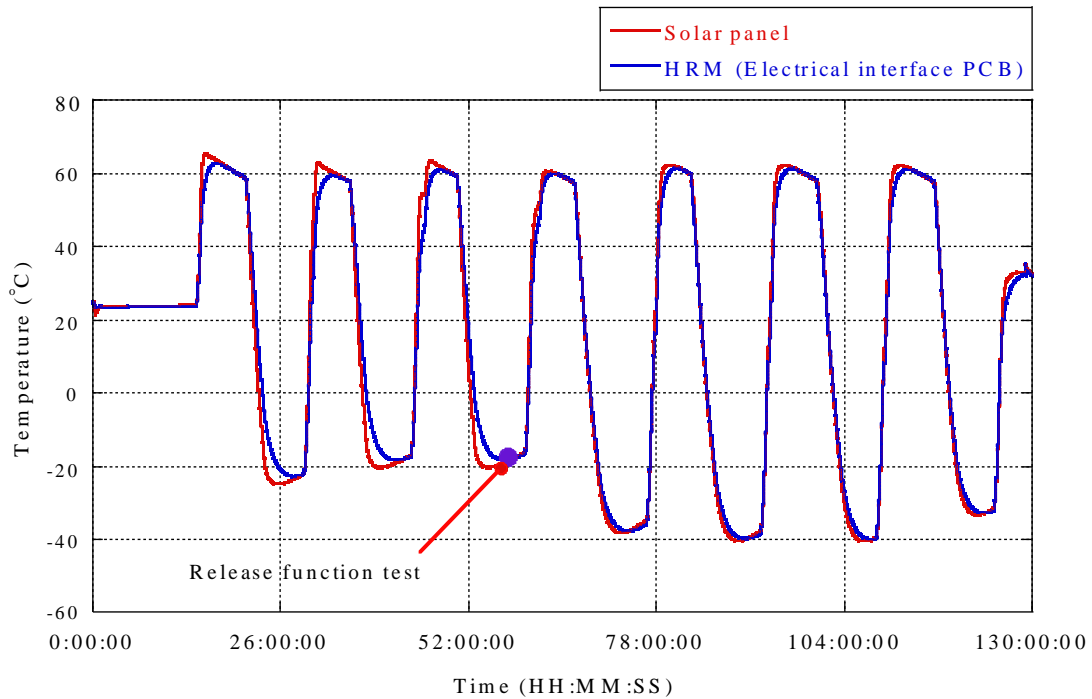
Fig. 80 Time Histories of the Temperature Profiles of the Solar Panel Module in the TV Test.

After the completion of the TV test, the release function test of the mechanism was carried out at ambient room temperature conditions to validate the mechanism's release operation after exposure to the thermal stress in a space simulated TV environment. The corresponding release function test results are presented in Fig. 81. The results obtained before and after the vibration tests are plotted in the figure to compare the release time. The solar panel was successfully released within 1.5 s after the burn wire was triggered in the mechanism; however, this value was higher by factors of 2.08 and 1.64 compared with those measured before and after the vibration tests, respectively. In addition, after all the launch vibration and TV environments tests were completed, the solar panel was inspected microscopically. Figures 82 (a) and (b) show the representative optical microphotographs of the sidereal edge of the solar panel in the pre- and post-TV tests. The inspection results did not indicate any slip, dissociation or plastic deformation in the laminated layers.

- 152 -
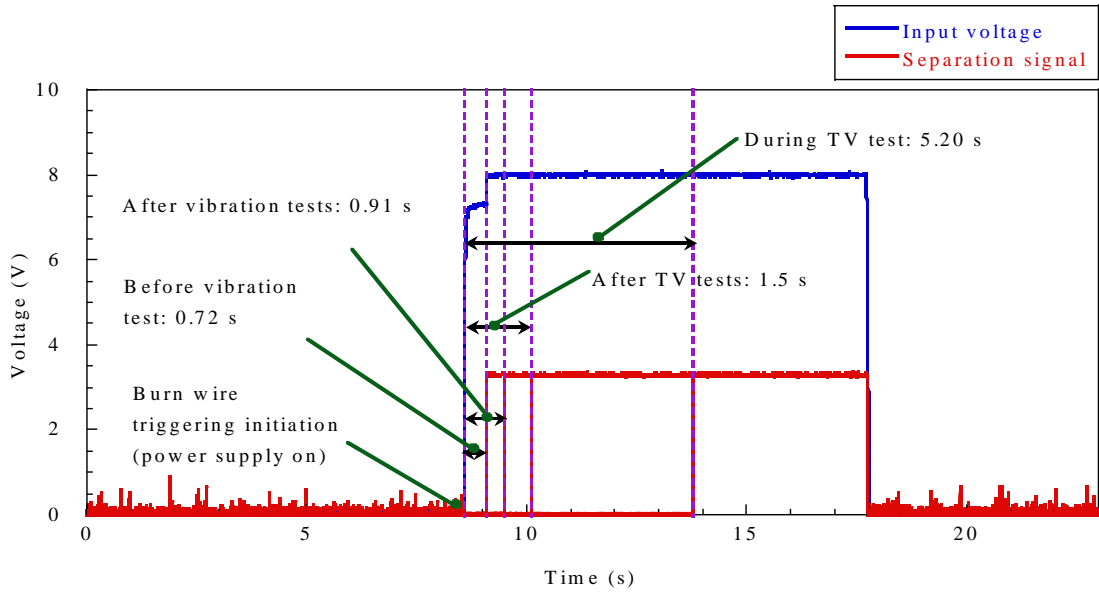
Fig. 81 Time Histories of Release Time of the Mechanism Before and After Launch
Vibration and TV Tests.

(a)   (b)
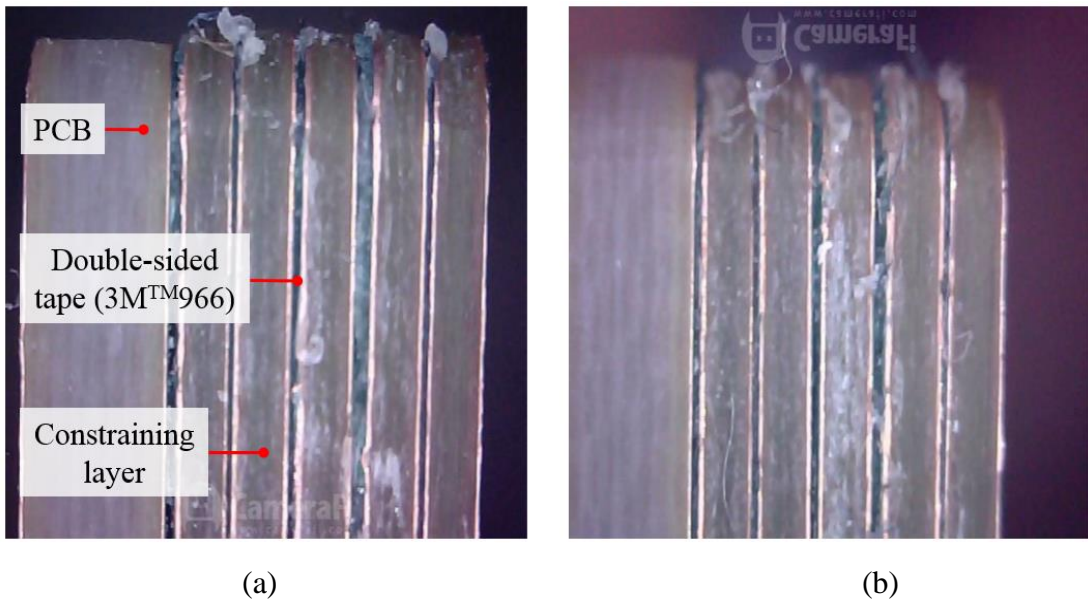
Fig. 82 Representative Optical Microphotographs of the Solar Panel Side Edge: (a)
Before TV Environment Test and (b) After TV Environment Test.

8. Summary of Experimental Validation Test Results

The release time and structural safety results of the solar panel module is summarize in Table 34 for the comparison of the performance at each event. The pass and fail criteria for determining the structural safety of the laminated stiffeners were the absence and presence of delamination or cracks, respectively. These qualification-level launch vibration and TV environment tests and inspection results validate the structural safety of the proposed solar panel module employing the three pogo pin-based mechanism. The solar panel deployment tests validate the reliable release action of the mechanism during an initial orbital ejection of the CubeSat. In addition, the radiation test results of the electrical components used in the electrical interface PCB of P-HRM indicates the nominal behaviour under the TID and SEE test that ensured the radiation hardness in the space environment.

Table 34 Summary of Release Time and Structural Safety Results of the Solar Panel Module at Each Event.

Test Event	Input Power (V)	Release Time (s)	Solar Panel Release (Pass/Fail)	Structural Safety of the Solar Panel Module	
				Mechanism (Pass/Fail)	Stiffeners (Pass/Fail)
Before Vibration	8	0.72	P	P	P
After Vibration	8	0.91	P	P	P
During TV Test	8	5.20	P	P	P
After TV Test	8	1.5	P	P	P

Furthermore, the relative maximum dynamic displacement at the center of the solar panel was 0.12 mm during the *z*-direction excitation under a random vibration load, estimated from the three-sigma value of the G_{rms} response. The maximum dynamic displacement of the proposed solar panel module reduced significantly by a factor of 5.9

compared with that of the typical solar panel without a stiffener. This is owing to the higher vibration attenuation resulted from the shear deformation of the viscous layers of the acrylic tapes. Thus, a highly damped deployable solar panel employing constrained layer damping with viscoelastic acrylic tapes is effective for achieving the design goals of launch load attenuation and minimization of the dynamic deflection of the 6U sized solar panel at the module level.

VI. Conclusion and Future Research

A. Conclusion

In this study, the design methodology for structural design of a highly damped deployable solar panel module was evaluated under simulated launch vibration and thermal environments to demonstrate the effectiveness of the design. A qualification model of a highly damped PCB-based deployable solar panel module employing multi-layered stiffeners with viscoelastic acrylic tapes combined with a three pogo pin-based burn wire triggering release mechanism was fabricated and experimentally evaluated for the application in STEP Cube Lab-II. The proposed solar panel is advantageous to assure structural safety of the solar cells under launch vibration environments by attenuating panel dynamic acceleration and deflection through shear deformation characteristics of adhesive tapes. The optimized design of three pogo pin-based burn wire triggering mechanism has many advantages, including increased loading capability, multiplane constraints, and reliable release action that can overcome the limitations of conventional burn wire cutting release mechanisms. The power budget of CubeSat was calculated based on the system requirement according to the mission operations and the energy balance analysis to satisfy the onboard power demand of subsystems and payloads for the mission performance. The power analysis results helped to assess the size of the solar panel as the surface area has a linear relationship to the CubeSat's on-board power generation. The structural safety of the solar panel module in launch vibration loads is estimated by modal and random vibration analysis of the design through the FEM. In addition, the calculated MoS of the nylon wire for the panel holding constraint indicates that at least double wire winding is required for securely stowing the panel in launch loads. The thermal design analysis of the solar panel was performed to determine the most feasible thermal design for minimization of thermal distortion of the panel in extreme in-orbit thermal environments. The results revealed that the thermal design

based on the black anodizing surface finish or kapton tape is effective for minimization of thermal gradient on the solar panel.

The basic dynamic characteristics of the solar panel were demonstrated by free-vibration tests under various temperature conditions. The functionality of the mechanism was verified through the solar panel deployment tests in ambient room temperature. Additionally, the TID and SEE radiation tests of the electrical interface PCB assured the radiation hardness of the mechanism. The launch vibration results of the solar panel demonstrated that the dynamic displacement along the z-axis was significantly reduced by a factor of 5.9 compared to the typical solar panel without employing stiffener. After completion of all the vibration and TV tests, the visual inspection of the solar panel does not report any crack, dissociation, and plastic deformation on the stiffeners. The release function test of the solar panel performed after launch vibration and TV tests showed nominal function of the mechanism. The test results indicated that the proposed high damping deployable solar panel module is effectively qualified for use in the CubeSats application. Thus, the use of a single HRM makes it possible to ensure the structural safety of solar cells without reducing the available area of solar cell accommodation within the minimal increased mass of the solar panel module. In addition, the solar panel design suggested in this study could also have a considerable advantage for the rapid attenuation of residual vibration on deployed solar panels after the slew maneuver of satellite that could minimize the performance degradation of the future space missions, where rapid slew maneuvers are required for the acquisition of a target point.

B. Future Research

Future research as an extension of the works presented in this dissertation that seem most worthwhile in improving viscoelastic vibration damping strategies and its applicability in nano-class satellites are described as follows:

(1) Applicability in small satellites

The work presented in this dissertation is mainly focused on design methodology validation of a highly damped deployable solar panel module combined with pogo pin-based burn wire triggering release mechanism under launch vibration and thermal environments for the application of nano-class satellites especially for CubeSat. Based on the finding of this research, the applicability investigation of this strategy on the deployable solar panels of small satellites for ensuring the structural safety of the solar cells under launch vibration would be one potential future work. If this technology is applicable for larger configurations of the small satellites' deployable solar panels, the use of a single HRM makes it possible to ensure the structural safety of solar cells without reducing the available area of solar cell accommodation, and significantly decrease the solar panel development cost. Additionally, the relationship between the stiffness of the solar panel module with the applied tension on the nylon wire knot could also be an interesting topic as future research.

(2) Effectiveness for in-orbit vibration attenuation

In recent years, the complexity of CubeSat missions has been increasing steadily as the platform capability has drastically improved. Missions involving high-accuracy fine-pointing stability for Earth observation and interplanetary explorations are no longer out of the reach of CubeSats. The in-orbit low and medium frequency vibration on the deployable solar panels induced by satellite attitude maneuver is also critical for some on-board equipment and sensors because it causes rigid body motion in the satellite, which could degrade pointing stability. This work shows that the chattering vibration on the solar panel deployed configuration can also be substantially attenuate with the application of viscoelastic acrylic tape. In order to verify the effectiveness of the constrained layer damping with a viscoelastic material technique for rapid attenuation of residual vibration on the panel at the end of the slew maneuver or even eliminate micro-jitter on the satellite, a comprehensive experimental test in the vacuum environment shall be carried out in the future.

(3) Aging test for life cycle approximation

The life cycle testing result of the viscoelastic material used in the Hubble space telescope solar array damper indicated that the viscoelastic bond actually developed further over time, suggesting that the damping of the constraint layer could work as predicted over its life in orbit [70]. This statistic was also stated in the 3M^{TM} adhesive tape datasheet: the bond strength of adhesive tape increases as a function of time and temperature [69]. In this study, the solar panel was verified in the simulated launch and in-orbit environments at the qualification level, although the aging test of the viscoelastic material for life cycle approximation, a variance in the stiffness of the panel, and damping efficiency over time can also be seen as potential additional assurance works.

【Reference】

1) H. J. Kramer and A. P. Cracknell, "An Overview of Small Satellites in Remote Sensing", International Journal of Remote Sensing, Vol. 29, pp. 4285-4337, 2008.

2) T. Arvidson, S. Goward, J. Gasch and D. Williams, "Landsat-7 Long-term Acquisition Plan: Development and Validation", Photogrammetric Engineering and Remote Sensing, Vol. 72, pp. 1137-1146, 2006.

3) Y. Tanaka, H. Inoue and S. S. Holt, "The X-ray Astronomy Satellite ASCA", Publications of the Astronomical Society of Japan, Vol. 46, pp. 37-41, 1994.

4) P. G. Antreasian, D. T. Baird, J. S. Border et. al., "Mars Odyssey Orbit Determination During Interplanetary Cruise", Journal of Spacecraft and Rockets, Vol. 42, pp. 1-12, 2005.

5) C. R. O'Dell, "Creation of the Hubble Space Telescope", Experimental Astronomy, Vol. 25, pp. 261-272, 2009.

6) J. Puig-Suari, C. Turner and R. J. Twiggs, "CubeSat: The Development and Launch Support Infrastructure for Eighteen Different Satellite Customers on One Launch", Proceedings of the 15th Annual AIAA/USU Small Satellite Conference, Logan, Utah, USA, pp.1-5, 2001.

7) J. Puig-Suari, C. Turner and W. Ahlgren, "Development of the Standard CubeSat Deployer and a CubeSat Class PicoSatellite" Proceedings to the 2001 IEEE Aerospace Conference, USA, pp. 347-353, 2001.

8) J. Bouwmeester and J. Guo, "Survey of Worldwide Pico-and Nanosatellite Missions, Distributions and Subsystem Technology", Acta Astronautica, Vol. 67, pp. 854-862, 2010.

9) K. Woellert, P. Ehrenfreund, A. J. Ricco and H. Hertzfeld, "Cubesats: Cost-effective Science and Technology Platforms for Emerging and Developing Nations", Advances in Space Research, Vol. 47, pp. 663-684, 2011.

10) P. Ehrenfreund, A. J. Ricco, D. Squires et al., "The O/OREOS Mission-Astrobiology in Low Earth Orbit", Acta Astronautica, Vol. 93, pp. 501-508, 2014.

11) H. U. Oh and T. Y. Park, "Experimental Feasibility Study of Concentrating Photovoltaic Power System for CubeSat Applications", IEEE Transactions on Aerospace and Electronic Systems, Vol. 51, No. 3, pp. 1942-1949, 2015.

12) X. Li, Q. Schiller, L. Blum et al., "First Results from CSSWE CubeSat: Characteristics of Relativistic Electrons in the Near Earth Environment during the October 2012 Magnetic Storms", Journal of Geophysical Research: Space Physics, Vol. 118, No. 10, pp. 6489-6499, 2013.

13) D. H. Cho, W. S. Choi, M. K. Kim, J. H. Kim, E. Sim and H. D. Kim, "High-Resolution Image and Video CubeSat (HiREV): Development of Space Technology Test Platform Using a Low-cost CubeSat Platform", International Journal of Aerospace Engineering, Vol. 2019, pp. 1-17, 2019.

14) S. Wu, W. Chen, C. Cao, C. Zhang and Z. Mu, "A Multiple-CubeSat Constellation for Integrated Earth Observation and Marine/Air Traffic Monitoring", Advances in Space Research, Vol. 66, pp. 1-13, 2020.

15) S. Nag, J. L. Rios, D. Gerhardt and C. Pham, "CubeSat Constellation Design for Air Traffic Monitoring", Acta Astronautica, Vol. 128, pp. 180-193, 2016.

16) G. Santilli, C. Vendittozzi, C. Cappelletti, S. Battistini and P. Gessini, "CubeSat Constellations for Disaster Management in Remote Areas", Acta Astronautica, Vol. 145, pp. 11-17, 2018.

17) Nanosats Database, Constellations, Companies, Technologies, World's Largest Database of Nanosatellites, Over 2700 Nanosats and CubeSats, https://www.nanosats.eu/, Online, last accessed: 08,17,2020.

18) M. Komatsu and S. Nakasuka, "University of Tokyo Nano Satellite Project "PRISM", Trans. JSASS Space Tech. Japan, Vol. 7, pp. 19-24, 2009.

19) R. Funase, S. Ikari, R. Suzumoto, N. Sako, M. Sanada and S. Nakasuka, "On-orbit Operation Results of the World's First CubeSat XI-IV Lessons Learned

from Its Successful 15-years Space Flight", Proceedings to the 33rd Annual AIAA/USA Conference on Small Satellites, Logan, United State, pp. 1-8, 2019.

20) J. Schoolcraft, A. T. Klesh and T. Werne, "MarCO: Interplanetary Mission Development on a CubeSat Scale", Proceedings to the 14th International Conference on Space Operations (SpaceOps), Daejeon, South Korea, pp. 1-8, 2016.

21) T. Hashimoto, T. Yamada, J. Kikuchi, M. Otsuki, T. Ikenaga and OMOTENASHI Project Team, "Nano Moon Lander: OMOTENASHI", Proceedings to the 31st International Symposium on Space Technology and Science (ISTS), Matsuyama, Japan, pp. 1-5, 2017.

22) S. Song, H. Kim and Y.K. Chang, "Design and Implementation of 3U CubeSat Platform Architecture", International Journal of Aerospace Engineering, Vol. 2018, pp. 1-17, 2018.

23) F. Santoni and F. Piergentili, "Design and Test of a Maximum Power Point Tracking System for UNISAT-3 Microsatellite", Proceedings to the 55th International Astronautical Congress, Vol. 10, pp. 6668-6677, 2004.

24) S. Notani and S. Bhattacharya, "Flexible Electrical Power System Controller Design and Battery Integration for 1U to 12U CubeSats", Proceedings to the 2011 IEEE Energy Conversion Congress and Exposition, Phoenix, AZ, USA, pp. 3633-3640, 2011.

25) D. Selva and D. Krejci, "A Survey and Assessment of the Capabilities of CubeSats for Earth Observation", Acta Astronautica, Vol. 74, pp. 50-68, 2012.

26) F. Santoni, F. Piergentili, G. P. Candini, M. Perelli, A. Negri and M. Marino, "An Orientable Solar Panel System for Nanospacecraft", Acta Astronautica, Vol. 101, pp. 120-128, 2014.

27) P. Senatore, A. Klesh, T. H. Zurbuchen, D. McKauge and J. Cutler, "Concept, Design and Prototyping of XSAS: A High Power Extendable Solar Array for CubeSat Applications", Proceedings to the 40th Aerospace Mechanisms Symposium, NASA Kennedy Space Centre, Florida, USA, pp. 431-444, 2010.

28) F. Santoni, F. Piergentili, S. Donati, M, Perelli, A. Negri and M. Marino, "An Innovative Deployable Solar Panel System for CubeSats", Acta Astronautica, Vol. 95, pp. 210-217, 2014.

29) A. T. Klesh, J. Baker and J. Krajewski, "MarCO: Flight Review and Lessons Learned", Proceedings to the 33rd Annual AIAA/USU Conference on Small Satellites, Logan, Utah State, USA, pp.1-6 2019.

30) A. Ampatzoglou and V. Kostopoulos, "Design, Analysis, Optimization, Manufacturing, and Testing of a 2U CubeSat", International Journal of Aerospace Engineering, Vol. 2018, pp. 1-15, 2018.

31) Innovative Solutions In Space B.V., Custom Solar Panels-ISIS-Innovative Solutions in Space, https://www.isispace.nl/product/custom-solar-panels-cubesats-nanosats/, Online, last accessed: 08,17,2020.

32) T. Y. Park, B. G. Chae and H. U. Oh, "Development of 6U CubeSat's Deployable Solar Panel with Burn Wire Triggering Holding and Release Mechanism", International Journal of Aerospace Engineering, Vol. 2019, pp. 1-13, 2019.

33) L. S. Lim, T. D. V. Bui, K. S. Low et al., "VELOX-II: Challengers of Developing a 6U Nanosatellite", Proceedings to the AIAA SPACE Conference and Exposition, Long Beach, California, pp. 1-11, September 13-16, 2016.

34) S. Lee, A. Hutputanasin, A. Toorian, W. Lan and R. Munakata, "CubeSat Design Specification Rev. 12", California Polytechnic State University, San Luis Obispo, USA, pp. 1-22, 2009.

35) GOMspace, NanoPower DSP-GOMspace, Deployable Solar Panels for 3U and 6U Satellites, https://gomspace.com/shop/subsystems/power/nanopowerdsp.aspx, Online, last accessed: 08,17,2020.

36) Solar Arrays-MMA Deisign LLC, https://mmadesignllc.com/products/solar-arrays/, Online, last accessed: 08,17,2020.

37) Y. H. Li, X. G. Li, Y. Q. Wen, S. W. Guo, L. Cheng and H. N. Mu, "Optimal Design of An Explosive Separation Device based on LS-DYNA", Journal of Beijing Institute of Technology, Vol. 25, pp. 24-28, 2016.

38) A. T. Guzik and O. Benafan, "Design and Development of CubeSat Solar Array Deployment Mechanisms Using Shape Memory Alloys", Proceedings to the 44th Aerospace Mechanisms Symposium, Ohio, pp. 1-14, 2018.

39) A. Gaude and V. Lappas, "Design and Structural Analysis of a Control Moment Gyroscope (CMG) Actuator for CubeSats", Aerospace, Vol. 7. pp. 1-16, 2020.

40) Y. H. Li, J. C. Wang, L. Cheng et al., "Numerical Simulation of Separation Shock Characteristics of a Piston Type Explosive Bolt", Vibroengineering PROCEDIA, Vol. 21, pp. 214-219, 2018.

41) H. U. Oh and M. J. Lee, "Development of a Non-explosive Segmented Nut-type Holding and Release Mechanism for Cube Satellite Applications", Transactions of the Japan Society for Aeronautical and Space Science, Vol. 58, pp. 1-6, 2015.

42) J. Lee, D. H. Hwang and J. H. Han, "Numerical Study on Pyroshock Generation and Propagation from Pyrotechnic Release Devices using Hydrocodes", Proceedings to the 21st International Congress on Sound and Vibration, Florence, Italy, pp. 1-8, 2015.

43) X. Pan, Y. Zhang, Y. Lu, F. Yan and H. Yue, "A Reusable SMA Actuated Non-Explosive Lock-Release Mechanism for Space Application", International Journal of Smart and Nano Materials, Vol. 11, pp. 1-13, 2020.

44) National Aeronautics Space Administration (NASA), "Launch Services Program, Program Level Dispenser and CubeSat Requirements Document", LSP-REQ-317.01, Revision B, pp. 1-14, 2014. https://www.nasa.gov/pdf/62 7972main_LSP-REQ-317_01A.pdf, Online, last accessed: 08,17,2020.

45) A. Thurn, S. Huynh and S. Koss, "A Nichrome Burn Wire Release Mechanism for CubeSats", Proceedings to the 41st Aerospace Mechanisms Symposium, Jet Propulsion Laboratory, Pasadena, CA, USA, pp. 479-488, 2012.

46) J. Gardiner, "Suitability of Nickel Chromium Wire Cutters as Deployable Release Mechanisms on CubeSats in Low Earth Orbit", Physics Capstone Project. Paper 24, pp. 1-20, 2015, https://digitalcommons.usu.edu/cgi/viewcontent.cgi?article=1023&context=phys_capstoneproject, Online, last accessed: 08,17,2020.

47) B. K. Bharadwaj and Y. V. Gupta, "Design Analysis and Testing of Antenna Development Mechanism for CubeSat Applications", Proceedings to the 2nd International Space Conference, New Delhi, India, pp. 1-5, 2015.

48) Y. Rahmat-Samii and A. C. Densmore, "Technology Trends and Challenges of Antennas for Satellite Communication Systems", IEEE Transactions on Antennas and Propagation, Vol. 63, No. 4, pp. 1191-1204, 2015.

49) W. Blackwell, K. Clark, D. Cousins, D. Crompton, A. Cunningham, M. Diliberto, L. Fuhrman, R. Leslie, I. Osaretin and S. Michael, "New Capabilities for All-Weather Microwave Atmospheric Sensing Using CubeSats and Constellations", Proceedings to the 31th Annual AIAA/USU Conference on Small Satellites, Logan, Utah, USA, pp. 1-5, 2015.

50) AAC Clyde Space Small Satellite Spacecraft Providers, https://www.aac-clyde.space/, Online, last accessed: 08,17,2020.

51) N. Ahmad, "Passive Damping in Stiffened Structures Using Viscoelastic Polymers", Ph.D. Thesis, Virginia Polytechnic Institute and State University, pp. 1-145, 2016.

52) B. C. Nakra, "Vibration Control in Machines and Structures Using Viscoelastic Damping", Journal of Sound and Vibration, Vol. 211, pp. 449-465, 1998.

53) K. Minesugi and J. Onoda, "Passive Vibration Suppression using Thin Tape with Viscous Lamina", Proceedings to the AIAA 36th Structures Structural Dynamics and Materials Conference, New Orleans, LA, U.S.A, pp. 200-206, 1995.

54) A. Torisaka and H. Yamakawa, "Optimum Vibration Control Design of a Light Weight Structure in Wide Frequency Domain", Journal of Environment and Engineering, Vol. 6, pp. 328-339, 2011.

55) S. C. Kwon, M. S. Jo, D. H. Ko and H. U. Oh, "Viscoelastic Multilayered Blade-type Passive Vibration Isolation System for a Spaceborne Cryogenic Cooler", Cryogenics, Vol. 105, pp. 1-16, 2020.

56) D. S. Steinberg, "Vibration Analysis for Electronic Equipment", 3rd ed., John Wiley and Sons, Inc. New York, USA, pp. 1-414, 2000.

57) T. Y. Park, S. H. Kim, H. Kim and H. U. Oh, "Experimental Investigation on the Feasibility of Using Spring-Loaded Pogo Pin as a Holding and Release Mechanism for CubeSat's Deployable Solar Panels", International Journal of Aerospace Engineering, Vol. 2018, pp. 1-10, 2018.

58) S. Bhattarai, H. Kim, S. H. Jung and H. U. Oh, "Development of Pogo Pin based Holding and Release Mechanism for Deployable Solar Panel of CubeSat", International Journal of Aerospace Engineering, Vol. 2019, pp. 1-13, 2019.

59) S. J. Kang and H. U. Oh, "On-Orbit Thermal Design and Validation of 1 U Standardized CubeSat of STEP Cube Lab", International Journal of Aerospace Engineering, Vol. 2016, pp. 1-17, 2016.

60) Blue Canyon Technologies, XACT Attitude Control System, https://bluecanyontech.com/static/datasheet/BCT_DataSheet_Components_ACS.pdf, Online, last accessed: 08,17,2020.

61) Space Solar Cells-Azur Space Solar Power, Solar Cell 3G30C, http://www.azurspace.com/index.php/en/products/products-space/space-solar-cells, Online, last accessed: 08,17,2020.

62) N. H. Crisp, K. Smith and P. Hollingsworth, "Launch and Development of Distributed Small Satellite Systems", Acta Astronautica, Vol. 114, pp. 65-78, 2015.

63) D. Y. Lee, J. W. Culter, J. Mancewicz and A. J. Ridley, "Maximizing Photovoltaic Power Generation of a Space-dart Configured Satellite", Acta Astronautica, Vol. 111, pp. 283-299, 2015.

64) J. G. Llorente, A. A. Lidtke, K. Hatanaka, R. Kawauchi and K. I. Okauyama, "Solar Module Integrated Converters as Power Generator in Small Spacecrafts: Design and Verification Approach", Aerospace, Vol. 6, pp. 1-23, 2019.

65) S. S. Sanjuan, J. G. Llorente and R. H. Velasco, "Comparison of the Incident Solar Energy and Battery Storage in a 3U CubeSat Satellite for Different Orientation Scenarios", Journal of Aerospace Technology and Management, Vol. 8, pp. 91-102, 2016.

66) T. Etchells and L. Berthoud, "Developing a Power Modelling Tool for CubeSats, Proceedings to the Annual AIAA/USU Conference on Small Satellites", Logan, USA, pp. 1-9, 2019.

67) NanoPower BPX Datasheet-GOMSpace, NanoPower BPX, https://gomspace. com/UserFiles/Subsystems/datasheet/gs-ds-nanopower-bpx-318.pdf,lastaccess ed: 10,17,2020.

68) NanoPower Battery-GOMSpace, NanoPower Battery 2600 mAh, https://goms pace.com/UserFiles/Subsystems/datasheet/gs-ds-nanopower-bpx-3-18.pdf, Online, last accessed: 10,17,2020.

69) 3M Company, 3M^{TM} Adhesive Transfer Tape 966, https://3m.citrination.com/ pif/ 000314?locale=en-US, Online, last accessed: 10,17,2020.

70) J. R. Maly, B. B. Reed, M. J. Viens et al. "Life Cycle Testing of Viscoelastic Material for Hubble Space Telescope Solar Array 3 Damper", Proceedings to the Smart Structures and Materials, San Diego, California, United States, pp.128-140, 2003.

71) Texas Instruments, SN74LVCIG86 Single 2-Input Exclusive-OR Gate datasheet, https://www.ti.com/lit/ds/symlink/sn74lvc1g86.pdf, Online, last accessed:10,17,2020.

72) CFE Company, DIP Spring Pogo Electrical Contact Pins Connector, https://www.cfeconn.com/connector/dip-spring-pogo-electrical-contact-pins-connector, Online, last accessed: 10,17,2020.

73) PSA Company, Resistors-Walsin Technology, http://www.passivecomponent .com/products/resistors/, Online, last accessed: 08,17,2020.

74) Components101,PC817Photo-CouplerIC, https://components101.com/ics/pc8 17-ic-pinout-equivalent-datasheet, Online, last accessed: 08,17,2020.

75) YGK Nylon Wire, YGK Nylon Shock Leader Line, YGK-Jignpop.com, https:// jignpop.com/ygk-nylon-shock-leader-line/, Online, last accessed: 08,17,2020.

76) A. S. Santome, G. U. Sosa and B. R. Angeles et al., "Conceptual Design and Finite Element Method Validation of New Type of Self-locking Hinge for Deployable CubeSat Solar Panels", Advances in Mechanical Engineering, Vol. 11, pp. 1-13, 2019.

77) L. Puig, A. Barton and N. Rando, "A Review on Large Deployable Structures for Astrophysics Missions", Acta Astronautica, Vol. 67, pp. 12-26, 2010.

78) D. Zhang, L. Liu, J. Leng and Y. Liu, "Ultra-light Release Device Integrated with Screen-printed Heaters for CubeSat's Deployable Solar Arrays", Composite Structures, Vol. 232, pp. 1-11, 2020. (Article id. 111561).

79) R. Trabert, A. Klesh and P. Senatore, et al. "The eXtendable Solar Array System: A Modular Nanosatellite Power System", Proceedings to the AIAA/AAS Astrodynamics Specialist Conference, Toronto, Canada, pp. 1-15, 2010.

80) D. X. Li, W. Liu and C. Z. Fan, "Dynamic Characteristics of Satellite Solar Arrays under the Deployment Shock in Orbit", International Journal of Aerospace Engineering, Vol. 2018, pp. 1-8, 2018.

81) X. Ding, X. Li, K. Xu, Q. Yang and H. Pu, "Study on the Behavior of Solar Array Deployment with Root Hinge Drive Assembly", Chinese Journal of Aeronautics, Vol. 25, No. 2, pp. 276-284, 2012.

82) L. X. Zhang, Z. F. Bai, Y. Zhao and X. B. Cao, "Dynamic Response of Solar Panel Deployment on Spacecraft System Considering Joint Clearance", Acta Astronautica, Vol. 81, No. 1, pp. 174-185, 2012.

83) ECSS-E-ST-33-01C, "Space Engineering, Mechanisms", Requirements & Standards Division, Noordwijk, The Netherlands, pp. 1-65, 2009.

84) MiSuMi, Torsional Springs, https://us.misumi-ec.com/vona2/detail/10302306 960/ Online, last accessed: 08,17,2020.

85) I. Yunis, "The Standard Deviation of Launch vehicle Environments", Proceedings to the 46th AIAA/ASME/ASCE/AHS/ASC Structures, Structural Dynamics and Materials Conference, Austin, Texas, pp. 1-7, 2005.

86) GEVS: GSFC-STD-7000A, "General Environmental Verification Standard (GEVS) for GSFC Flight Programs and Projects," NASA Goddard Space Flight Center, pp. 1-203, 2013.

87) A. D. Scott, "An Analysis of Spacecraft Dynamic Testing at the Vehicle Level", Master Thesis, Naval Postgraduate School, Monterey, California, pp. 1-140, 1996.

88) F. Singarayar, R. Reinhard, C. Asma et al., "QB50 System Requirements and Recommendations", Issue 4, pp. 1-28, 2013, https://www.qb50.eu, Online, last accessed: 06,22,2020.

89) C. Knight, M. Remedia, G. S. Aglietti and G. Richardson, "Satellite Vibration Testing: Angle Optimisation Method to Reduce Overtesting", Acta Astronautica, Vol. 147, pp. 205-218, 2018.

90) M. A. Macchia, "Application of Metamaterials for Multifunctional Satellite Bus Enabled via Additive Manufacturing", Master Thesis, Department of Aeronautics and Astronautics, Graduate School of Engineering and Management, Air Force Institute of Technology Air University, USA, pp. 1-151, 2019.

91) Ariane 5 User's Manual, European Space Agency, Issue 5 Revision 2, pp. 1-271, 2011, https://www.arianespace.com/wpcontent/uploads/2015/09/Ariane5_users_manual_Issue5_July2011.pdf, Online, last accessed: 10,17,2020.

92) G. I. Barsoum, H. H. Ibrahim and M. A. Fawzy, "Static and Random Vibration Analyses of a University CubeSat Project", Journal of Physics Conference Series 1264, pp. 1-14, 2019.

93) R. A. S. Moreira, J. D. Rodrigues and A. J. M. Ferreira, "A Generalized Layerwise Finite Element for Multi-layer Damping Treatments", Computational Mechanics, Vol. 37, No. 5, pp. 426-444, 2006.

94) F. Abdoun, L. Azrar, E. M. Daya and M. P. Ferry, "Forced Harmonic Response of Viscoelastic Structures by an Asymptotic Numerical Method", Computers and Structures, Vol. 87, No. 1-2, pp. 91-100, 2009.

95) J. M. Yang, X. D. Zhong and Y. Y. Zhao, "Strain Energy and Damping Analysis of Composite Laminates with Two Interleaved Viscoelastic Layers", Engineering Mechanics, Vol. 27, No. 3, pp. 212-216, 2010.

96) M. J. Li, G. W. Liu and Y. W. Xu, "Parameter Effects of the Main Controlled Anisotropic Layer on Structural Damping of Alternately Laminated Damped Structures", Acta Material Composite Sinica, Vol. 23, pp. 180-184, 2006.

97) G. L. Ghiringhelli and M. Terraneo, "Analytically Driven Experimental Characterisation of Damping in Viscoelastic Materials", Aerospace Science and Technology, Vol. 40, pp. 75-85, 2015.

98) M. Amabili, "Nonlinear Damping in Nonlinear Vibrations of Rectangular Plates: Derivation from Viscoelasticity and Experimental Validation", Journal of the Mechanics and Physics of Solids, Vol. 118, pp. 275-292, 2018.

99) D. Anastasio, S. Marchesiello, G. Kerschen and J. P. Noel, "Experimental Identification of Distributed Nonlinearities in the Modal Domain", Journal of Sound and Vibration, Vol. 458, pp. 426-444, 2019.

100) H. Moradi, G. Vossoughi and M. R. Movahhedy, "Experimental Dynamic Modelling of Peripheral Milling with Process Damping, Structural and Cutting

Force Nonlinearities", Journal of Sound and Vibration, Vol. 332, pp. 4709-4731, 2013.

101)   P. Olejnik and J. Awrejcewicz, "Coupled Oscillators in Identification of Nonlinear Damping of a Real Parametric Pendulum" Mechanical Systems and Signal Processing, Vol. 98, pp. 91-107, 2018.

102)   A. Torisaka, and H. Yamakawa, "Simultaneous optimization of thickness and sticking position of multilayer damping materials for vibration control of small satellite," Proceedings to the 11th AIAA/ISSMO Multidisciplinary Analysis and Optimization Conference, Portsmouth, Virginia, pp. 1633-1646, 2006.

103)   H. Xu, W. Li and J. Du, "Modal Analysis of General Plate Structures", Journal of Vibration and Acoustics, Vol. 136, pp. 1-11, 2014.

104)   A. N. Nayak, L. Satpathy and P. K. Tripathy, "Free Vibration Characteristics of Stiffened Plates", International Journal of Advanced Structural Engineering, Vol. 10, pp. 153-167, 2018.

105)   M. Bilasse, L. Azrar and E. M. Daya, "Complex Modes based Numerical Analysis of Viscoelastic Sandwich Plates Vibrations", Computers & Structures, Vol. 89, pp. 539-555, 2011.

106)   F. Yilmaz, O. Haktanir and A. B. Uygur, "Quasi-Static Structural Test of Satellites", Proceedings to the 7th International Conference on Recent Advances in Space Technologies, Istanbul, Turkey, pp. 421-424, 2015.

107)   M. Safarabadi and S. Bazargan, "Prediction of Equivalent Static Loads Act on a Micro Satellite via Modal Analysis", Engineering Solid Mechanics, Vol. 3, pp. 75-84, 2015.

108)   J. W. Miles, "On Structural Fatigue under Random Loading", Journal of the Aeronautical Sciences, Vol. 21, No. 11, pp. 753-762, 1954.

109)   ECSS "Space Engineering, Structural Factors of Safety for Spaceflight Hardware," ECSS-E-ST-32-10C Rev.1, 2009, https://ecss.nl/standard/ecss-e-st-32-10c-rev-1-structural-factors-of-safety-for-spaceflight-hardware/, Online, last accessed: 06,22,2020

110) I. Vertat and A. Vobornik, "Efficient and Reliable Solar Panels for Small CubeSat Picosatellites", International Journal of Photoenergy, Vol. 2014, pp. 1-9, 2014.

111) K. H. Kyung and C. Y. Han, "Analytical and Numerical Approaches of a Solar Array Thermal Analysis in a Low-earth Orbit Satellite", Advances in Space Research, Vol. 46, pp. 1427-1439, 2010.

112) D. W. Hengeveld, M. M. Mathison, J. E. Braun, E. A. Groll and A. D. Williams, "Review of Modern Spacecraft Thermal Control Technologies", HVAC&R Research, Vol. 16, No. 2, pp. 189-220, 2010.

113) V. Baturkin, "Mirco-satellite Thermal Control-concepts and Components", Acta Astronatutica, Vol. 56, pp. 161-170, 2005.

114) M. W. Smith, A. Donner, M. Knapp, et al. "On-Orbit Results and Lessons Learned from the ASTERIA Space Telescope Mission", Proceedings to the 32th Annual AIAA/USU Conference on Small Satellites, Utah, USA, pp. 1-20, 2018.

115) M. D. Rao, "Recent Applications of Viscoelastic Damping for Noise Control in Automobiles and Commercial Airplanes", Journal of Sound and Vibration, Vol. 262 pp. 457-474, 2003.

116) X. Zhou, D. Yu, X. Shao, S. Zhang and S. Wang, "Research and Applications of Viscoelastic Vibration Damping Materials: A Review", Composite Structures, Vol. 136, pp. 460-480, 2016.

117) A. D. Nashif and J. P. Henderson, "Vibration Damping", John Wiley & Sons, pp. 1-480, 1985.

118) C. T. Sun and Y. P. Lu, "Vibration Damping of Structural Elements", Prentice Hall PTR Englewood Cliffs, pp. 1-372, 1995.

119) H. Hu, S. P. Belouettar, M. Ferry and E. M. Daya, "Review and Assessment of Various Theories for Modeling Sandwich Composites", Composite Structures, Vol. 84, No. 3, 2008, pp. 282-292.

120) E. M. Kerwin, "Damping of Flexural Waves by a Constrained Viscoelastic Layer", The Journal of the Acoustical Society of America, Vol. 31, No. 7, pp. 952-962, 1959.

121) D. J. Mead and S. Markus, "The Forced Vibration of a Three-layer, Damped Sandwich Beam with Arbitrary Boundary Conditions", Journal of Sound and Vibration, No. 2, Vol. 10, pp. 163-175, 1969.

122) C. D. Johnson and D. A. Kienholz, "Finite Element Prediction of Damping in Structures with Constrained Viscoelastic Layers", AIAA Journal, No. 9, Vol. 20, pp. 1284-1290, 1982.

123) S. Tian, Z. Xu, Q. Wu and C. Qin, "Dimensionless Analysis of Segmented Constrained Layer Damping Treatments with Modal Strain Energy Method", Shock and Vibration, Vol. 2016, pp. 1-16, 2016.

124) T. X. Liu, H. X. Hua and Z. Zhang, "Robust Control of Plate Vibration via Active Constrained Layer Damping", Thin-Walled Structures, Vol. 42, pp. 427-448, 2004.

125) J. J. Kim and B. N. Agrawal, "Rest-to-rest Slew Maneuver of Three-axis Rotational Flexible Spacecraft," IFAC Proceedings Volumes", Vol. 41, pp. 12054-12060, 2008.

126) S. Bhattarai, H. Kim and H. U. Oh, "CubeSat's Deployable Solar Panel with Viscoelastic Multilayered Stiffener for Launch Vibration Attenuation", International Journal of Aerospace Engineering, Vol. 41, pp. 1-10, pp. 2020.

127) D. Roylance "Engineering Viscoelasticity", Department of Materials Science and Engineering Massachusetts Institute of Technology, Cambridge MA 2139, pp. 1-37, 2001.

128) D. Kamesh, R. Pandiyan and A. Ghosal, "Modeling, Design and Analysis of Low Frequency Platform for Attenuating Micro-vibration in Spacecraft", Journal of Sounds and Vibration, Vol. 329, pp. 3431-3450, 2010.

129) K. Avery, J. Finchel, J. Mee, W. Kemp, R. Netzer, D. Elkins, B. Zufelt and D. Alexander, "Total Does Test Results for CubeSat Electronics", Proceedings to the 2011 IEEE Radiation Effects Data Workshop, Las Vegas, NV, USA, pp. 1-4, 2011.

130) R. Kinubury, F. Schmidt, W. Blackwell, I. Osarentin, R. Legge, K. Cahoy and D. Sklair, "TID Tolerance of Popular CubeSat Components", Proceedings to the 2013 IEEE Radiation Effects Data Workshop (REDW), San Francisco, CA, USA, pp. 1-4, 2013.

131) M. Malagoli and Y. Allewaert, "Improvement of the Wire Rating Standards based on TV Testing and Thermal Modeling", Proceedings to the 48th International Conference on Environmental Systems, Albuquerque, New Maxico, pp. 1-15, 2018.

【Research Achievement】

< Research Article>

1. **S. Bhattarai**, J. S. Go, H. Kim, and H. U. Oh, "Experimental Validation of a Highly Damped Deployable Solar Panel Module with a Pogo Pin-based Burn Wire Triggering Release Mechanism," International Journal of Aerospace Engineering, Vol. 2020, pp. 1-14, 2020.

2. **S. Bhattarai**, H. Kim, and H. U. Oh, "CubeSat's Deployable Solar Panel with Viscoelastic Multi-layered Stiffener for Launch Vibration Attenuation," International Journal of Aerospace Engineering, Vol. 2020, pp. 1-10, 2020.

3. **S. Bhattarai**, H. Kim, S. H. Jung, and H. U. Oh, "Development of Pogo Pin-Based Holding and Release Mechanism for Deployment Solar Panel of CubeSat," International Journal of Aerospace Engineering, Vol. 2019 pp.1-13, 2019.

< Conference Paper>

1. **S. Bhattarai** and H. U. Oh, "Development of Holding and Release Mechanism for CubeSat Applications", Proceedings of Asian Joint Symposium on Aerospace Engineering, HICO Gyeongju, Republic of Korea, pp. 1-5, Oct.31-Nov. 3, 2018.

2. **S. Bhattarai**, S. H. Kim, J. S. Go, and H. U. Oh, "Structural and Thermal Analysis of 3U CubeSat's Deployable Solar Panel Module", Aerospace Systems Engineering Spring Conference, Jeju , Republic of Korea, pp.1-2, April 24-27, 2019.

3. **S. Bhattarai**, J. S. Go, and H. U. Oh, "Experimental CanSat Platform for Verification of Burn Wire Triggering Type Holding and Release Mechanism", Proceedings of Joint Symposium 32nd International Symposium on Space Technology (ISTS) & 9th Nano-Satellite Symposium (NSAT), Fukui, Japan, June 15-21, 2019.

4. **S. Bhattarai**, J. S. Go, H. Kim, and H. U. Oh, "Development of a Highly Damped Deployable PCB Solar Panel Module with Pogo Pin-based Burn Wire Triggering Release Mechanism for STEP Cube Lab-II 6U CubeSat", 2020 Spring Conference of Aerospace System Engineering", Jeju Island, South Korea, June 29-31, 2020.